THE UNIVERSITY
of ADELAIDE

Faculty of Sciences, Engineering and Technology

School of Physical Sciences

Department of Physics

Broken flavour-symmetry induced state mixing in lattice QCD+QED

Zeno Rafael Kordov

Supervisors:
A. Prof. Ross Young
A. Prof. James Zanotti

May 2022

Abstract

Lattice QCD affords us the unique opportunity to study the quark structure of hadrons non-perturbatively, through the couplings of quark-field operators to hadron mass-eigenstates. In this thesis, we study cases of flavour wavefunction mixing which are induced by broken flavour-symmetry, with particular consideration for the effects of isospin-breaking and electromagnetism. Namely, we investigate mixing between the octet baryons Σ^0 and Λ, and the pseudoscalar mesons π^0, η and η', respectively. The latter scenario introduces the computational challenge of calculating disconnected quark-loop diagrams on the lattice, and we have investigated various techniques for improving the calculation. Additionally, we calculate the masses of the pseudoscalar mesons in lattice QCD+QED simulations, and investigate their behaviour with respect to the flavour-symmetry features observed through the state mixing. Finally, we detail and present lattice determinations of the weak decay constants of the pseudoscalar mesons, with the investigation being informed by the aforementioned state mixing. The results obtained from lattice simulations in each investigation are used to fit quark mass and charge extrapolations for the relevant quantities.

Declaration

I certify that this work contains no material which has been accepted for the award of any other degree or diploma in my name, in any university or other tertiary institution and, to the best of my knowledge and belief, contains no material previously published or written by another person, except where due reference has been made in the text. In addition, I certify that no part of this work will, in the future, be used in a submission in my name, for any other degree or diploma in any university or other tertiary institution without the prior approval of the University of Adelaide and where applicable, any partner institution responsible for the joint-award of this degree.

I give permission for the digital version of my thesis to be made available on the web, via the Universitys digital research repository, the Library Search and also through web search engines, unless permission has been granted by the University to restrict access for a period of time.

I acknowledge the support I have received for my research through the provision of an Australian Government Research Training Program Scholarship.

Zeno Rafael Kordov

Acknowledgements

I'd first like to extend my sincere thanks to my supervisors Ross and James, whose warm support has given me the confidence and freedom to explore my research problems with an element of my own creativity, for which I am very grateful. I have appreciated and benefited from Ross' willingness to entertain long impromptu discussions of technical particulars, his consistently exhaustive feedback on my work, and ability to ascertain my point given an often insufficient explanation. Similarly, James' tireless technical assistance with all things lattice, mindfulness and respect for the completion of my goals, and ability to translate Ross-language into Zeno-language, have all been crucial to the producing of this thesis.

I'd like to thank all of the HDR students who have made my candidature so much more entertaining and provided countless discussions about physics and otherwise. In particular, a special thank you to my friends Alec and Curtis, with whom I've enjoyed many laughs and beers, and who have endured an unfortunately large amount of my venting about the stresses of PhD candidature. Enormous thanks also go out to all enjoyers of, and partakers in, our great sport of officeball, which despite appearing to be a horrible source of procrastination, has been sufficient motivation for my coming into the office on many days, where I presumably also got some work done.

Above all else, I am extremely grateful for the ongoing support of my partner Esther, who has always encouraged me to pursue my ambitions and believed in my ability to do so. For patient consolation when nothing seemed to be working out, excitement at my successes, and otherwise being the best companion I could hope for, I am endlessly appreciative.

Contents

Chapter 1

Introduction

The study of hadron physics, the broad subject of this thesis, perhaps began with Rutherford's 1911 discovery of the atomic nucleus [1], and subsequent identification of the proton with the hydrogen nucleus. It soon became clear that an additional nuclear constituent was required for the description of atoms heavier than Hydrogen, and the neutron was eventually discovered by Chadwick in 1932 [2, 3]. With these basic elements of the atomic nucleus identified and no known mechanism for their binding, it was in 1934 that Yukawa proposed a short-ranged, but very strong, attractive force felt between nucleons and mediated by a particle of mass intermediate to the electron and proton: the meson [4]. Yukawa's meson was discovered in 1937 [5, 6] and designated the pion to differentiate it from the similarly massive and concurrently discovered muon. Besides the discovery of antiparticles and expected observations of the antiproton and antineutron, occuring eventually in 1955 [7] and 1957 [8] respectively, the simple picture of hadron physics as nucleons interacting via pions was retained up until the discovery of the kaon in 1947 [9].

Beginning with the kaon, a seemingly endless stream of new baryon and meson discoveries commenced, due in part to the operation of the first modern particle accelerator, the Brookhaven Cosmotron [10]. Baryon number conservation had already been posited to explain the stability of the proton [11], and further important steps were made in this period towards understanding hadron structure: isospin and strangeness quantum numbers, and the organisation of some hadrons into charge multiplets [12–15]. Whilst these ideas were celebrated for their ability to generalise the plethora of particle decays that had been observed, as well as those seemingly disallowed, the revolution in the classification of all hadrons came in 1961 with Gell-Mann's 'Eightfold Way' [16, 17]. The success of the Eightfold Way was not only the classification of all known hadrons according to their strangeness and charge, akin to the periodic table in chemistry, but also prediction of the omega-minus baryon which was soon confirmed in 1964 [18].

In 1964 Gell-Mann, and Zweig independently, were able to correctly deduce the mechanism underlying the Eightfold Way: hadrons were bound states of more fundamental particles, which Gell-Mann called *quarks* [19]. At its conception, this quark model of hadrons had two primary issues which slowed its adoption, despite its attractive simplicity. One issue was that bound states of two or more identical quarks should be disallowed by the Pauli exclusion principle, for which a solu-

tion was proposed independently by Greenberg [20] and Han-Nambu [21], whereby quarks possessed an additional SU(3) degree of freedom; SU(3)-colour in the modern nomenclature. The second issue was that of confinement, the central question being why no one had observed a light, abundant, fractionally-charged, spin-$\frac{1}{2}$ particle consistent with any of the proposed quarks. Whilst deep inelastic scattering experiments had already revealed 'parton' structure within nucleons [22,23], it wasn't until the discovery of the J/ψ meson in 1974 [24, 25], and subsequent predictive success of a theorised charm quark [26], that the quark model met general acceptance.

Around this same period, the quark model was finding solid mathematical footing as a Yang-Mills[1] theory of quarks gauged by SU(3)-colour (1972, [28]), quantum chromodynamics (QCD), and the 1973 discovery of asymptotic freedom for non-abelian Yang-Mills theories suggested an explanation for confinement at low energies [29, 30]. In 1974, the American physicist Kenneth G. Wilson proposed a discretised formulation of the Euclidean-space theory of quarks and abelian gauge fields [31], showing that confinement was achieved in the strong-coupling limit, and indicating that this *lattice* construction could also be used to probe the new theory of QCD non-perturbatively. Whilst the realisation of asymptotic freedom makes perturbative methods tenable to high energy processes, the lattice gauge theory of Wilson remains uniquely capable of probing QCD at low energies in the present. By 1978 Wilson had begun work on computer simulations of non-abelian pure-gauge theories on the lattice using Monte Carlo methods [32], which, with the addition of many subsequent developments, is the basic conception of the numerical calculations employed in this thesis. In Chapter 2 we detail the construction of lattice QCD underlying the numerical calculations presented throughout this work and for use in the chapters thereafter, a detailed discussion of the calculation of disconnected quark-loops on the lattice is presented in Chapter 4.

While the complete description of hadron structure is wrapped up in the complexities of QCD, the Eightfold Way still offers a valuable and, importantly, digestible starting point for the discussion. For our purposes in this thesis we can limit consideration to just the up, down and strange quarks appearing in Gell-Mann's original construction, denoted SU(3)-flavour, since we restrict our lattice QCD simulations to only these light quarks. In the Eightfold Way, representations[2] of flavour wavefunctions with degenerate spins are constructed from products of the underlying fundamental representations, which are identified with quarks. Within these constructed representations, further divisions of particles into SU(2) multiplets may be made, with the common choice being isospin, the subgroup of SU(3)-flavour containing the up and down quarks. An attractive feature of isospin is that due to near degeneracy of the up and down quark bare masses, hadrons within an isospin multiplet have very similar masses. The mass-splittings between isospin multiplets within a representation are then dominated by the significantly larger (than the up/down)

[1] The non-abelian gauge field theory which Yang and Mills originally proposed [27] was actually a theory of nucleon fields gauged by SU(2)-isospin.

[2] Representations such as the spin-1/2 baryon octet and pseudoscalar meson octet. See Appendix A for more details.

strange quark mass. The varying electric charges of the hadrons are understood to further separate the mass spectrum of an isospin multiplet with a similarly small magnitude to the effects of the up–down mass difference. Whilst isospin is hence a natural choice, in the construction of the Eightfold Way it is arbitrary in the exact same sense as choosing the z-component of angular momentum as a quantum number, instead of x or y, in elementary quantum mechanics. The other choices of SU(2) subgroups of SU(3) will be discussed in detail in Chapter 3. In addition to supplying mass-splittings to the spectrums of hadrons within a representation, broken SU(3)-flavour symmetry also permits the flavour-wavefunctions of some particular states to mix together in the forming of mass eigenstates. This effect can be understood as resulting from the breaking of orthogonality of the SU(3)-flavour wavefunctions of hadrons with otherwise identical quantum numbers, and depending on the severity of mixing can have significant effects on observable hadron properties. The investigation of these types of broken flavour-symmetry effects within the lattice QCD framework, and in particular the wavefunction mixing, is the central theme of this thesis.

In Chapter 3 we study the state mixing of the isovector and isoscalar members of the spin-1/2 baryon octet, the Σ^0 and Λ respectively, which is consequential to various problems in nuclear physics such as the Λ–neutron interaction [33]. Therein we define the mixing and detail our program for calculating its extent in lattice QCD (and QED) simulations. We also obtain expressions which exhibit the quark mass and charge dependence of the state mixing, and show with preliminary results that the non-degenerate charges of the up and down quarks enhances the mixing by a comparable amount to their non-degenerate masses. Moreover, our preliminary result shows agreement with the phenomenological Dalitz-Von-Hippel determination [34], which includes both QCD and QED effects, and the QCD-component of the mixing we determine agrees with existing QCD-only determinations from chiral perturbation theory [35] and lattice QCD [36].

In Chapter 5 we extend the procedure of Chapter 3 to investigate the state mixing of the pseudoscalar mesons π^0, η and η', as well as their masses and those of the remaining octet mesons. Whilst the π^0 and η are isovector and isoscalar members of an octet respectively, analogous to the Σ^0 and Λ, the presence of the SU(3)-flavour singlet η' complicates the situation considerably. Moreover, the presence of flavour-neutral quark combinations in these mesons necessitates the calculation of quark-loop diagrams, which are notoriously difficult to calculate in lattice QCD. Existing lattice studies of mixing in this sector have been performed with exact isospin symmetry, and without QED [37–39], meaning that admixture with the π^0 is neglected. We obtain quark charge and mass parametrisations for the meson masses and π^0–η–η' mixing, and our preliminary results for the η–η' mixing see agreement with the existing isospin-exact determinations. The method we have employed however, with improved precision through additional lattice simulations, should resolve isospin-breaking effects in the mixing.

Finally, using the results of Chapter 5, we investigate the weak decay constants of the pseudoscalar mesons in Chapter 6. These weak decay constants are important inputs to phenomenology as they can be used to parametrise numerous electroweak decays of the pseudoscalar mesons. Moreover, because of their relationship to spontaneous chiral symmetry breaking, decays of the π^0, η and η' may be an important probe of physics beyond the standard model [40]. We also introduce a necessary extension to the non-perturbative RI'-MOM lattice renormalisation scheme which facilitates proper treatment of the relevant operators in simulations with QED. Significantly, we obtain quark mass and charge parametrisations for the decay constants that also require knowledge of the underlying state mixing as studied in Chapter 5. In Chapter 7 we summarise the work of Chapters 3–6 and give our concluding remarks.

Chapter 2

Lattice gauge field theory

The concept of simulating gauge field theories on a discrete lattice was first actualised by Wilson [31], as a means to investigate quark confinement in regimes where perturbative methods had proved untenable. In resemblance to perturbation theory, where a finite number of terms approximate the true result, the general outlook of studying gauge field theories on a lattice is to reduce the number of degrees-of-freedom of the theory sufficiently, while necessarily introducing some quantifiable error, such that calculations may be performed by a computer.

In simple terms, the lattice is a finite-extent volume with each dimension discretised so that it consists of a finite number of sites, each separated by a characteristic lattice spacing. That is, denoting neighbouring sites in some dimension as x_n and x_{n+1}, the lattice spacing is

$$a = x_{n+1} - x_n. \tag{2.1}$$

It is typical that the spacing a be common to each lattice dimension and this is true for the lattices used herein, which all possess the physical $3 + 1$ (space+time) dimensions. Having established this system which possesses a computationally manageable (finite) number of degrees of freedom, the aim of lattice gauge field theory is to then simulate the fundamental gauge and matter fields on this lattice, through various prescriptions which must be consistent with the (physical) continuum theory. It should be noted that the finite lattice spacing acts as a regulator to the theory, cutting off UV physics at a^{-1}, and hence the results of calculations performed on the lattice should be returned to the continuum via an extrapolation of $a \to 0$, and hence made independent of the regulator.

As suggested by the purpose for which it was formulated, the lattice is primarily used as a non-perturbative way of studying quantum chromodynamics (QCD) from first principles, and in this context referred to as 'lattice QCD'. Because the strong coupling is large at low energies, and therefore disallows perturbative study of QCD in this regime, lattice QCD has become an indispensable tool for probing strongly interacting particles at low energies. Whilst being uniquely capable of non-perturbative QCD calculations, in addition to requiring removal of the regulator dependence ($a \to 0$), it is also usually necessary to correct for the un-physical finite volume of the lattice. Moreover, an essential piece of lattice QCD machinery, the lattice quark propagator, becomes increasingly computationally expensive to calcu-

late as quark masses are reduced, meaning that lattice results are often obtained for un-physically large quark masses and subsequently extrapolated to their physical values. We note that in recent times however, an increasing number of lattice simulations with physical values of the quark masses are becoming available [41–44]. Controlling these various sources of systematic error is important in obtaining realistic results.

The aim of this chapter is to introduce the general methodology of lattice QCD, as well as specific details on the lattice techniques employed throughout this thesis. It is assumed that the reader is already familiar with gauge field theories in the continuum.

2.1 Technical formulation

The general formulation of lattice QCD makes use of the path integral construction of quantum field theory first developed by Feynman in his doctoral thesis [45]. In this construction, the correlation functions containing the physical information can be written as functional integrals over the fundamental fields of the theory, for example the scalar two-point correlation function[1]

$$\begin{aligned} C_S(y,x) &\equiv \langle\Omega|T(\bar{\psi}_f(y)\psi_{f'}(y)\,\bar{\psi}_{f'}(x)\psi_f(x))|\Omega\rangle \\ &= \frac{\int DA_\mu\, D\bar{\psi}\, D\psi\, \left(\bar{\psi}_f(y)\psi_{f'}(y)\,\bar{\psi}_{f'}(x)\psi_f(x)\right)\, e^{iS_{\mathrm{QCD}}}}{\int DA_\mu\, D\bar{\psi}\, D\psi\, e^{iS_{\mathrm{QCD}}}}. \end{aligned} \tag{2.2}$$

The A_μ and ψ_f are gauge and quark fields of flavour f respectively, and S_{QCD} is the standard QCD action

$$S_{\mathrm{QCD}} = S_{\mathrm{F}} + S_{\mathrm{G}} = \int d^4x \sum_f \bar{\psi}_f(i\gamma^\mu D_\mu - m_f)\psi_f - \frac{1}{4}G^a_{\mu\nu}G^{\mu\nu}_a, \tag{2.3}$$

where we have written the total action as the sum of the fermionic (S_{F}) and pure-gauge (S_{G}) components, noting however that the fermion action depends also on the gauge fields through the covariant derivative, $D_\mu = \partial_\mu - igt_aA^a_\mu$. The index a enumerates the eight generators of the fundamental representation of SU(3), $t_a = \lambda_a/2$, where λ_a are the Gell-Mann matrices, and g dictates the coupling strength of the quarks with the gluons. The integration measure of Equation (2.2) denotes integration of each field over every possible value at each spacetime point:

$$DA_\mu\, D\bar{\psi}\, D\psi = \prod_{a,x} dA^a_\mu(x) \prod_{f,x} d\bar{\psi}_f(x) \prod_{f,x} d\psi_f(x). \tag{2.4}$$

The Equation (2.2) is not readily adaptable to computational evaluation due to the complex argument of the exponential, but we can bypass this potential issue

[1] The term 'n-point function' is commonly used in lattice literature, with n simply indicating the number of space-time points present in the position-space correlation function.

by instead expressing the path integral in Euclidean space, consistent with the replacement $t \to -i\tau$. The Euclidean space representation of the two-point function Equation (2.2) is then given by

$$C_S(y,x) = \frac{\int DA_\mu \, D\bar{\psi} \, D\psi \, \left(\bar{\psi}_f(y)\psi_{f'}(y)\, \bar{\psi}_{f'}(x)\psi_f(x)\right) \, e^{-S^E_{\rm QCD}}}{\int DA_\mu \, D\bar{\psi} \, D\psi \, e^{-S^E_{\rm QCD}}}, \tag{2.5}$$

where the fields are now functions of Euclidean space vectors, i.e. obtained from the replacement $\psi(t,\vec{x}) \to \psi(\vec{x},\tau)$. The Euclidean QCD action is given by

$$S^E_{\rm QCD} = S^E_{\rm F} + S^E_{\rm G} = \int d^4x \sum_f \bar{\psi}_f \left(\gamma^E_\mu(\partial_\mu + igt_a A^a_\mu) + m_f\right)\psi_f + \frac{1}{4}G^a_{\mu\nu}G^{\mu\nu}_a, \tag{2.6}$$

where $\gamma^E_4 = \gamma^0$ and $\gamma^E_i = -i\gamma^i$.

Since fermion fields satisfy anti-commutation relations, it is instructive to view them as elements of a Grassmann algebra and employ the results of Berezin integration; the integration of Grassmann variables. There are many apt treatments of this subject in the literature, in the context of lattice [46] and otherwise [47], and so for our purposes we will simply employ some important results.

Since the gluonic part of the QCD action doesn't depend on the quark fields, we may write Equation (2.5) as

$$C_S(y,x) = \frac{\int DA_\mu \, e^{-S^E_{\rm G}} \, D\bar{\psi} \, D\psi \, \left(\bar{\psi}_f(y)\psi_{f'}(y)\, \bar{\psi}_{f'}(x)\psi_f(x)\right) \, e^{-S^E_{\rm F}}}{\int DA_\mu \, e^{-S^E_{\rm G}} \, D\bar{\psi} \, D\psi \, e^{-S^E_{\rm F}}}, \tag{2.7}$$

and we can write the fermion action in the suggestive form

$$S^E_{\rm F} = \sum_f \int d^4x \, d^4y \, \bar{\psi}_f(x) M_f(x,y) \psi_f(y), \tag{2.8}$$

with

$$M_f(x,y) \equiv \left[\gamma^E_\mu \left(\, \partial_\mu + igt_a A^a_\mu \,\right) + m_f\right] \delta^4(x-y), \tag{2.9}$$

and perform the functional integrals in the quark fields using Berezin integration to give

$$C_S(y,x) = \frac{-\int DA_\mu \, e^{-S^E_{\rm G}} \, {\rm Tr}\left[M^{-1}_f(x,y) M^{-1}_{f'}(y,x)\right] \prod_{f''} \det(M_{f''})}{\int DA_\mu \, e^{-S^E_{\rm G}} \, \prod_{f''} \det(M_{f''})}. \tag{2.10}$$

The trace Tr[...] in the above expression is performed over the spin and colour indices which have thus far been left implicit. The inverse of the fermion matrix, $M^{-1}_f(x,y)$, is also known as the fermion propagator (of flavour f), which we denote throughout this text as

$$S_f(x;y) \equiv M^{-1}_f(x,y). \tag{2.11}$$

The unique combination of quark propagators appearing in the numerator integrand of Equation (2.10) is determined by performing all allowed Wick contractions of the quark fields which leave no field uncontracted, and the spin and colour traces emerge from this process also provided the calculation is performed with all indices explicit.

Instead of attempting to naively sum the integrand for every configuration of gauge field available on the discrete lattice, the strategy of lattice QCD is to instead generate a finite number of gauge field configurations such that the probability of obtaining any particular configuration is $\propto \prod_f \det(M_f)\, e^{-S_{\mathrm{G}}^E}$ [48]. The generation of gauge field configurations according to this distribution is typically performed using a Monte Carlo algorithm such as Hybrid Monte Carlo [49]. Having generated such an ensemble of N_{cf} gauge field configurations, the path integral Equation (2.10) which may be interpreted as an average of the integrand over uniformly distributed paths, is approximated as the ensemble average

$$\langle\Omega|T(\bar{\psi}_f(y)\psi_{f'}(y)\,\bar{\psi}_{f'}(x)\psi_f(x))|\Omega\rangle \approx \frac{-1}{N_{cf}}\sum_{n=1}^{N_{cf}} \mathrm{Tr}\left[S_f(x;y)S_{f'}(y;x)\right]_n , \tag{2.12}$$

over paths distributed as previously described. For much of the work following this chapter we will leave the gauge ensemble average implicit in describing our correlation functions. Moreover, for the lattice simulations in this thesis we use three flavours of quarks which we identify with the up, down and strange quarks.

We remark that a historically common[2] practice in lattice calculations, known as the *quenched* approximation, is to set $\det(M_f) \equiv 1$ in the Monte Carlo generation of the gauge fields in order to reduce computational cost. This is intuitively understood as removing quarks from the QCD 'sea', which should have less effect on calculations for larger values of the quark masses, but introduces unknown systematic errors which make the approximation untenable to precision calculations.

The above path integral construction and subsequent arguments are readily generalised to more complicated n-point correlation functions containing both quark and gauge fields through Wick contraction. The discussion so far has proceeded in the language of the continuum, as opposed to a discrete spacetime, and so it remains to be shown how this process may be discretised. In the following few sections we will introduce the discretisation of the fermion and gluon actions present in our path integral expressions, as well as the addition of quantum electrodynamics (QED), with the result being lattice QCD+QED.

2.1.1 The discrete gauge action

An important consideration in the discretisation of gauge field theories is that the derivatives appearing in the action will necessarily be replaced by some form of finite-difference approximation. This means that derivatives of fermion fields which

[2]This approximation has become much less commonplace as computer performance increases and the emphasis of lattice calculations shifts towards high precision.

are local in the continuum theory will become non-local functions of multiple lattice sites, each with their own local values of the gauge fields. This motivates us to first introduce the lattice analogue of the Schwinger line integral, the Wilson line

$$U(x,y) = e^{ig\int_x^y dz_\mu\, t_a A_\mu^a(z)} = e^{ig\int_x^y dz_\mu\, \underline{A}_\mu(z)}, \tag{2.13}$$

with implicit sums over repeated indices as usual, and we have let $\underline{A}_\mu(z) \equiv t_a A_\mu^a(z)$. The Wilson line accounts for variation in the QCD gauge potential between the points x and y, so that they might be compared sensibly, and belongs to the fundamental representation of SU(3). Moreover, it may be used to render non-local products of fields gauge-invariant.

The discrete analogue of the Schwinger line integral for neighbouring lattice sites separated by the spacing a in the x-direction, for example, is given by $U(x, x+\hat{x}a) = e^{iga\underline{A}_1(x)}$. This leads us to define a ubiquitous lattice quantity: the lattice link variable,

$$U_\mu(x) \equiv e^{iga\underline{A}_\mu(x)} = 1 + iga\underline{A}_\mu(x) + \mathcal{O}(a^2). \tag{2.14}$$

The link variable has direction, with the link $U_\mu(x)$ extending from the site x to the site $x + \hat{\mu}a$, and it follows that $U_\mu^\dagger(x)$ extends from the site $x + \hat{\mu}a$ back to the site x.

The link variables transform according to

$$U_\mu(x) \to e^{i\Lambda(x)} U_\mu(x) e^{-i\Lambda(x+\hat{\mu}a)}, \quad U_\mu^\dagger(x) \to e^{i\Lambda(x+\hat{\mu}a)} U_\mu^\dagger(x) e^{-i\Lambda(x)}, \tag{2.15}$$

for $\Lambda(x)$ an arbitrary element of the SU(3) Lie algebra in the fundamental representation. The gauge transformation rules suggest that we may obtain gauge-invariant combinations of links by taking (colour) traces of products that correspond to closed paths. The simplest 1×1 path, which we denote the *plaquette*, in the μ-ν plane is given as

$$P_{\mu\nu}(x) = U_\mu(x) U_\nu(x + \hat{\mu}a) U_\mu^\dagger(x + \hat{\nu}a) U_\nu^\dagger(x), \tag{2.16}$$

which may be evaluated using (2.14) to yield $P_{\mu\nu}(x) = e^{iga^2\underline{G}_{\mu\nu}(x)}$, with $\underline{G}_{\mu\nu}$ evaluating to the gluon field strength tensor in the continuum limit $a \to 0$. Note that the plaquette itself is not gauge invariant but its trace, $\mathrm{Tr}[P_{\mu\nu}(x)]$, is.

It is straightforward to now use the plaquette to devise a combination of link variables which recovers the continuum QCD gluon action, S_G in Equation (2.3), as $a \to 0$, and the most simple such combination is given by

$$S_\mathrm{G}[U] = \beta_\mathrm{QCD}\, a^4 \sum_x \sum_{\mu<\nu} \left[1 - \frac{1}{6} \mathrm{Tr}\left(P_{\mu\nu}(x) + P_{\mu\nu}^\dagger(x) \right) \right], \tag{2.17}$$

where the indicated trace is performed in the colour degrees of freedom, and $\beta_\mathrm{QCD} \equiv 6/g^2$. The sums in Equation (2.17) are such that they enumerate every distinct plaquette on the lattice, and the adjoint plaquette appearing within the trace ensures that the resulting action is real. Note also the factor a^4 which originates with the

discretisation of the integral:

$$\int d^4x \longrightarrow \sum_x a^4. \tag{2.18}$$

For reference we have listed the discretised forms of a variety of continuum expressions used herein in Appendix B.

The QED action

The construction of a discretised Euclidean action for QED is quite straightforward from a theoretical perspective and proceeds analogously to QCD. The continuum Euclidean QCD action in Equation (2.6) may be updated to include QED as

$$S^E_{\text{QCD+QED}} = \int d^4x \sum_f \bar{\psi}_f \left(\gamma^E_\mu(\partial_\mu + ig\underline{A}_\mu + iq_f A^{EM}_\mu) + m_f\right)\psi_f$$

$$+ \frac{1}{4} G^a_{\mu\nu} G^{\mu\nu}_a + \frac{1}{4} F_{\mu\nu}F^{\mu\nu}, \tag{2.19}$$

where A^{EM}_μ and $F_{\mu\nu}$ denote the U(1) gauge potential and QED field strength tensor respectively, and q_f the electric charge of the quark flavour f. The arguments that lead us to Equations (2.10) and (2.12) may be repeated with S^E_{G} updated to include the last term of Equation (2.19), and the covariant derivative $D \to \partial_\mu + ig\underline{A}_\mu + iq_f A^{EM}_\mu$.

In order to construct the lattice QED action used in this work, which is known as the *noncompact* action, we define a discretised form of the EM field strength tensor, made simple by the abelian nature of the gauge group

$$F_{\mu\nu}(x) = \frac{1}{a}\left[A^{EM}_\nu(x + a\hat{\mu}) - A^{EM}_\nu(x) - A^{EM}_\mu(x + a\hat{\nu}) + A^{EM}_\mu(x)\right]. \tag{2.20}$$

Using the above construction the discretised action may be immediately written as

$$S_{\text{QED}}[A^{EM}] = \frac{a^2}{2e^2}\sum_x \sum_{\mu<\nu} \left[A^{EM}_\nu(x + a\hat{\mu}) - A^{EM}_\nu(x) - A^{EM}_\mu(x + a\hat{\nu}) + A^{EM}_\mu(x)\right]^2, \tag{2.21}$$

where e is the elementary charge.

We have now arrived at a simple construction of the pure-gauge component of the lattice QCD+QED action,

$$S_{\text{G}}[U, A^{EM}] = \beta_{\text{QCD}}\, a^4 \sum_x \sum_{\mu<\nu} \left[1 - \frac{1}{6}\text{Tr}\left(P_{\mu\nu}(x) + P^\dagger_{\mu\nu}(x)\right)\right] +$$

$$\frac{a^2}{2e^2}\sum_x \sum_{\mu<\nu} \left[A^{EM}_\nu(x + a\hat{\mu}) - A^{EM}_\nu(x) - A^{EM}_\mu(x + a\hat{\nu}) + A^{EM}_\mu(x)\right]^2. \tag{2.22}$$

Note that $1/e^2$ may be denoted by $\beta_{\mathrm{QED}} \equiv 1/e^2$. This simple gauge action has corrections beginning at $\mathcal{O}(a^2)$, and there are a variety of techniques commonly employed to improve on this. In particular, the results in this thesis have been obtained using a tree-level Symanzik improved gluon action [50], which makes use of some more extended and complex link variable constructions. The QED gauge action used herein remains unimproved however.

2.1.2 Fermions in lattice QCD+QED

We will begin by constructing a simple, intuitive discretisation of the continuum fermion action before discussing some necessary improvements. In the absence of gauge fields, the Euclidean fermion action is given by

$$S_{\mathrm{F}}^{free} = \int d^4x \sum_f \bar{\psi}_f \left(\gamma_\mu \partial_\mu + m_f\right) \psi_f, \tag{2.23}$$

and we may approximate the derivative on the lattice as a symmetric finite difference

$$\partial_\mu \psi(x) \to \frac{1}{2a} \left(\psi(x + \hat{\mu}a) - \psi(x - \hat{\mu}a)\right). \tag{2.24}$$

We may deduce then that a reasonable lattice action for fermions is given as

$$S_{\mathrm{F}}^{free} \to \sum_f \sum_x \sum_\mu \frac{a^3}{2} \left[\bar{\psi}_f(x)\gamma_\mu \psi_f(x + \hat{\mu}a) - \bar{\psi}_f(x)\gamma_\mu \psi_f(x - \hat{\mu}a)\right] + a^4 \sum_f \sum_x m_f \, \bar{\psi}_f(x)\psi_f(x), \tag{2.25}$$

and we refer to this as the naive lattice action. Note that the dimensions of the quark mass and quark fields in terms of the lattice spacing are a^{-1} and $a^{-3/2}$ respectively. Unfortunately, this naive action has a well-studied flaw known as 'the doubling problem' [46] which makes it unsuitable for realistic calculations. The so-called doubling problem is that in the continuum, the quark propagator associated with the naive fermion action receives contributions from 16 momentum-space excitations where only *one* should be present.

There are various alternative approaches to discretising the fermion action which avoid the doubling problem and give the correct continuum limit. Unfortunately, in solving the doubling problem there are other well-known issues that necessarily arise [51], such as the explicit breaking of chiral symmetry (even as $m_f \to 0$) in Wilson's formulation [52], or the restrictions on quark flavours present in the 'staggered' formulation [53–55]. It follows then that the action one chooses in performing a lattice calculation must depend on the application.

For our purposes herein we utilise an $\mathcal{O}(a)$-improved formulation of the Wilson action known as the Sheikholeslami-Wohlert or, more commonly, *clover* action [56]. Firstly, the Wilson action is obtained from the naive action by the addition of a

finite-difference second-derivative term with vanishing effect in the continuum,

$$S_{\mathrm{F}}^{(W)} = S_{\mathrm{F}}^{naive} - \frac{ra^3}{2}\sum_f\sum_x\sum_\mu \bar{\psi}_f(x)\left[\psi_f(x+\hat{\mu}a) + \psi_f(x-\hat{\mu}a) - 2\psi_f(x)\right], \quad (2.26)$$

where r is the Wilson parameter. As previously mentioned, the addition of this term results in broken chiral symmetry even for $m_f \to 0$, but removes fermion doublers. Generalising the fermion action to the interacting theory with QCD and QED, we can insert the relevant link variables which render the Wilson action gauge invariant as

$$S_{\mathrm{F}}^{(W)}[U, A^{EM}, \bar{\psi}, \psi] = \sum_f\sum_x\sum_\mu \frac{a^3}{2}\big[\bar{\psi}_f(x)(\gamma_\mu - r)e^{iaq_f A_\mu^{EM}(x)}U_\mu(x)\psi_f(x+\hat{\mu}a) -$$

$$\bar{\psi}_f(x)(\gamma_\mu + r)e^{-iaq_f A_\mu^{EM}(x)}U_\mu^\dagger(x-\hat{\mu}a)\psi_f(x-\hat{\mu}a)\big] + \sum_f (m_f a + 4r)\, a^3 \sum_x \bar{\psi}_f(x)\psi_f(x), \quad (2.27)$$

where $e^{iaq_f A_\mu^{EM}(x)}$ is the QED link variable responsible for including the coupling of the photon field to the quark flavour f with electric charge q_f, analogous to Equation (2.14).

Besides breaking chiral symmetry, a further consequence of the Wilson action is that the additional term introduces $\mathcal{O}(a)$ errors, where the gauge actions are good to (at least) $\mathcal{O}(a^2)$ [50]. This motivates the Sheikholeslami-Wohlert $\mathcal{O}(a)$-improvement of the Wilson action, which is achieved by the addition of a further term,

$$S_{\mathrm{F}}^{(SW)} = S_{\mathrm{F}}^{(W)} - \frac{c_{SW}\, a^4}{4}\sum_f\sum_x\sum_{\mu,\nu} \bar{\psi}_f(x)\sigma_{\mu\nu}\hat{G}_{\mu\nu}(x)\psi_f(x), \quad (2.28)$$

where c_{SW} is the clover coefficient which may be tuned to optimise the improvement perturbatively or, as in our case, non-perturbatively [50], and $\hat{G}$ is a discretised gluon field strength tensor given explicitly in terms of QCD link variables [56].

The quark hopping parameter

In practice, it is typical to define the 'hopping parameter' $\kappa_f \equiv 1/(2m_f a + 8r)$ and re-scale the quark fields according to $\psi_f/\sqrt{2}\kappa_f \to \psi_f$, which yields

$$S_{\mathrm{F}}^{(SW)}[U, A^{EM}, \bar{\psi}, \psi] = \sum_f\sum_{x,y} \bar{\psi}_f(x)M_f(x,y)\psi_f(y), \quad (2.29)$$

where the clover fermion matrix is given by

$$M_f(x,y) = \delta_{x,y}a^3 - a^3\kappa\sum_\mu \big[(r-\gamma_\mu)e^{iaq_f A_\mu^{EM}(x)}U_\mu(x)\delta_{x+\hat{\mu}a,y} +$$

$$(\gamma_\mu + r)e^{-iaq_f A_\mu^{EM}(x)}U_\mu^\dagger(x-\hat{\mu}a)\delta_{x-\hat{\mu}a,y}\big] - \frac{\kappa_f\, c_{SW}\, a^4}{2}\sum_{\mu,\nu}\sigma_{\mu\nu}\hat{G}_{\mu\nu}(x)\delta_{x,y}. \qquad (2.30)$$

In our simulations we take the Wilson parameter $r = 1$, and in the absence of gauge fields the Wilson quark's bare mass is then given in terms of the hopping parameter by $am_f = 1/2\kappa_f - 4$. With interactions present, broken chiral symmetry manifests as an additive renormalisation of the quark mass which depends on the lattice spacing, giving

$$am_f = \frac{1}{2\kappa_f} - \frac{1}{2\kappa_f^c}, \qquad (2.31)$$

where κ_f^c is the *critical* hopping parameter, which must be determined for a given set of c_{SW}, β_{QCD} and β_{QED} values. The value of κ_f^c may be inferred from the κ-dependence of the pion mass on the lattice, since the pion mass is known to vanish when the relevant bare quark mass vanishes, independent of the lattice spacing. We discuss this process for the lattice ensembles used in this thesis in Section 2.3.

Scale setting

One might assume that the spacing a is an input parameter to a lattice calculation, but in fact it is not independent of β_{QCD}, and hence the actions are constructed in a dimensionless way and the spacing is determined after-the-fact. A common choice is to determine the scale by calculating a quantity such as a hadron mass M, accessible only in the dimensionless combination aM on the lattice, and comparing the result with an experimental value,

$$a = \frac{(aM)^{latt.}}{M^{exp.}}. \qquad (2.32)$$

One technicality with this approach is the dependency of the lattice quantity aM on the input bare quark masses. To properly compare with the experimental value, aM should be calculated using 'physical' values of the bare quark masses, or the lattice value extrapolated to the physical point using multiple determinations at large quark-mass values. Moreover, the 'physical' bare quark masses should be determined from where ratios of lattice hadron masses take their experimental values. The lattice spacings of the ensembles employed in this thesis have been determined in this manner from hadron masses, and we will discuss this in greater detail in Section 2.3.

There are various alternatives which avoid the calculation of lattice quark propagators such as the Sommer scale, r_0 [57], and w_0 scale [58–60]. These methods are used to set the overall scale so that the QCD renormalisation group may be used to determine a directly from β_{QCD}.

The lattice quark propagator

Recall now our method for approximating the two-point function in Equation (2.12), and note that the above fermion matrix, Equation (2.30), is a discrete analogue of the continuum Dirac matrix referenced there. We may summarise that, generally

speaking, approximation of hadronic correlation functions on the lattice is achieved by averaging the appropriate combination of quark propagators over an ensemble of link variable configurations. These configurations are generated according to a distribution governed by a discrete gauge action, such as that given by Equation (2.22), and further weighted by the determinants of discrete fermion matrices such as those given by Equation (2.30). We will now discuss the calculation of the inverse (discrete) fermion matrix, or quark propagator, in some more detail.

The complete, 'all-to-all' lattice quark propagator $S(y;x)$, connecting each site x with all sites y, is a prohibitively costly object to compute and store for typical lattice sizes. We have dedicated Chapter 4 to the approximation of this object for use in Chapters 5 and 6, but for many applications it is sufficient to compute correlation functions using propagators connecting a single source point x_0 to every lattice site y, denoted 'point-to-all' propagators, $S_f(y;x_0)$. This is possible due to the translational invariance of the resulting correlation functions; any site in the lattices four-volume is a suitable source point upon gauge ensemble average. The point-to-all propagator is calculated by numerically inverting the fermion matrix against a delta function as in the equation

$$\sum_y M(x,y)^{ca}_{\zeta\alpha}\, S(y;x_0)^{ab}_{\alpha\beta} = \delta_{x\,x_0}\,\delta^{b\,c}\,\delta_{\beta\,\zeta}, \tag{2.33}$$

where we have made the colour (superscript) and spin (subscript) indices explicit. An inversion must be performed for each of the 12 combinations of spin and colour at the source. When performing Wick contractions for fermionic two-point functions with a fixed source location, it is typical to encounter quark propagators like $S(x_0;y)$, connecting every site at the source to a single sink. A very useful transformation property of the propagator in this instance is $S(x_0;y) = \gamma_5 S(y;x_0)^\dagger \gamma_5$, which allows us to write such correlation functions entirely in terms of the point-to-all propagator.

Note that the lattice quark propagator itself is not gauge-invariant, and there are many additional Green's functions of interest that require gauge-fixing to allow for comparison with other determinations. We will be predominantly interested in gauge-invariant combinations of quark propagators in this work, such as our base example in Equation (2.2), and hence for our current purposes we only note that various programs for lattice gauge-fixing exist (e.g. [61]).

2.2 Correlation functions

We have spent the preceding section introducing the basic means for approximating the continuum Green's functions of QCD and QED on a discrete lattice. In particular, this approximation proceeds via evaluation of lattice-regularised path integrals such as the right-hand side of Equation (2.5). In this section we will take a closer look at the Green's functions themselves, and in particular introduce the spectral decomposition and large Euclidean-time limit, which are frequently invoked in extracting lattice quantities.

Let us generalise Equation (2.5) to a two-point function with arbitrary *source* and *sink* operators $\mathcal{O}_i$ and $\mathcal{O}_j$ respectively,

$$\langle\Omega|\mathcal{O}_j(y)\,\mathcal{O}_i(x)|\Omega\rangle = \frac{\int DA_\mu\, D\bar{\psi}\, D\psi\, \mathcal{O}_j(y)\,\mathcal{O}_i(x)\, e^{-S}}{\int DA_\mu\, D\bar{\psi}\, D\psi\, e^{-S}}, \tag{2.34}$$

where the time-ordering $\tau' = y_4 > x_4 = \tau$ is assumed, and the correlation function of Equation (2.2) is recovered if we choose $\mathcal{O}_j(y) = \bar{\psi}_f(y)\psi_{f'}(y)$ and $\mathcal{O}_i(x) = \bar{\psi}_{f'}(x)\psi_f(x)$.

We have discussed in the previous section how to deal with the right-hand side of Equation (2.34) under lattice regularisation, and we will now investigate the left-hand side under the same discretisation. It is usually more instructive to study the left-hand side after integrating the spatial degrees of freedom, and so we perform the discrete Fourier transforms

$$C\left(\vec{p}\,',\tau';\vec{p},\tau\right) \equiv \frac{1}{L^3}\sum_{\vec{x},\vec{y}} e^{i\vec{p}\,'\cdot\vec{y}} e^{-i\vec{p}\cdot\vec{x}} \langle\Omega|\mathcal{O}_j(\vec{y},\tau')\,\mathcal{O}_i(\vec{x},\tau)|\Omega\rangle, \tag{2.35}$$

where we have set the lattice spacing $a = 1$ for simplicity, and L^3 is the spatial volume of the lattice[3]. Note that due to the finite extent of the lattice, the available momenta p_i are multiples of $2\pi/L_i$, where L_i is the extent of the lattice component in the i^{th} direction. The spectral decomposition proceeds by insertion of a complete set of states between the operators

$$C\left(\vec{p}\,',\tau';\vec{p},\tau\right) = \sum_{\vec{x},\vec{y}}\sum_{n}\sum_{\vec{k}} \frac{e^{i\vec{p}\,'\cdot\vec{y}} e^{-i\vec{p}\cdot\vec{x}}}{2E_{n,\vec{k}}L^6} \left\langle\Omega\right| \mathcal{O}_j(\vec{y},\tau') \left|n,\vec{k}\right\rangle \left\langle n,\vec{k}\right| \mathcal{O}_i(\vec{x},\tau) \left|\Omega\right\rangle, \tag{2.36}$$

and the spacetime dependence of the source and sink operators may be separated as

$$\mathcal{O}(\vec{x},\tau) = e^{\hat{H}\tau + i\hat{\vec{p}}\cdot\vec{x}}\,\mathcal{O}\,e^{-\hat{H}\tau - i\hat{\vec{p}}\cdot\vec{x}}, \tag{2.37}$$

for the Hamiltonian and 3-momentum operators $\hat{H}$ and $\hat{\vec{p}}$ respectively. Substituting into Equation (2.36) gives

$$\begin{aligned} C\left(\vec{p}\,',\tau';\vec{p},\tau\right) = \sum_{\vec{x},\vec{y}}\sum_{n}\sum_{\vec{k}} \frac{e^{i\vec{p}\,'\cdot\vec{y}} e^{-i\vec{p}\cdot\vec{x}}}{2E_{n,\vec{k}}L^6} \left\langle\Omega\right| \mathcal{O}_j e^{-i\vec{k}\cdot\vec{y} - E_{n,\vec{k}}\tau'} \left|n,\vec{k}\right\rangle \\ \times \left\langle n,\vec{k}\right| e^{i\vec{k}\cdot\vec{x} + E_{n,\vec{k}}\tau} \mathcal{O}_i \left|\Omega\right\rangle. \end{aligned} \tag{2.38}$$

We may now perform the sums over $\vec{x}$ and $\vec{y}$, yielding momentum delta functions

$$C\left(\vec{p}\,',\tau';\vec{p},\tau\right) = \sum_{n}\sum_{\vec{k}} \frac{(2\pi)^6\,\delta^3(\vec{p}\,' - \vec{k})\,\delta^3(\vec{p} - \vec{k})}{2E_{n,\vec{k}}L^6} \left\langle\Omega\right| \mathcal{O}_j \left|n,\vec{k}\right\rangle$$

[3]It is implied here that the number of lattice sites in the x, y and z directions are equal, and this is true throughout this work.

$$\times \left\langle n, \vec{k} \right| \mathcal{O}_i \left| \Omega \right\rangle e^{-E_{n,\vec{k}}(\tau'-\tau)}. \tag{2.39}$$

Clearly this correlation function vanishes for $\vec{p}' \neq \vec{p}$, which is what we should expect from conservation of momentum. For the case $\vec{p}' = \vec{p}$ we get

$$C\left(\vec{p}, t\right) = \sum_n \frac{1}{2E_{n,\vec{p}}} \left\langle \Omega \right| \mathcal{O}_j \left| n, \vec{p} \right\rangle \left\langle n, \vec{p} \right| \mathcal{O}_i \left| \Omega \right\rangle e^{-E_{n,\vec{p}}\, t}, \tag{2.40}$$

which is the spectral decomposition of the two-point function. Since the energies are real and positive, in the limit of very large source and sink (Euclidean) time separations $t \equiv \tau' - \tau$, the ground state is resolved

$$C\left(\vec{p}, t\right) \to \frac{1}{2E_{0,\vec{p}}} \left\langle \Omega \right| \mathcal{O}_j \left| n = 0, \vec{p} \right\rangle \left\langle n = 0, \vec{p} \right| \mathcal{O}_i \left| \Omega \right\rangle e^{-E_{0,\vec{p}}\, t}. \tag{2.41}$$

This simple observation may be used to calculate hadron masses, for example, by choosing operators with appropriate quantum numbers[4] and projecting onto $\vec{p} = 0$, or to calculate matrix elements of a chosen operator.

A standard technique for studying ground state masses from correlation functions is the *effective energy* (or effective mass for $\vec{p} = 0$), whereby one constructs the combination

$$E_{eff} = \frac{1}{\delta t} \log \left(\frac{C(\vec{p}, t)}{C(\vec{p}, t + \delta t)} \right), \tag{2.42}$$

which converges to the lowest energy, $E_{0,\vec{p}}$, as $t \to \infty$. The region at which t is considered large enough to reliably extract the ground-state energy is usually determined by looking for so-called *plateaus*, where the effective energy has flattened out and can be fit to a constant value with fair goodness-of-fit. An example of a typical signal for a baryon two-point correlation function and its associated effective mass is presented in Figure 2.1. In the given example, the effective mass would suggest visually that the region $t \in [9, 16]$ contains the best-fit plateau, and this should be confirmed through calculation of a goodness-of-fit test statistic such as the χ^2/dof.

We note that in the above spectral decomposition which culminated with Equation (2.40), we have assumed that our operators have vanishing vacuum expectation values, which need not be true in general. For example, the scalar quark bilinear $\mathcal{O}_S = \bar{\psi}\psi$, as in our initial example, will retain the vacuum term entering with the complete set of states, and give a spectral decomposition

$$C_S\left(\vec{p}, t\right) = \left| \langle \Omega | \mathcal{O}_S | \Omega \rangle \right|^2 + \sum_n \frac{1}{2E_{n,\vec{p}}} \left| \langle n, \vec{p} | \mathcal{O}_S | \Omega \rangle \right|^2 e^{-E_{n,\vec{p}}\, t}. \tag{2.43}$$

[4] An operator must share the quantum numbers of the state which one wishes to resolve. See, for example, [62].

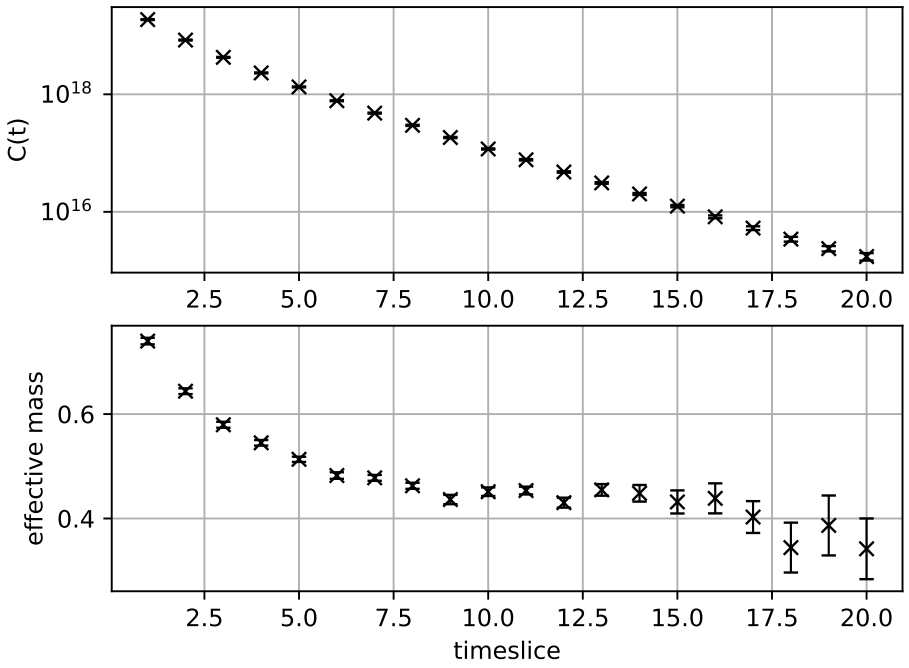

Figure 2.1: An example of a typical signal for a baryon two-point correlation function (top), and its corresponding effective mass (bottom) as defined in Equation (2.42) with $\delta t = 2$. By inspection, the ground-state mass would likely be extracted in the region $t \in [9, 16]$, as determined by a statistical analysis.

In this case one could simply account for this vacuum expectation value by fitting to a function of the form $A + Be^{-Et}$, at large t, in order to extract the ground state energy.

As a final remark on correlation functions we note that the boundary condition imposed in the time direction, which we take as anti-periodic for the quarks, results in the presence of a backwards propagating state for each state appearing in the spectral sum. It is often sufficient to ignore this state provided that the time extent of the lattice is great enough, and as such the number of sites in the time direction is typically chosen to be twice that of the spatial dimensions. If the backwards propagating states cannot be ignored at the precision of the calculation, the spectral decomposition may be updated to include them as

$$C\left(\vec{p}, t\right) = \sum_{n} \frac{1}{2E_{n,\vec{p}}} \left\langle \Omega \right| \mathcal{O}_f \left| n, \vec{p} \right\rangle \left\langle n, \vec{p} \right| \mathcal{O}_i \left| \Omega \right\rangle \left(e^{-E_{n,\vec{p}}\, t} + e^{-(T-t)E_{n,\vec{p}}} \right), \qquad (2.44)$$

with T the full Euclidean time extent of the lattice. In this thesis we find it advantageous to consider the backwards propagating states wherever mesons are concerned.

2.3 Mass tuning and gauge ensemble selection

The lattice simulations in this thesis are performed using three light flavours of dynamical[5] quark, which we endow with the physical electric charges of the up, down and strange quarks, although with an un-physically large QED coupling which will be discussed shortly. Because of the great simplification to our quark-mass extrapolation scheme, the flavour-breaking expansion [63], as well as improved precision for partially quenched[6] calculations, our desire is to start from a point of SU(3)-flavour symmetry, $m_u = m_d = m_s$, and hold the singlet quark mass fixed

$$\bar{m} = \frac{1}{3}(m_u + m_d + m_s) = \text{constant}. \tag{2.45}$$

Equation (2.45) defines a plane in the space of quark masses, and it is crucial that the plane defined by $\bar{m}$ contains[7] the physical point, i.e. the point where the quark masses result in physical values for sufficient ratios of hadron masses [64]. Due to the presence of QED however, it is not possible to achieve exact SU(3)-flavour symmetry since the up and down/strange quarks have different electric charges, and hence equal bare masses no longer results in degenerate quarks. Instead, when $m_d = m_s$ the residual flavour symmetry is called U-spin symmetry; the degeneracy of the down and strange quarks. We are instead left to choose an approximate SU(3)-flavour symmetric point, but still with exact U-spin symmetry [65], which we choose as

$$M^2_{u\bar{u}} = M^2_{d\bar{d}} = M^2_{s\bar{s}} = X^2_\pi, \tag{2.46}$$

where the first three masses-squared are for connected neutral pseudoscalar mesons with only up, down or strange valence quarks respectively, and

$$X^2_\pi = \frac{1}{6}\left[(M^\star_{K^+})^2 + (M^\star_{K^0})^2 + (M^\star_{K^-})^2 + (M^\star_{\bar{K}^0})^2 + (M^\star_{\pi^+})^2 + (M^\star_{\pi^-})^2\right]. \tag{2.47}$$

The $\star$ superscript denotes the experimental value of the corresponding meson mass. For this purpose the meson masses are calculated without disconnected contributions, which will be discussed at length in Chapter 5. The significance of the quantity X^2_π is that it is a mass combination which, according to its flavour-breaking mass parametrisation [63], will remain approximately constant on the plane defined by Equation (2.45) and hence fix the bare quark masses to the correct $\bar{m}$-plane.

The critical hopping parameter for each quark flavour, κ^c_f, is determined by extrapolating the corresponding meson mass-squared $M^2_{f\bar{f}}$ to zero using partially

[5] By 'dynamical' we mean that the determinant of the fermion matrix is included in the generation of the gauge ensembles (i.e. not quenched).

[6] 'Partial quenching' is where the bare mass of a dynamical quark is allowed to differ from that which is used in the valence quark fermion matrix upon inversion. Whilst this process incurs some quantifiable systematic error, it facilitates the calculation of quark propagators for additional masses without requiring the generation of new gauge ensembles.

[7] Since the physical point can only be determined on the lattice with finite accuracy, in practice the 'correct' $\bar{m}$ is determined to the precision required by the study.

quenched simulations, giving the bare quark mass

$$m_f(\kappa_f, q_f) = \frac{1}{2}\left(\frac{1}{\kappa_f} - \frac{1}{\kappa_f^c(q_f)}\right), \tag{2.48}$$

shown with explicit dependence on the quark's electric charge q_f. Our quark-mass extrapolation scheme for hadron properties, detailed in subsequent chapters, is made around the approximate SU(3)-symmetric point defined by Equation (2.46). The relevant deviations in quark mass from the approximate symmetric point are hence [65]

$$\delta m_f(\kappa_f, q_f) \equiv m_f(\kappa_f, q_f) - \bar{m} = \frac{1}{2}\left(\frac{1}{\kappa_f} - \frac{1}{\kappa_f^{syms}(q_f)}\right), \tag{2.49}$$

where κ_f^{syms} denotes the hopping parameter corresponding to $M_{f\bar{f}}^2 = X_\pi^2$. In terms of our expansion parameters, the constant-$\bar{m}$ surface condition implies

$$\delta m_u + \delta m_d + \delta m_s = 0. \tag{2.50}$$

The QCD+QED gauge ensembles we employ throughout this work are a mixture of $24^3 \times 48$, $32^3 \times 64$ and $48^3 \times 96$ volumes with three flavours of dynamical quark constrained to the constant-$\bar{m}$ plane containing the approximate SU(3)-symmetric point with

$$\kappa_u^{syms} = 0.124362, \quad \kappa_{d/s}^{syms} = 0.121713. \tag{2.51}$$

The coupling constants are $\beta_{\text{QCD}} = 5.50$ and $\beta_{\text{QED}} = 0.8$, which corresponds to a QED coupling of $\alpha_{\text{QED}} \approx 0.1$ that is much larger than the physical $1/137$. This was chosen to help ensure that we could observe qualitative QED effects in our lattice results, which are understood to be much smaller than the QCD contributions in hadron spectroscopy. Where quantitative QED effects are desired in later chapters we discuss correcting for our un-physically large coupling therein. The lattice spacing has been determined on $32^3 \times 64$ and $48^3 \times 96$ volumes as $a^{-1} = 2.89(5)\,\text{GeV}$ and $a^{-1} = 2.91(3)\,\text{GeV}$ respectively by comparing the value of aX_π, extrapolated to the physical point using the flavour-breaking expansion, with the experimental value X_π [65].

Where the partially quenched approximation is used in Chapter 3, the valence and sea quarks are confined to the same constant-$\bar{m}$ plane. Since the primary aim of the results herein is to study the nature of hadron properties under broken flavour-symmetry, the ensembles are largely focused near to the approximate symmetric point, where flavour-breaking leads to more pronounced consequences, with some more heavily flavour-breaking ensembles used to improve quark-mass parametrisations. More detailed information about the lattice simulations used to obtain results in each chapter can be found therein.

Chapter 3

Σ^0–Λ state mixing

The first classification of the low-lying hadronic states in terms of their valence quark structure was given by the eight-fold way [16], and is based on SU(3)-flavour symmetry. This idea is still useful today, however SU(3)-flavour symmetry is broken in nature by the non-degenerate bare masses and charges of the up, down and strange quarks. In particular, it is understood that isospin (also denoted T-spin [66]) is only approximately realised in nature, and so idealised hadronic states such as the Σ^0 and Λ, which differ only in their isospin eigenvalues, are permitted to mix to form the physical mass eigenstates. This mixing is typically parametrised by a *mixing angle*, and we will detail this parametrisation in the following section.

The extent to which the Σ^0 and Λ mix depends upon the severity of isospin breaking, as well as the residual and much greater SU(3) symmetry breaking by the strange quark. One approach in calculating the Σ^0–Λ mixing, due to Dalitz and Von Hippel (denoted DvH [34]), is based on relationships between the electromagnetic mass-splittings of octet baryons. This was derived through consideration of an effective Lagrangian density exhibiting SU(3)-flavour symmetry plus a perturbation which encodes bare quark mass and QED effects [67], and uses experimental baryon masses as inputs. Because of this, separate QCD and QED contributions cannot be approximated within this framework alone. A similar approach is employed in [68]. In pure QCD, there is a well-known result for the mixing from χPT [35, 69], and a previous determination in lattice QCD [36, 70, 71], with all existing results giving a mixing angle in the range $\approx 0.5°$–$1°$.

Our aim herein is to study the extent and quality of the state mixing between the Σ^0 and Λ baryons on the lattice, and in particular the distinct contributions from both QCD and QED. We describe and perform calculations using a novel method that focuses on the eigenvectors obtained from a variational analysis of a matrix of correlation functions, and derive a quark-mass expansion formula which is used to give preliminary results at the physical quark masses. The work presented in this chapter is the subject of our publication [72].

3.1 Lattice computation of Σ^0–Λ mixing

We will now describe the process by which we have probed the Σ^0–Λ state mixing in lattice QCD+QED. The underlying premise is to study the diagonalization of the variational matrix of correlation functions defined with respect to different (local) source and sink interpolating operators for the Σ^0 and Λ.

Throughout this chapter we often discuss variation of the light quark masses and charges, or discuss degeneracies of the quarks. Whilst obviously the physical quarks have fixed mass and charge parameters up to renormalisation, lattice simulations such as ours often use unphysical quark masses and charges for ease of calculation, and it therefore becomes natural to consider how quantities might change under variation of these parameters.

3.1.1 Interpolating operators and correlation functions

In this section we will explore the roles of other SU(2) subgroups in addition to isospin, and so in our present discussion we use the placeholder labels a, b and c in place of the three light quark flavours. Following the notation introduced in [36], we employ a basis of standard Euclidean-space interpolating operators for the SU(3) Σ^0 and Λ octet baryons with flavour content a, b, c,

$$\mathcal{B}_{\Sigma(abc)}(x)_\alpha = \frac{1}{\sqrt{2}}\epsilon^{lmn}\big(b(x)^l_\alpha \left[a(x)^{m\top}C\gamma^5 c(x)^n\right] + a(x)^l_\alpha \left[b(x)^{m\top}C\gamma^5 c(x)^n\right]\big), \quad (3.1)$$

and

$$\mathcal{B}_{\Lambda(abc)}(x)_\alpha = \frac{1}{\sqrt{6}}\epsilon^{lmn}\big(2c(x)^l_\alpha \left[a(x)^{m\top}C\gamma^5 b(x)^n\right] + b(x)^l_\alpha \left[a(x)^{m\top}C\gamma^5 c(x)^n\right]$$
$$-a^l_\alpha(x) \left[b^m(x)^\top C\gamma^5 c^n(x)\right]\big), \quad (3.2)$$

where $C = \gamma_2\gamma_4$, the superscript $\top$ denotes a transpose in Dirac space, l, m and n are colour indices and α a Dirac index. Note that the position of the flavour labels is important here. These operators are constructed to exhibit the necessary colour antisymmetry and definite SU(2) symmetry in the quark flavours a and b; symmetric under an interchange of a and b for the Σ operator and antisymmetric for the Λ. The three choices of Cartan subalgebra for SU(3)-flavour [73], T-, V- and U-spin (see [74]), correspond to replacement of the placeholder flavours a/b by u/d, u/s and d/s respectively. Evident in the opposing symmetries of these two operators under the interchange of a and b; if the a and b quarks are degenerate, these operators are orthogonal and there is no Σ^0–Λ mixing.

We use these operators to form the 2×2 matrix of correlation functions with elements

$$C_{ij}(t) = \sum_{\vec{y}} \mathrm{Tr}_D \Gamma_{unpol} \left\langle 0|\mathcal{B}_i(\vec{y},t)\bar{\mathcal{B}}_j(\vec{x}_0,0)|0\right\rangle, \quad (3.3)$$

where $\Gamma_{unpol} = (1+\gamma_4)/2$, Tr_D denotes a trace in Dirac (spin) indices, and i and j enumerate the operator labels $\Sigma(abc)$ and $\Lambda(abc)$.

The correlation functions are calculated in lattice QCD+QED via Wick's theorem, whereby the correlation functions may be written in terms of lattice quark propagators, with the gauge ensemble average implied. Explicitly,

$$C_{\Sigma(abc)\Sigma(abc)}(t) = \sum_{\vec{y}} \mathrm{Tr}_D \Gamma_{unpol} \Big\langle \mathcal{B}_{\Sigma(abc)}(\vec{y},t)\, \bar{\mathcal{B}}_{\Sigma(abc)}(\vec{x}_0,0) \Big\rangle = \sum_{\vec{y}} \frac{\epsilon^{lmn}\epsilon^{l'm'n'}}{2} \times$$

$$\Bigg(\mathrm{Tr}_D \Big[\Gamma_{unpol}\, S_a(\vec{y},t;\vec{x}_0,0)^{ll'} \Big]\, \mathrm{Tr}_D \Big[S_b^\top(\vec{y},t;\vec{x}_0,0)^{mm'}\, C\gamma^5\, S_c(\vec{y},t;\vec{x}_0,0)^{nn'}\, \gamma^5 C \Big] +$$

$$\mathrm{Tr}_D \Big[\Gamma_{unpol}\, S_b(\vec{y},t;\vec{x}_0,0)^{ll'} \Big]\, \mathrm{Tr}_D \Big[S_a^\top(\vec{y},t;\vec{x}_0,0)^{mm'}\, C\gamma^5\, S_c(\vec{y},t;\vec{x}_0,0)^{nn'}\, \gamma^5 C \Big] +$$

$$\mathrm{Tr}_D \Big[\Gamma_{unpol}\, S_b(\vec{y},t;\vec{x}_0,0)^{lm'}\, C\gamma^5 S_c^\top(\vec{y},t;\vec{x}_0,0)^{nn'}\, \gamma^5 C\, S_a(\vec{y},t;\vec{x}_0,0)^{ml'} \Big] +$$

$$\mathrm{Tr}_D \Big[\Gamma_{unpol}\, S_a(\vec{y},t;\vec{x}_0,0)^{lm'}\, C\gamma^5 S_c^\top(\vec{y},t;\vec{x}_0,0)^{nn'}\, \gamma^5 C\, S_b(\vec{y},t;\vec{x}_0,0)^{ml'} \Big] \Bigg), \tag{3.4}$$

where $S_f(y;x_0)$ is the point-to-all quark propagator of Equation (2.33), from source $x_0 = (\vec{x}_0, 0)$ to sink $y = (\vec{y}, t)$, for a quark of flavour f. The other diagonal entry of our correlation function matrix evaluates to

$$C_{\Lambda(abc)\Lambda(abc)}(t) = \sum_{\vec{y}} \frac{\epsilon^{lmn}\epsilon^{l'm'n'}}{6} \times$$

$$\Bigg(4\mathrm{Tr}_D \Big[\Gamma_{unpol}\, S_c(\vec{y},t;\vec{x}_0,0)^{ll'} \Big]\, \mathrm{Tr}_D \Big[S_b^\top(\vec{y},t;\vec{x}_0,0)^{mm'}\, C\gamma^5\, S_a(\vec{y},t;\vec{x}_0,0)^{nn'}\, \gamma^5 C \Big] +$$

$$\mathrm{Tr}_D \Big[\Gamma_{unpol}\, S_a(\vec{y},t;\vec{x}_0,0)^{ll'} \Big]\, \mathrm{Tr}_D \Big[S_b^\top(\vec{y},t;\vec{x}_0,0)^{mm'}\, C\gamma^5\, S_c(\vec{y},t;\vec{x}_0,0)^{nn'}\, \gamma^5 C \Big] +$$

$$\mathrm{Tr}_D \Big[\Gamma_{unpol}\, S_b(\vec{y},t;\vec{x}_0,0)^{ll'} \Big]\, \mathrm{Tr}_D \Big[S_a^\top(\vec{y},t;\vec{x}_0,0)^{mm'}\, C\gamma^5\, S_c(\vec{y},t;\vec{x}_0,0)^{nn'}\, \gamma^5 C \Big] +$$

$$2\mathrm{Tr}_D \Big[\Gamma_{unpol}\, S_c(\vec{y},t;\vec{x}_0,0)^{lm'}\, C\gamma^5 S_a^\top(\vec{y},t;\vec{x}_0,0)^{nn'}\, \gamma^5 C\, S_b(\vec{y},t;\vec{x}_0,0)^{ml'} \Big] +$$

$$2\mathrm{Tr}_D \Big[\Gamma_{unpol}\, S_c(\vec{y},t;\vec{x}_0,0)^{lm'}\, C\gamma^5 S_b^\top(\vec{y},t;\vec{x}_0,0)^{nn'}\, \gamma^5 C\, S_a(\vec{y},t;\vec{x}_0,0)^{ml'} \Big] +$$

$$2\mathrm{Tr}_D \Big[\Gamma_{unpol}\, S_b(\vec{y},t;\vec{x}_0,0)^{lm'}\, C\gamma^5 S_a^\top(\vec{y},t;\vec{x}_0,0)^{nn'}\, \gamma^5 C\, S_c(\vec{y},t;\vec{x}_0,0)^{ml'} \Big] +$$

$$2\mathrm{Tr}_D \Big[\Gamma_{unpol}\, S_a(\vec{y},t;\vec{x}_0,0)^{lm'}\, C\gamma^5 S_b^\top(\vec{y},t;\vec{x}_0,0)^{nn'}\, \gamma^5 C\, S_c(\vec{y},t;\vec{x}_0,0)^{ml'} \Big] -$$

$$\mathrm{Tr}_D \Big[\Gamma_{unpol}\, S_b(\vec{y},t;\vec{x}_0,0)^{lm'}\, C\gamma^5 S_c^\top(\vec{y},t;\vec{x}_0,0)^{nn'}\, \gamma^5 C\, S_a(\vec{y},t;\vec{x}_0,0)^{ml'} \Big] -$$

$$\left. \mathrm{Tr}_D \left[\Gamma_{unpol} \, S_a(\vec{y},t;\vec{x}_0,0)^{lm'} \, C\gamma^5 S_c^{\top}(\vec{y},t;\vec{x}_0,0)^{nn'} \, \gamma^5 C \, S_b(\vec{y},t;\vec{x}_0,0)^{ml'} \right] \right), \tag{3.5}$$

and the two off-diagonal entries, which are numerically equal, give

$$C_{\Sigma(abc)\Lambda(abc)}(t) = C_{\Lambda(abc)\Sigma(abc)}(t) = \sum_{\vec{y}} \frac{\epsilon^{lmn}\epsilon^{l'm'n'}}{2\sqrt{3}} \times$$

$$\begin{aligned}
\Big(& \mathrm{Tr}_D \left[\Gamma_{unpol} \, S_b(\vec{y},t;\vec{x}_0,0)^{ll'} \right] \mathrm{Tr}_D \left[S_a^{\top}(\vec{y},t;\vec{x}_0,0)^{mm'} \, C\gamma^5 \, S_c(\vec{y},t;\vec{x}_0,0)^{nn'} \, \gamma^5 C \right] - \\
& \mathrm{Tr}_D \left[\Gamma_{unpol} \, S_a(\vec{y},t;\vec{x}_0,0)^{ll'} \right] \mathrm{Tr}_D \left[S_b^{\top}(\vec{y},t;\vec{x}_0,0)^{mm'} \, C\gamma^5 \, S_c(\vec{y},t;\vec{x}_0,0)^{nn'} \, \gamma^5 C \right] + \\
& 2\mathrm{Tr}_D \left[\Gamma_{unpol} \, S_b(\vec{y},t;\vec{x}_0,0)^{lm'} \, C\gamma^5 S_a^{\top}(\vec{y},t;\vec{x}_0,0)^{nn'} \, \gamma^5 C \, S_c(\vec{y},t;\vec{x}_0,0)^{ml'} \right] - \\
& 2\mathrm{Tr}_D \left[\Gamma_{unpol} \, S_a(\vec{y},t;\vec{x}_0,0)^{lm'} \, C\gamma^5 S_b^{\top}(\vec{y},t;\vec{x}_0,0)^{nn'} \, \gamma^5 C \, S_c(\vec{y},t;\vec{x}_0,0)^{ml'} \right] - \\
& \mathrm{Tr}_D \left[\Gamma_{unpol} \, S_b(\vec{y},t;\vec{x}_0,0)^{lm'} \, C\gamma^5 S_c^{\top}(\vec{y},t;\vec{x}_0,0)^{nn'} \, \gamma^5 C \, S_a(\vec{y},t;\vec{x}_0,0)^{ml'} \right] + \\
& \mathrm{Tr}_D \left[\Gamma_{unpol} \, S_a(\vec{y},t;\vec{x}_0,0)^{lm'} \, C\gamma^5 S_c^{\top}(\vec{y},t;\vec{x}_0,0)^{nn'} \, \gamma^5 C \, S_b(\vec{y},t;\vec{x}_0,0)^{ml'} \right] \Big).
\end{aligned} \tag{3.6}$$

It is easily confirmed by observation that the correlation functions $C_{\Sigma(abc)\Sigma(abc)}(t)$ and $C_{\Lambda(abc)\Lambda(abc)}(t)$ are symmetric under the interchange of a and b quarks, whilst $C_{\Sigma(abc)\Lambda(abc)}(t)$ is antisymmetric, as is required by the symmetries of the interpolating operators. The distinct flavours a and a' do not contract under Wick's theorem but are otherwise degenerate, and hence $S_a(y;x) = S_{a'}(y;x)$, so that $C_{\Sigma(aa'c)\Lambda(aa'c)}(t) = 0$. This is equivalent to there being no Σ^0–Λ state mixing when the elected Cartan subalgebra corresponds to an exact symmetry. Moreover, if all three light quark flavours are degenerate, then

$$C_{\Sigma(aa'a'')\Sigma(aa'a'')}(t) = C_{\Lambda(aa'a'')\Lambda(aa'a'')}(t), \tag{3.7}$$

and the correlation function matrix is proportional to the 2×2 identity.

An additional relation which we will use in our quark mass extrapolation scheme, and which can also be inferred from the underlying SU(3) group theory or confirmed from the detailed correlation function expressions, is

$$\begin{aligned}
\begin{bmatrix} C_{\Sigma(aba')\Sigma(aba')} & C_{\Sigma(aba')\Lambda(aba')} \\ C_{\Lambda(aba')\Sigma(aba')} & C_{\Lambda(aba')\Lambda(aba')} \end{bmatrix} &= U \begin{bmatrix} C_{\Sigma(aa'b)\Sigma(aa'b)} & 0 \\ 0 & C_{\Lambda(aa'b)\Lambda(aa'b)} \end{bmatrix} U^T \\
&= \begin{bmatrix} \frac{1}{2} & \frac{\sqrt{3}}{2} \\ \frac{-\sqrt{3}}{2} & \frac{1}{2} \end{bmatrix} \begin{bmatrix} C_{\Sigma(aa'b)\Sigma(aa'b)} & 0 \\ 0 & C_{\Lambda(aa'b)\Lambda(aa'b)} \end{bmatrix} \begin{bmatrix} \frac{1}{2} & \frac{-\sqrt{3}}{2} \\ \frac{\sqrt{3}}{2} & \frac{1}{2} \end{bmatrix}.
\end{aligned} \tag{3.8}$$

This relation indicates a simple and constant diagonalization whenever one of the relevant SU(2) symmetries is realised. For ease of comparison with later working we list the expanded relations:

$$C_{\Sigma(aba')\Sigma(aba')} = \frac{\left(3C_{\Lambda(aa'b)\Lambda(aa'b)} + C_{\Sigma(aa'b)\Sigma(aa'b)}\right)}{4} \tag{3.9}$$

$$C_{\Lambda(aba')\Lambda(aba')} = \frac{\left(3C_{\Sigma(aa'b)\Sigma(aa'b)} + C_{\Lambda(aa'b)\Lambda(aa'b)}\right)}{4} \tag{3.10}$$

$$C_{\Sigma(aba')\Lambda(aba')} = \frac{\sqrt{3}\left(C_{\Lambda(aa'b)\Lambda(aa'b)} - C_{\Sigma(aa'b)\Sigma(aa'b)}\right)}{4} \tag{3.11}$$

$$C_{\Lambda(aa'b)\Lambda(aa'b)} = \frac{\left(3C_{\Sigma(aba')\Sigma(aba')} - C_{\Lambda(aba')\Lambda(aba')}\right)}{2} \tag{3.12}$$

$$C_{\Sigma(aa'b)\Sigma(aa'b)} = \frac{\left(3C_{\Lambda(aba')\Lambda(aba')} - C_{\Sigma(aba')\Sigma(aba')}\right)}{2}. \tag{3.13}$$

3.1.2 Mixing angle and extrapolation scheme

In Section 3.1.1 we have detailed the lattice correlation functions which we are concerned with herein, and we will now discuss how we extract mixing information from them. We wish to find operators which couple diagonally to the Σ^0 and Λ, by which we mean $\langle 0|\mathcal{O}_i^\star|j\rangle \propto \delta_{ij}$ for some operators $\mathcal{O}^\star_{\Sigma^0}/\mathcal{O}^\star_\Lambda$ and physical states $|\Sigma^0\rangle/|\Lambda\rangle$. We denote the physical vacuum by $|0\rangle$.

We consider the eigenvalue problem (EVP)

$$C(t)\,\vec{v}_n(t) = \lambda_n(t)\,\vec{v}_n(t), \tag{3.14}$$

where $C(t)$ is the matrix of correlation functions with elements defined in Equation (3.3). It is more typical in variational studies to solve a generalized eigenvalue problem (GEVP; see [75,76]), however the eigenvectors which determine the mixing agree mathematically between the two methods in the large-time limit. Moreover, we find better signal quality for eigenvectors calculated from the EVP in the present study, as we will see.

At large Euclidean time the correlation functions of Equation (3.3) may be written with contributions from only the least energetic states which couple to our operators via the spectral decomposition,

$$\begin{aligned} C_{ij}(t) &= \sum_n \frac{1}{2M_n} \langle 0|\,\mathcal{B}_i\,|n\rangle\,\langle n|\,\bar{\mathcal{B}}_j\,|0\rangle\, e^{-M_n t} \\ &\approx \frac{1}{2M_{\Sigma^0}} \langle 0|\,\mathcal{B}_i\,|\Sigma^0\rangle\,\langle \Sigma^0|\,\bar{\mathcal{B}}_j\,|0\rangle\, e^{-M_{\Sigma^0} t} + \frac{1}{2M_\Lambda}\,\langle 0|\,\mathcal{B}_i\,|\Lambda\rangle\,\langle \Lambda|\,\bar{\mathcal{B}}_j\,|0\rangle\, e^{-M_\Lambda t}, \end{aligned} \tag{3.15}$$

with corrections beginning at $\mathcal{O}(\exp(-\Delta M\, t))$, where ΔM is the mass gap between the next-least-energetic state mass, M_3, and $\max\{M_{\Sigma^0}, M_\Lambda\}$: $\Delta M = M_3 - \max\{M_{\Sigma^0}, M_\Lambda\}$. In this limit the right eigenvectors of our real, symmetric matrix (Equation (3.14)) exhibit the property [75]

$$\sum_{j=1}^{2} \langle 0|\mathcal{B}_j|n\rangle\, [\vec{v}_m]_j \propto \delta_{nm}, \quad \sum_{j=1}^{2} [\vec{v}_m]_j\, \langle n|\bar{\mathcal{B}}_j|0\rangle \propto \delta_{nm}, \tag{3.16}$$

for $n = \Sigma^0, \Lambda$ and $\{\mathcal{B}_1, \mathcal{B}_2\} = \{\mathcal{B}_{\Sigma^0}, \mathcal{B}_\Lambda\}$, and hence we can form our diagonalizing operators as

$$\mathcal{O}^\star_{\Sigma^0} \equiv \sum_{j=1}^{2} [\vec{v}_{\Sigma^0}]_j\, \mathcal{B}_j, \quad \mathcal{O}^\star_\Lambda \equiv \sum_{j=1}^{2} [\vec{v}_\Lambda]_j\, \mathcal{B}_j. \tag{3.17}$$

The 2×2 matrix with columns one and two being the orthogonal, normalized-to-unity eigenvectors $\vec{v}_{\Sigma^0}$ and $\vec{v}_\Lambda$ respectively, can be viewed as a rotation matrix that acts to rotate our basis of standard interpolating operators into a pair which couple diagonally to the Σ^0 and Λ eigenstates. It is therefore natural to parametrise this rotation by a single mixing angle, which we call the Σ–Λ mixing angle and denote $\theta_{\Sigma\Lambda}$:

$$\begin{bmatrix} [\vec{v}_{\Sigma^0}]_1 & [\vec{v}_\Lambda]_1 \\ [\vec{v}_{\Sigma^0}]_2 & [\vec{v}_\Lambda]_2 \end{bmatrix} = \begin{bmatrix} \cos\theta_{\Sigma\Lambda} & -\sin\theta_{\Sigma\Lambda} \\ \sin\theta_{\Sigma\Lambda} & \cos\theta_{\Sigma\Lambda} \end{bmatrix}. \tag{3.18}$$

Mixing angle mass parametrisation

Typically the most significant systematic error in lattice calculations is the heavier-than-physical quark masses used to reduce the computational cost of inverting the Fermion matrix. Because of this and in order to present a good estimate of a physical quantity using lattice results, it is often necessary to extrapolate the quantity from the unphysical quark masses used in the simulations to the physical masses, which requires a functional relationship between those masses and the quantity of interest.

In this work we derive a parametrisation for the mixing angle $\theta_{\Sigma\Lambda}$ in terms of the up, down and strange quark masses and charges. Since there is no mixing when the light quarks have equal masses and charges (i.e. SU(3)-flavour symmetry is realised), we consider the mixing angle induced by mass and charge perturbations 'near' a configuration of equal-mass light quarks without charge. We denote the deviation of the quark mass of flavour i from the SU(3)-symmetric point by $\delta m_i = m_i - m_0$, where m_0 is the bare quark mass of all flavours at the SU(3)-symmetric point. We restrict perturbations in the quark charges to ϵQ_i, proportional to the $i = u, d, s$ physical charges, Q_i, but scaled by the small parameter ϵ (so as to keep their ratios physical). This ensures that as we introduce perturbations in the quark charges simultaneously via ϵ, we retain the physical U-spin symmetry with respect to QED, and reduce the number of parameters, from the three that would be required to describe independent variations of the charges, to one.

Since we have found that the eigenvectors of the matrix of correlation functions encode the mixing angle, we endeavour to Taylor expand the matrix of correlation functions itself about the aforementioned SU(3)-symmetric point, now denoting its explicit dependence on the quark masses and charges as

$$C(t) \longrightarrow C(t, m_a, m_b, m_c, e_a, e_b, e_c) \quad \text{or} \quad C(t, \vec{m}_{abc}, \vec{e}_{abc}), \tag{3.19}$$

where the ordering of mass and charge labels corresponds to the order of flavour labels for the individual correlation functions: $C(t, \vec{m}_{abc}, \vec{e}_{abc})$ has elements $C_{ij}(t)$ for $i, j = \Sigma(abc), \Lambda(abc)$. We will also drop the explicit time-dependence of the correlation functions for the present discussion and take relations between time-dependent quantities to be at equal Euclidean time.

Explicitly considering the isospin ordering uds[1] and Taylor expanding to first order in ϵ gives

$$\begin{aligned} C(\vec{m}_{uds,0}, \epsilon\vec{Q}_{uds}) &\simeq C(\vec{m}_{uds,0}, 0) + \left[\begin{array}{cc} \frac{\partial C_{\Sigma\Sigma}(\vec{m}_{uds,0}, \epsilon\vec{Q}_{uds})}{\partial\epsilon} & \frac{\partial C_{\Sigma\Lambda}(\vec{m}_{uds,0}, \epsilon\vec{Q}_{uds})}{\partial\epsilon} \\ \frac{\partial C_{\Lambda\Sigma}(\vec{m}_{uds,0}, \epsilon\vec{Q}_{uds})}{\partial\epsilon} & \frac{\partial C_{\Lambda\Lambda}(\vec{m}_{uds,0}, \epsilon\vec{Q}_{uds})}{\partial\epsilon} \end{array}\right] \Bigg|_{\epsilon=0} \epsilon \\ &= C(\vec{m}_{uds,0}, 0) + \frac{S}{2}\begin{bmatrix} 1 & 0 \\ 0 & 1 \end{bmatrix} + \frac{D_{\text{QED}}}{4}\begin{bmatrix} -1 & \sqrt{3} \\ \sqrt{3} & 1 \end{bmatrix}, \end{aligned} \tag{3.20}$$

where $\vec{m}_{uds,0} = (m_0, m_0, m_0)$ and

$$S \equiv \epsilon\left(\frac{\partial C_{\Sigma\Sigma}(\vec{m}_{dsu,0}, \epsilon\vec{Q}_{dsu})}{\partial\epsilon} + \frac{\partial C_{\Lambda\Lambda}(\vec{m}_{dsu,0}, \epsilon\vec{Q}_{dsu})}{\partial\epsilon}\right)\Big|_{\epsilon=0} \tag{3.21}$$

$$D_{\text{QED}} \equiv \epsilon\left(\frac{\partial C_{\Sigma\Sigma}(\vec{m}_{dsu,0}, \epsilon\vec{Q}_{dsu})}{\partial\epsilon} - \frac{\partial C_{\Lambda\Lambda}(\vec{m}_{dsu,0}, \epsilon\vec{Q}_{dsu})}{\partial\epsilon}\right)\Big|_{\epsilon=0}. \tag{3.22}$$

We have used Equations (3.9)–(3.11) to eliminate the three independent isospin correlation functions in favour of two U-spin correlation functions. In doing this we have also isolated a contribution proportional to the identity which will have no effect on the eigenvectors. Note that, as previously expressed, $C(\vec{m}_{uds,0}, 0)$ is also proportional to the identity.

Now considering first order perturbations in the light quark masses we find

$$\begin{aligned} C_{ij}(\vec{m}_{uds}, 0) \simeq C_{ij}(\vec{m}_{uds,0}, 0) &+ \left(\frac{\partial C_{ij}(\vec{m}_{uds}, 0)}{\partial m_u}\Big|_{\vec{m}_{uds,0},0}\right)\delta m_u + \\ &\left(\frac{\partial C_{ij}(\vec{m}_{uds}, 0)}{\partial m_d}\Big|_{\vec{m}_{uds,0}}\right)\delta m_d + \left(\frac{\partial C_{ij}(\vec{m}_{uds}, 0)}{\partial m_s}\Big|_{\vec{m}_{uds,0}}\right)\delta m_s \end{aligned}$$

[1]Note that dus is also isospin, and we know that the corresponding matrix of correlation functions simply acquires a minus sign on its off-diagonal components under u–d interchange.

$$= C_{ij}(\vec{m}_{uds,0}) + \left(U^T_{ik} \frac{\partial C_{kl}(\vec{m}_{uds})}{\partial m_s}\Big|_{\vec{m}_{uds,0}} U_{lj} \right) \delta m_u + \left(U_{ik} \frac{\partial C_{kl}(\vec{m}_{uds})}{\partial m_s}\Big|_{\vec{m}_{uds,0}} U^T_{lj} \right) \delta m_d + \left(\frac{\partial C_{ij}(\vec{m}_{uds})}{\partial m_s}\Big|_{\vec{m}_{uds,0}} \right) \delta m_s, \tag{3.23}$$

where the repeated indices k and l are summed over, and the matrix U is defined in Equation (3.8). If we now eliminate δm_s using the condition $\bar{m} = constant$, the above expression reduces to

$$C(\vec{m}_{uds}, 0) \simeq C(\vec{m}_{uds,0}, 0) + \frac{D_{\mathrm{QCD}}}{4} \begin{bmatrix} -3(\delta m_u + \delta m_d) & \sqrt{3}(\delta m_u - \delta m_d) \\ \sqrt{3}(\delta m_u - \delta m_d) & 3(\delta m_u + \delta m_d) \end{bmatrix}, \tag{3.24}$$

where

$$D_{\mathrm{QCD}} = \left(\frac{\partial C_{\Sigma\Sigma}(\vec{m}_{uds}, 0)}{\partial m_s} - \frac{\partial C_{\Lambda\Lambda}(\vec{m}_{uds}, 0)}{\partial m_s} \right)\Big|_{\vec{m}_{uds} = \vec{m}_{uds,0}}. \tag{3.25}$$

Comparing Equation (3.24) with the flavour-breaking expression presented in [36], for the parameter A_2 used therein, at large Euclidean times we must have $D_{\mathrm{QCD}}(t) = 2A_2$.

Simply combining our expansions for mass and charge perturbations of the matrix of isospin correlation functions, our first order parametrisation is

$$C(\vec{m}_{uds}, \epsilon\vec{Q}_{uds}) \simeq C(\vec{m}_{uds,0}, 0) + \frac{S}{2} \begin{bmatrix} 1 & 0 \\ 0 & 1 \end{bmatrix} + \frac{D_{\mathrm{QED}}}{4} \begin{bmatrix} -1 & \sqrt{3} \\ \sqrt{3} & 1 \end{bmatrix} + \frac{D_{\mathrm{QCD}}}{4} \begin{bmatrix} -3(\delta m_u + \delta m_d) & \sqrt{3}(\delta m_u - \delta m_d) \\ \sqrt{3}(\delta m_u - \delta m_d) & 3(\delta m_u + \delta m_d) \end{bmatrix}. \tag{3.26}$$

We will see that, for the lattice ensembles considered, a first order parametrisation is sufficient to describe our results.

Finally, we can calculate the eigenvectors of Equation (3.26) symbolically to determine the mixing angle in terms of our expansion parameters, yielding

$$\tan 2\theta_{\Sigma\Lambda,\mathrm{isospin}} = -\sqrt{3} \left(\frac{D_{\mathrm{QCD}}(\delta m_u - \delta m_d) + D_{\mathrm{QED}}}{3D_{\mathrm{QCD}}(\delta m_u + \delta m_d) + D_{\mathrm{QED}}} \right). \tag{3.27}$$

This derivation process can now be repeated for the matrices of U- and V-spin correlation functions, with the final results being

$$\tan 2\theta_{\Sigma\Lambda,\text{V-spin}} = \sqrt{3} \left(\frac{D_{\mathrm{QCD}}(\delta m_u - \delta m_s) + D_{\mathrm{QED}}}{3D_{\mathrm{QCD}}(\delta m_u + \delta m_s) + D_{\mathrm{QED}}} \right) \tag{3.28}$$

$$\tan 2\theta_{\Sigma\Lambda,\text{U-spin}} = \frac{\sqrt{3} D_{\mathrm{QCD}}(\delta m_d - \delta m_s)}{3D_{\mathrm{QCD}}(\delta m_d + \delta m_s) + 4D^{\text{U-spin}}_{\mathrm{QED}}}, \tag{3.29}$$

where $D_{\text{QED}}^{\text{U-spin}}$ is similar to D_{QED}, only with derivatives of correlation functions of definite isospin instead of U-spin,

$$D_{\text{QED}}^{\text{U-spin}} \equiv \epsilon \left(\frac{\partial C_{\Sigma\Sigma}(\vec{m}_{uds,0}, \epsilon\vec{Q}_{uds})}{\partial\epsilon} - \frac{\partial C_{\Lambda\Lambda}(\vec{m}_{uds,0}, \epsilon\vec{Q}_{uds})}{\partial\epsilon} \right)\Big|_{\epsilon=0}. \tag{3.30}$$

We remark that we have absorbed the quark charge expansion parameter ϵ into the QED fit parameters since we are not varying the quark charges in our lattice simulations. Notice that for each of the above mixing angle expressions in the absence of QED, $D_{\text{QED}} = D_{\text{QED}}^{\text{U-spin}} = 0$, the parameter D_{QCD} cancels and the remaining expressions contain no parameters with implicit time dependence, and depend only on the quark masses. Moreover, the isospin expression without QED returns the leading-order χPT result [35], as well as the leading-order term presented in [36] derived via a more group-theoretic approach. It is interesting to note that the lattice data used to fit the parametrisation in [36] were the Σ^0 and Λ masses, whereas we are herein fitting directly to the mixing angles.

Where the QED coupling is non-zero, and our mixing angles depend on parameters which themselves depend implicitly on Euclidean time, we take the standard approach of fitting the mixing angles at large Euclidean times, where the ground states Σ^0 and Λ are expected to dominate the spectral sum as in Equation (3.15). Since the eigenvector elements are given functionally by ratios of correlation functions with very similar time dependence, especially near to the SU(3)-symmetric point, their resulting time dependence is observed to be very weak.

Running quark masses

Since we have included QED in our lattice calculations and we have quarks of differing charges, we must consider that numerically-equal variations of the bare quark masses will no longer result in equal variations of the renormalised quark masses. Because of this we include an additional parameter in our fit function which comes from making the substitution

$$\delta m_u + \delta m_d + \delta m_s = 0 \quad \rightarrow \quad \frac{1}{Z_{2/3}}\delta m_u + \frac{1}{Z_{-1/3}}(\delta m_d + \delta m_s) = 0, \tag{3.31}$$

where the introduced renormalisation factors Z_i correct for the running of the quark masses due to QED, analogous to the Dashen scheme introduced in [65]. In particular, the renormalisation factors account for the different variations of the up and down/strange quark propagators due to equal variations of their underlying bare quark masses.

Upon substituting the renormalised quark masses into our mixing expressions of Equations (3.27)–(3.29), we have our final parametrisations

$$\tan 2\theta_{\Sigma\Lambda,\text{isospin}} = \sqrt{3}\left(\frac{(\delta m_u - Z\delta m_d) + D_{\text{QED}}/D_{\text{QCD}}}{3(\delta m_u + Z\delta m_d) + D_{\text{QED}}/D_{\text{QCD}}} \right) \tag{3.32}$$

$$\tan 2\theta_{\Sigma\Lambda,\text{V-spin}} = \sqrt{3}\left(\frac{(\delta m_u - Z\delta m_s) + D_{\text{QED}}/D_{\text{QCD}}}{3(\delta m_u + Z\delta m_s) + D_{\text{QED}}/D_{\text{QCD}}}\right) \tag{3.33}$$

$$\tan 2\theta_{\Sigma\Lambda,\text{U-spin}} = \frac{\sqrt{3}(\delta m_d - \delta m_s)}{3(\delta m_d + \delta m_s) + 4D_{\text{QED}}^{\text{U-spin}}/D_{\text{QCD}}}, \tag{3.34}$$

where we have defined $Z \equiv \frac{Z_{2/3}}{Z_{-1/3}}$, and absorbed factors of $Z_{2/3}$ and $Z_{-1/3}$ into the fit parameters D_{QED} and $D_{\text{QED}}^{\text{U-spin}}$ respectively. We have now derived first-order quark mass and charge expansions for mixing angles with respect to T-, U- and V-spin SU(3) operator bases, sharing a total of three independent parameters, that can be determined via a fit across various values of the light quark masses.

Continuing the expansion of the correlation function matrix we find that second order QCD requires two additional parameters, with further parameters needed for leading-order mixed QCD–QED terms. As for pure QED terms at next order, in theory it is possible to replace

$$D_{\text{QED}} \to \left[\sum_{n=0}^{\infty} \frac{1}{(n+1)!}\left(\epsilon\frac{\partial}{\partial\epsilon}\right)^n\right] D_{\text{QED}}, \tag{3.35}$$

and absorb all orders of the QED expansion into our existing functional form, since we do not wish to vary ϵ in our extrapolation and the matrix structure of all higher-order terms is identical. However, we do not claim to have properly included these higher order terms herein as our lattice ensembles possess a much larger-than-physical EM coupling. This leads us to scale our QED fit parameters using a linear ansatz, and hence cannot be expected to be consistent with precision beyond leading order. We currently forgo the inclusion of any higher-order terms and as we will see, the first order expressions are suitable to describe our lattice data.

3.2 Results

The lattice ensembles used for this study have been selected to focus on the region near an approximate SU(3)-flavour symmetry, and this point, as well as the strong and EM couplings, are described in Section 2.3. Given the differences in quark charges, this symmetry cannot be exact, and our approach is to tune the neutral (connected) pseudoscalar mesons to be degenerate [65]. Starting from this configuration of bare quark masses, the approximate symmetry is further broken along a trajectory that leaves no residual invariant (or approximate invariant) SU(2) subgroup. In particular, we introduce a breaking $m_u - m_s$, while holding both m_d and the average quark mass $\bar{m}$ fixed. In this way we preserve the physical mass hierarchy, $m_u < m_d < m_s$. To further improve the constraint on our expansion parameters we also consider partially-quenched (PQ) propagators, where the valence masses are allowed to vary independently of the simulated sea quarks. The simulation parameters used in this chapter are listed in Table 3.1.

Lattice Ensembles					
$L^3 \cdot N_t$	κ_u	κ_d	κ_s	$\theta_{\Sigma\Lambda,\text{isospin}}$	$M_{u\bar{u}}$ (MeV)
$24^3 \cdot 48$	**0.124362**	**0.121713**	**0.121713**	-30°	442(9)
$24^3 \cdot 48$	**0.124374**	**0.121713**	**0.121701**	-21.8(1.1)°	423(9)
	0.124387	0.121713	0.121689	-19.5(1.2)°	423(10)
	0.124400	0.121740	0.121649	-6(1)°	378(28)
$24^3 \cdot 48$	**0.124400**	**0.121713**	**0.121677**	-17.8(7)°	405(8)
	0.124420	0.121713	0.121657	-16.7(7)°	387(8)
	0.124430	0.121760	0.121601	-4.8(7)°	377(8)
$48^3 \cdot 96$	**0.124508**	**0.121821**	**0.121466**	-3.5(4)°	284(4)
	0.124400	0.121713	0.121677	-18.5(9)°	389(5)

Table 3.1: Volumes, κ values and the fitted isospin mixing angles. There are four distinct ensembles with the sea-quark κ configurations indicated by bold text, and five additional partially-quenched calculations that have been performed on these ensembles with valence κ configurations listed in plain text. Physical electric charges were associated with the κ's for each flavour of quark (although the coupling is non-physical; see discussion in Section 3.2) and we also present the lightest neutral flavour-singlet meson $M_{u\bar{u}}$ on each ensemble for reference (calculated without disconnected contributions). The mixing angle result for the first listed ensemble follows theoretically from equations (3.9)–(3.11).

As we have detailed in Table 3.1, we have determined the mixing angles on both $24^3 \times 48$ and $48^3 \times 96$ volumes. We have found here that the mixing angles we calculate are consistent between the two lattice volumes, and hence we do not attempt to correct for finite volume effects in this work.

QCD-only mixing

We can see from Equation (3.27)–(3.29) in the absence of QED, $D_{\text{QED}} = D_{\text{QED}}^{\text{U-spin}} = 0$, that at first order in the quark masses, the mixing angles depend only on the mass splitting of the two relevant SU(2)-subgroup flavours relative to the third flavour's mass. For isospin,

$$\tan 2\theta_{\Sigma\Lambda,\text{isospin,QCD-only}} = \frac{\delta m_d - \delta m_u}{\sqrt{3}(\delta m_u + \delta m_d)} = \frac{\delta m_u - \delta m_d}{\sqrt{3}\,\delta m_s}, \tag{3.36}$$

provided that the average quark mass $\bar{m}$ is held constant. Because of this, we can present a QCD-only estimate of the mixing angle if we have a determination of the physical point quark masses. In a recent QCD-only lattice study of the Σ^0–Λ mixing [36], the quark masses at the physical point were determined to be

$$a\delta m_u = -0.01140(3), \quad a\delta m_d = -0.01067(3),$$

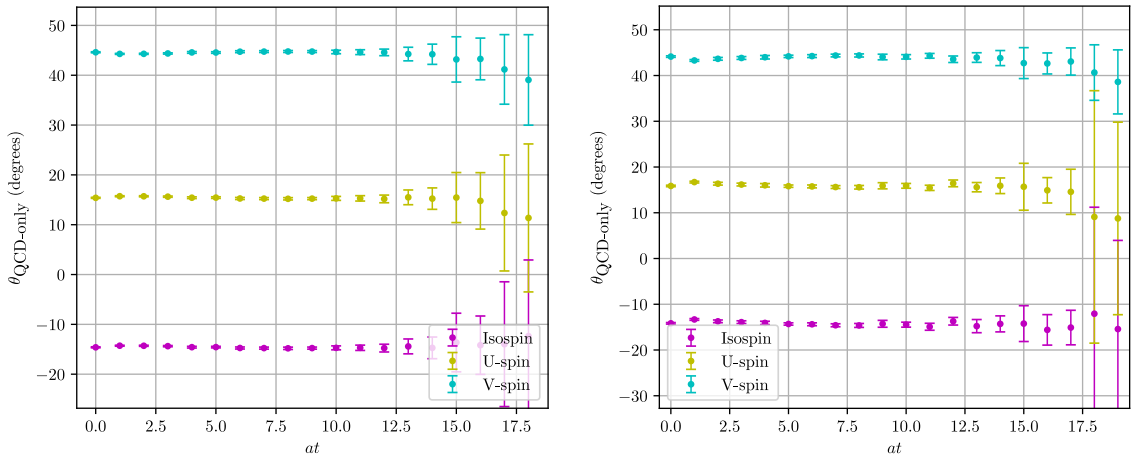

Figure 3.1: Mixing angles calculated on the two PQ calculations performed with the valence quark charges set to zero. The left plot has $(\kappa_u, \kappa_d, \kappa_s) = (0.12092, 0.1209, 0.12088)$ and the right plot has $(\kappa_u, \kappa_d, \kappa_s) = (0.12094, 0.1209, 0.12086)$. The QCD-only mixing angle formulae we have derived predict that the mixing angles be time-independent at first order.

which implies the isospin mixing angle

$$\Rightarrow \theta_{\Sigma\Lambda,\text{isospin,QCD-only}} = -0.55(3)^\circ.$$

Note that we have established a sign convention that follows from our choice of ordering for isospin, *uds* versus *dus*, as well as the ordering of the Σ^0 and Λ operators along the diagonal of the matrix of correlation functions. This convention differs from that used in [36]. We also note that using the mass ratios of the FLAG review [77], the QCD-only mixing angle is predicted to be $\theta_{\Sigma\Lambda,\text{isospin,QCD-only}} = -0.65(3)^\circ$.

We have performed two partially-quenched calculations with all valence quark charges set to zero, for the purpose of contrasting with the QCD+QED scenario. We can now check our earlier finding that the QCD-only mixing angle is time independent at first order, and we present the signals from both configurations in Figure 3.1 where this time independence is seen to be manifest. The valence κ values used in these calculations are $(\kappa_u, \kappa_d, \kappa_s) = (0.12092, 0.1209, 0.12088)$ for the left panel, and $(\kappa_u, \kappa_d, \kappa_s) = (0.12094, 0.1209, 0.12086)$ for the right panel.

QCD+QED mixing

As previously discussed in Section 3.1.2, we extract the mixing angles for each of our lattice setups detailed in Table 3.1 by studying the eigenvectors of the matrix of correlation functions, Equation (3.3). The mixing angles are determined on each timeslice, and at large Euclidean time where the Σ^0 and Λ are expected to dominate and render the eigenvectors time-independent, a constant function is fit to each angle.

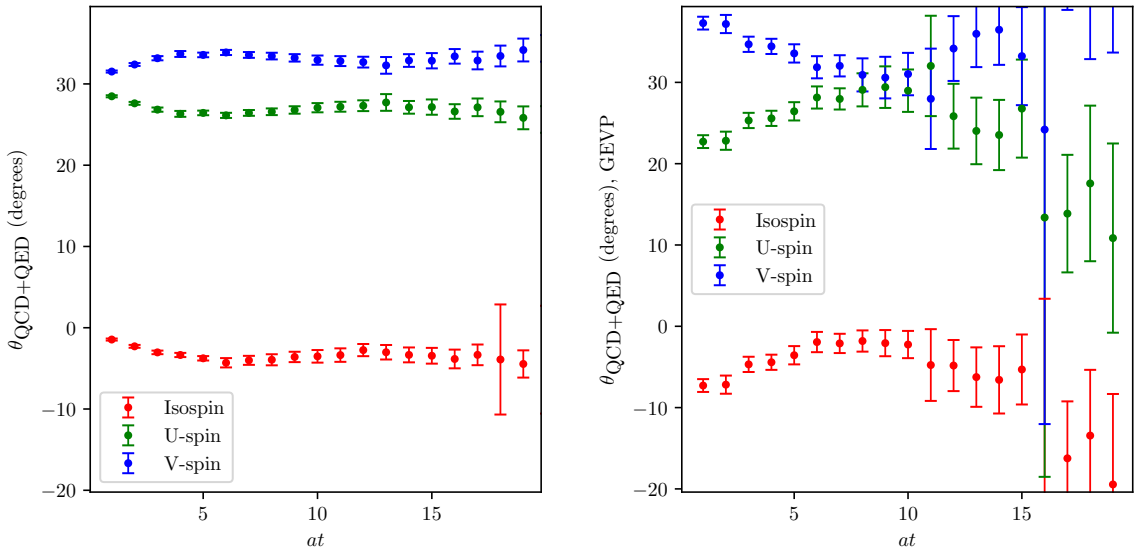

Figure 3.2: An example of the mixing angle signals (left), here calculated on our unitary $48^3 \times 96$ ensemble, and the same calculation performed using the GEVP (right).

Fit Parameters		
parameter	$D_{\text{QED}}/D_{\text{QCD}}$	Z
central value	$-3.8(7) \times 10^{-5}$	0.96(4)

Table 3.2: The best-fit parameter values ($\chi^2/\text{DOF} = 0.84$) from the fit of the QCD+QED isospin mixing angles with D_{QED} scaled to the physical EM coupling. The correlation coefficient for the two parameters is -0.45.

In Figure 3.2 we show an example of the mixing angle signal quality for each operator basis (left panel) on our unitary $48^3 \times 96$ simulation. In the right-hand panel we show the same mixing angles extracted from eigenvectors calculated using the GEVP, with $\delta t = 2$. Clearly there is agreement between the two methods, at least for a reasonable window in the GEVP case (say $at \in [6, 10]$), but we see increased stability for the EVP we use herein.

In Figure 3.3 we visualise the mixing angles from a selection of our ensembles exhibiting $\delta m_d = 0$, along with their corresponding fits, Equations (3.32)–(3.34). Included are the aforementioned PQ calculations with neutral valence quarks, which along this quark-mass trajectory are predicted to be constant from the QCD-only mixing formulae (Equation (3.36); similar for U and V). We see clear agreement between our fitted extrapolations and lattice data, indicating that our first order formulae are sufficient in this case. An interesting feature of this plot is the QCD+QED mixing angles asymptoting towards their respective QCD-only values as the up-quark mass deviates further from its SU(3)-symmetric value. This occurs because the symmetry breaking due to differences in the bare quark masses is dominating the effect of non-degenerate quark charges as we move away from $\delta m_u = 0$. An additional feature that can be seen in Figure 3.3 and from Equations (3.27)–

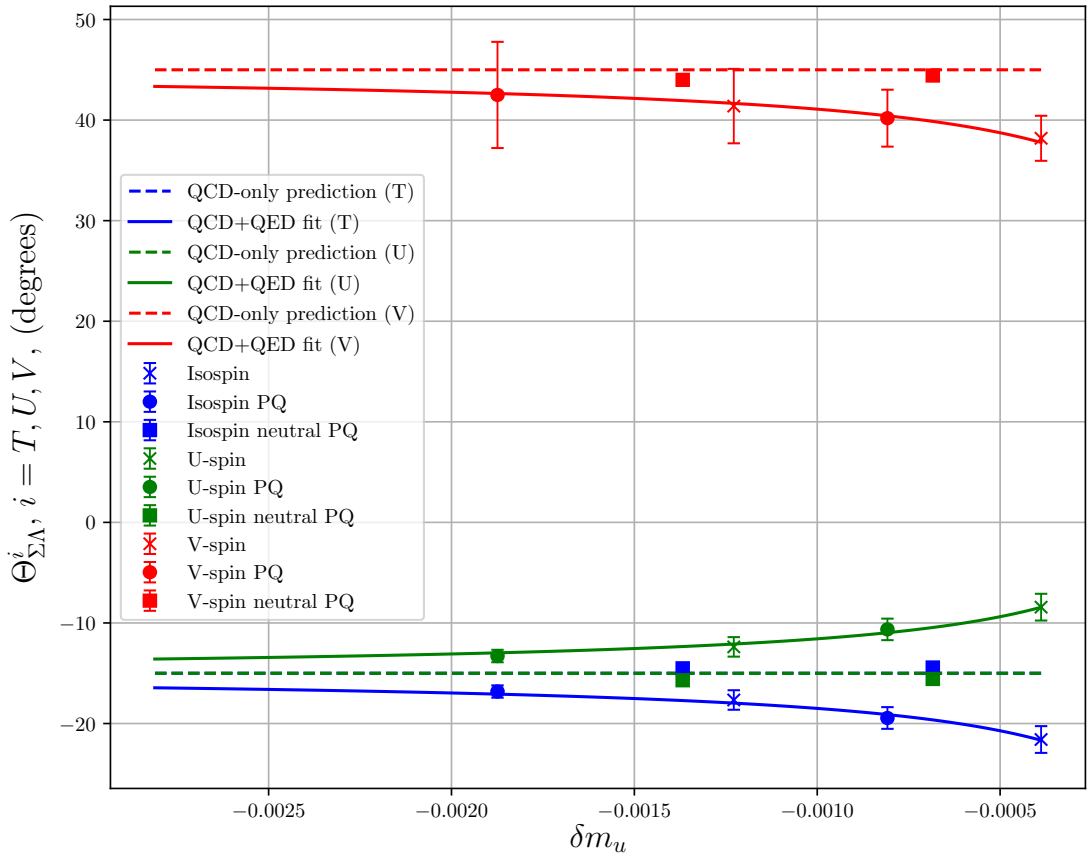

Figure 3.3: The mixing angles extracted from lattices with $\delta m_d = 0$ along with their respective fits. In this scenario the QCD-only mixing angle is a constant (dotted lines) and we can see the QED-inclusive mixing angles asymptoting to the QCD-only values as the T, U or V-spin symmetry becomes more broken by the mass parameters. Squares indicate mixing results from PQ calculations performed with all charges set to zero in order to approximate the QCD-only scenario, whilst the circles are PQ with physical charges (still unphysical coupling however) and the crosses are unitary.

(3.29) is that in the absence of QED ($D_{\mathrm{QED}} \to 0$), the differences between any two of the mixing angles is constant and has magnitude $\pi/3$ or $\pi/6$, whilst when QED is present only the isospin-V angle difference remains constant. This is because the isospin and V-spin pairs, u/d and u/s respectively, possess the same combinations of charges.

We now wish to extrapolate our isospin mixing angle to the physical point and present a preliminary result that can be compared with existing determinations. We consider this result preliminary as we have not attempted to gain full control of the systematic uncertainties present, such as finite volume effects and discretization errors. We use the physical-point quark mass parameters determined in [65],

$$a\delta m_u = -0.00834(8), \quad a\delta m_d = -0.00776(7),$$

and

$$a\delta m_u = -0.00791(4), \quad a\delta m_d = -0.00740(4),$$

using $32^3 \times 64$ and $48^3 \times 96$ volume lattices respectively. Unfortunately no $24^3 \times 48$ physical point is available, which would seem most consistent with our results, however our mixing angles agree between $24^3 \times 48$ and $48^3 \times 96$ volumes within uncertainties, and it is interesting to compare our results using these two determinations of the physical point masses. Using the best fit parameters displayed in Table 3.2 we find

$$\theta_{\Sigma\Lambda,\mathrm{isospin}}|_{\mathrm{QCD+QED}} = -1.00(32)^\circ,$$

and

$$\theta_{\Sigma\Lambda,\mathrm{isospin}}|_{\mathrm{QCD+QED}} = -0.96(31)^\circ,$$

for the physical quark masses determined on $32^3 \times 64$ and $48^3 \times 96$ volumes respectively. Note that the parameter D_{QED} has been scaled down by the proportionality factor $\alpha^\star_{\mathrm{QED}}/\alpha_{\mathrm{QED}} \approx 0.07338$ that relates our simulated EM coupling α_{QED} to that of the real world, $\alpha^\star_{\mathrm{QED}}$. These first-order results compare favourably with the widely used DvH formula result [34, 70] of $-0.86(6)^\circ$, which also incorporates QED effects implicitly, in the sense that it cannot separate QCD from QED effects on the mixing angle.

Note that while a direct confirmation of the assumed linear-in-α_{QED} scaling of the QED parameter has not yet been performed, it was shown in [50] that the quantities $1/\kappa_q^c$, $1/\bar{\kappa}_q$ and the bare quark mass at the symmetric point, $1/2\bar{\kappa}_q - 1/2\kappa_q^c$, all displayed clear linear behaviour with scaling of the quark charge squared.

We note that our renormalisation parameter Z is consistent with that presented in [65] of 0.93 using the Dashen scheme, which is defined by the bare quark-mass dependence of connected-only, neutral pseudoscalar meson masses. As was found in [36], the magnitude of the next-to-leading order QCD term was roughly one third that of the leading-order QCD term, and hence we approximate the contributions from higher order QCD terms as a systematic uncertainty of 20%. The effects of higher-order QED terms remains to be investigated.

Finally, as a further visualisation aid we present a surface plot of the isospin mixing angle fit to all ensembles of Table 3.1, along with the mixing angles themselves (sans uncertainties; black circles), in Figure 3.4. The four bottom-left-most points are the same data, sharing the $\delta m_d = 0$ trajectory, that were presented in Figure 3.3. Also included for reference is the location of the physical point, giving us a sense of the spread of our ensembles in quark mass space. Note that this surface indicates the fit before adjusting for the un-physically large EM coupling.

3.3 Summary

In this exploratory work we have detailed a program for calculating the Σ^0–Λ mixing in lattice QCD+QED, through which initial results were obtained which agree with existing determinations and that suggest the QED contribution to the mixing could be 30–50% of the total mixing. The ideas presented in this chapter will also be foundational to the work of Chapter 5, where we will investigate mixing in the flavour-neutral pseudoscalar mesons: π^0, η and η'.

Perhaps the primary difference between this work and similar lattice studies such as [36], is the emphasis on the calculation and extrapolation of the eigenvectors of the matrix of correlation functions, as opposed to the typical procedure of calculating hadron masses and operator overlaps. The results herein suggest this to be an effective technique, and with a greater number of ensembles at more varied quark masses, as well as a proper treatment of the finite-volume and discretization errors, one which will produce a precision determination of the Σ^0–Λ mixing angle.

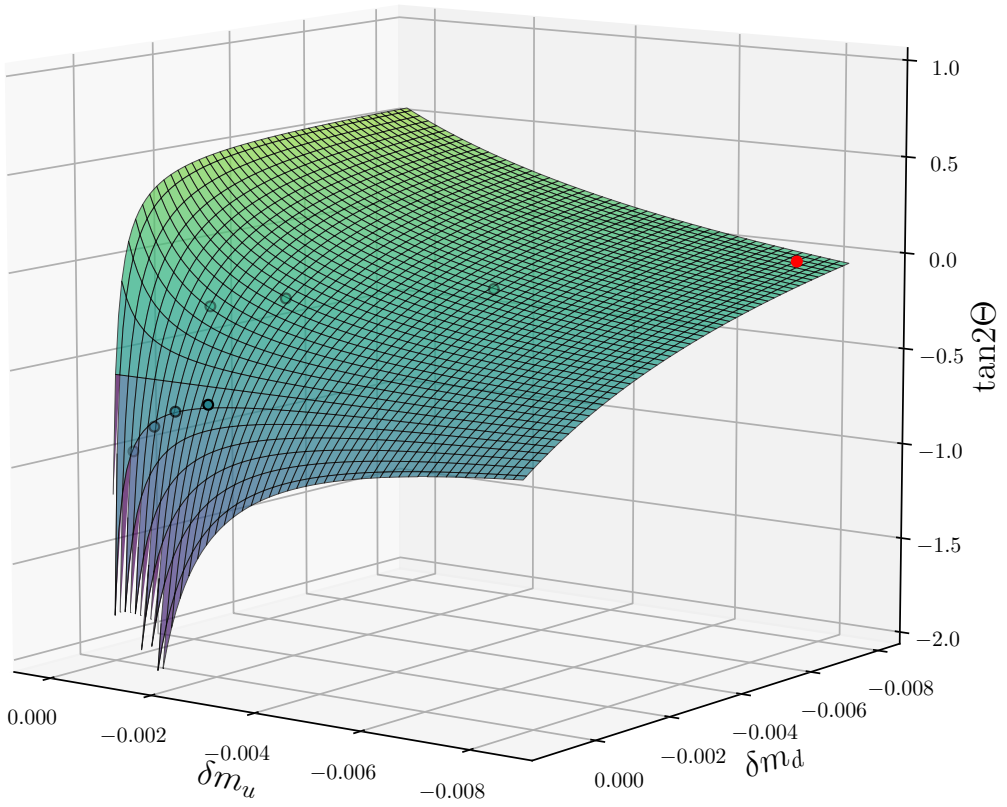

Figure 3.4: A visualisation of the T-spin mixing angle extrapolation Equation (3.32) from a fit to all extracted mixing angles (black circles), and the physical point location (red circle).

Chapter 4

Propagators from stochastic sources

In Chapter 5 we investigate the low-lying unflavoured pseudoscalar mesons, accessible in lattice QCD through correlation functions composed with flavour-neutral quark operators. The Wick contractions for specific correlation functions will be given in detail therein but we note that, in general, flavour-neutral operators such as $\bar{q}_f \Gamma q_f$, for some quark flavour f and Dirac structure Γ, will lead to *disconnected* or *quark-loop* terms, mathematically manifesting as quark propagators which terminate at their own source location: $S(x;x)$.

The point-to-all propagators $S(x;x_0)$ which we have utilised thus far, exploiting translational invariance of the source, contain information about propagation from the single source location x_0 to every other lattice site, including x_0 itself: $S(x_0;x_0)$. One could therefore imagine calculating the point-to-all propagator for every source site x_i on the lattice, and constructing the full self-to-self propagator $S(x;x)$ from the point-to-point pieces $S(x_i;x_i)$. In practice however, this naive construction is completely unattainable on typical lattice volumes due to the computational expense of inverting the fermion matrix a total $12 \cdot V_4$ times, where V_4 is the number of spacetime sites on the lattice.

In this chapter we introduce a method for approximating the all-to-all propagator, $S(y;x)$, of which the self-to-self propagator is a part, using stochastically-generated sources. A volume source, in contrast to the standard point source, has non-zero elements on each site of the lattice, and we will see that a particular choice for these elements results in a key property which facilitates the all-to-all propagator. After first establishing the base method we discuss various methods for improving precision. Central to this topic is balancing the computational cost of the approximation with improvement of the desired signal. The numerical calculations for this chapter were performed on a dynamical $n_f = 1+1+1$, $16^3 \times 32$, QCD-only lattice with $\beta_{\mathrm{QCD}} = 5.5$, and $(\kappa_u, \kappa_d, \kappa_s) = (0.120850, 0.120800, 0.120750)$. The discretised QCD action used here is the same as for the QCD+QED simulations performed elsewhere in this thesis, and was detailed in Chapter 2.

For completeness we note that another method used in the calculation of disconnected diagrams which has found broad success, but which we do not investigate further herein, is known as *distillation* and was first introduced in [78]. In this

method 'distilled' operators are defined using a truncated eigenmode representation of the quark-smearing operator, through which a reduced-rank quark propagator is defined which may be calculated exactly.

4.1 $\mathbb{Z}_2$ noise sources

A common choice in the construction of stochastic sources, especially for two-point correlation functions, is to sample the set $\{-1, 1\}$, a representation of the cyclic group $\mathbb{Z}_2$, with equal probability. The desirable quality of sources generated in this way is that if we employ an ensemble of N_r stochastically generated $\mathbb{Z}_2$ volume sources, $\eta_{[r]}(x)^a_\alpha \in \{-1, 1\}$, for spacetime lattice site x, colour index a and Dirac index α, they exhibit the key property

$$\lim_{N_r\to\infty} \frac{1}{N_r} \sum_{r=1}^{N_r} \eta_{[r]}(x)^a_\alpha \, \eta_{[r]}(y)^{b\dagger}_\beta = \delta_{ab}\delta_{\alpha\beta}\delta_{xy}. \tag{4.1}$$

By inverting the fermion matrix (we neglect reference to specific quark flavours here) against the volume source,

$$\psi_{[r]}(y)^a_\alpha = \sum_z M^{-1}(y;z)^{ac}_{\alpha\rho} \, \eta_{[r]}(z)^c_\rho, \tag{4.2}$$

we obtain the solution vector, $\psi_{[r]}(y)^a_\alpha$, which leads to the all-to-all propagator through the noise source average

$$\begin{aligned}
\lim_{N_r\to\infty} \frac{1}{N_r} \sum_{r=1}^{N_r} \psi_{[r]}(y)^a_\alpha \, \eta_{[r]}(x)^{b\dagger}_\beta &= \lim_{N_r\to\infty} \frac{1}{N_r} \sum_{r=1}^{N_r} \sum_z M^{-1}(y;z)^{ac}_{\alpha\rho} \, \eta_{[r]}(z)^c_\rho \, \eta_{[r]}(x)^{b\dagger}_\beta \\
&= \sum_z M^{-1}(y;z)^{ac}_{\alpha\rho} \, \delta_{cb}\delta_{\rho\beta}\delta_{zx} = M^{-1}(y;x)^{ab}_{\alpha\beta}, \\
\therefore S(y;x)^{ab}_{\alpha\beta} &= \lim_{N_r\to\infty} \frac{1}{N_r} \sum_{r}^{N_r} \psi_{[r]}(y)^a_\alpha \, \eta_{[r]}(x)^{b\dagger}_\beta .
\end{aligned} \tag{4.3}$$

In practice, a finite N_r is chosen such that the introduced stochastic noise is acceptable in the context of the desired signal, or ideally, is dominated by the uncertainty in the gauge-field average. There are numerous other distributions which could be sampled such that the resulting sources exhibit the property of Equation (4.1), some possessing other qualities which may make them more appropriate for other applications [79, 80], however for our purposes $\mathbb{Z}_2$ is sufficient and produces the greatest noise reduction, with the introduced noise going like $1/\sqrt{N_r}$ [81–84].

4.2 Noise source dilution

A simple method for improving the noise source calculation of quark propagators is known as dilution [82, 85], where one separates each volume source $\eta_{[r]}$ into N_d diluted sources $\eta^d_{[r]}$ which sum to give the original source: $\eta_{[r]} = \sum_d^{N_d} \eta^d_{[r]}$.

Typically, dilution is chosen to coincide with one or a number of the noise source indices, and we have chosen a baseline of dilution in colour, spin and time indices such that we may write our noise sources as

$$\eta_{[r]}(\vec{x}, t; t_0)^{b\,b_0}_{\beta\,\beta_0} = \xi_{[r]}(\vec{x})\,\delta^{b\,b_0}\,\delta_{\beta\,\beta_0}\,\delta_{t\,t_0}, \tag{4.4}$$

where b_0, β_0 and t_0 label the colour, spin and time sites on the lattice where the diluted source is non-zero, and $\xi_{[r]}(\vec{x})$ is a spatial $\mathbb{Z}_2$ source exhibiting an analogue of the key property of Equation (4.1),

$$\lim_{N_r\to\infty} \frac{1}{N_r} \sum_{r=1}^{N_r} \xi_{[r]}(\vec{x})\,\xi_{[r]}(\vec{y}) = \delta_{\vec{x}\vec{y}}. \tag{4.5}$$

In order to approximate the all-to-all propagator using our diluted sources we must calculate the solution vectors as in Equation (4.2), inverting against each diluted source

$$\psi_{[r]}(y; t_0)^{ab}_{\alpha\beta} = \sum_{\vec{z},t} M^{-1}(y; \vec{z}, t)^{ac}_{\alpha\rho}\,\eta_{[r]}(\vec{z}, t; t_0)^{cb}_{\rho\beta} = \sum_{\vec{z}} M^{-1}(y; \vec{z}, t_0)^{ab}_{\alpha\beta}\,\xi_{[r]}(\vec{z}), \tag{4.6}$$

from which individual contributions to the propagator are computed as

$$S(y; \vec{x}, t_0)^{ab}_{\alpha\beta}\,\delta_{t\,t_0}\,\delta^{c\,b}\,\delta_{\rho\,\beta} = \lim_{N_r\to\infty} \frac{1}{N_r} \sum_{r=1}^{N_r} \psi_{[r]}(y; t_0)^{ab}_{\alpha\beta}\,\eta_{[r]}(\vec{x}, t; t_0)^{cb}_{\rho\beta}. \tag{4.7}$$

This calculation must be repeated for each combination of t_0, b and β, after which the contributions may be summed. Notice that each contribution to the propagator is constructed using only one of the diluted sources, i.e. on the right-hand side of Equation (4.7) the dilution indices on the solution vector and noise source are identical.

Clearly, introducing dilution increases the number of computationally expensive inversions of the fermion matrix by a factor N_d, and were we to additionally dilute our sources completely in the spatial dimensions of the lattice we would simply recover the naive calculation of the all-to-all propagator. Moreover, full time-dilution facilitates approximation of the all-to-all propagator with just a single noise source, $N_r = 1$, and it has been show that a single time-diluted source far outperforms an ensemble of $N_r = N_t$ un-diluted sources for pseudoscalar two-point functions [82].

In Figure 4.1 we present a comparison of the effective mass of the η' meson calculated using 1–5 independent noise sources on each gauge configuration. Each

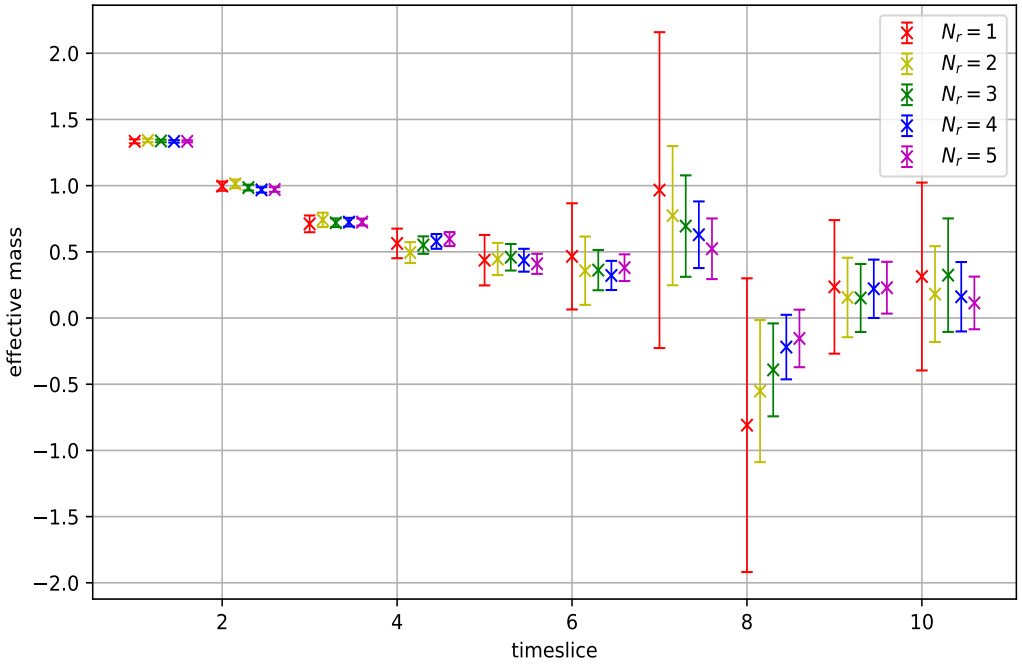

Figure 4.1: A comparison of the effective masses of the diagonalized η' state for increasing numbers of noise sources on our $16^3 \times 32$ simulation. Each signal is produced from ≈ 300 gauge configurations with the indicated number of noise sources (diluted in spin, colour and time) used on each configuration.

noise source is diluted in spin, colour and time. The effective mass signals for varying N_r agree and we can see the expected $1/\sqrt{N_r}$ noise reduction.

4.2.1 Spatial interlacing

Interlacing is an approach to dilution where one separates the spatial noise source into a number of diluted components determined by some interlacing 'mask' or elected pattern.

In general, the spatial lattice is separated into disjoint sets X_i which return the full spatial lattice in their union. If we make the spin, colour, time and interlacing dilution explicit, we can write our noise sources as

$$\eta^i_{[r]}(\vec{x}, t; t_0)^{b\,b_0}_{\beta\,\beta_0} = \xi_{[r]}(\vec{x})\,\delta^{b\,b_0}\,\delta_{\beta\,\beta_0}\,\delta_{t\,t_0}\,\delta_{\vec{x}\in X_i}, \tag{4.8}$$

where the superscript i is the interlacing index and $\delta_{\vec{x}\in X_i} = 1$ if $\vec{x} \in X_i$ and is zero otherwise. The solution vector for a particular choice of t_0, b, β and i is then calculated as

$$\psi^i_{[r]}(y; t_0)^{ab}_{\alpha\beta} = \sum_{\vec{z}} \sum_{t'} M^{-1}(y; \vec{z}, t')^{ac}_{\alpha\rho}\, \eta^i_{[r]}(\vec{z}, t'; t_0)^{cb}_{\rho\beta} = \sum_{\vec{z}\in X_i} M^{-1}(y; \vec{z}, t_0)^{ab}_{\alpha\beta}\, \xi_{[r]}(\vec{z}), \tag{4.9}$$

where we have labelled our solution vector in the same way as our diluted source to indicate which inversion it was calculated from. We obtain contributions to the full propagator as

$$\lim_{N_r\to\infty}\frac{1}{N_r}\sum_{r=1}^{N_r}\psi^i_{[r]}(y;t_0)^{ab}_{\alpha\beta}\,\eta^i_{[r]}(\vec{x},t;t_0)^{cb}_{\rho\beta}$$

$$=\lim_{N_r\to\infty}\frac{1}{N_r}\sum_{r=1}^{N_r}\sum_{\vec{z}\in X_i}M^{-1}(y;\vec{z},t_0)^{ab}_{\alpha\beta}\,\xi_{[r]}(\vec{z})\,\eta^i_{[r]}(\vec{x},t;t_0)^{cb}_{\rho\beta}$$

$$=\sum_{\vec{z}\in X_i}M^{-1}(y;\vec{z},t_0)^{ab}_{\alpha\beta}\,\delta_{t\,t_0}\,\delta^{c\,b}\,\delta_{\rho\,\beta}\,\delta_{\vec{x}\in X_i}\lim_{N_r\to\infty}\frac{1}{N_r}\sum_{r=1}^{N_r}\xi_{[r]}(\vec{z})\,\xi_{[r]}(\vec{x})$$

$$=M^{-1}(y;\vec{x},t_0)^{ab}_{\alpha\beta}\,\delta_{t\,t_0}\,\delta^{c\,b}\,\delta_{\rho\,\beta}\,\delta_{\vec{x}\in X_i}, \tag{4.10}$$

and as before we recover the full propagator by summing the contributions from each diluted source:

$$S(y;x)^{ac}_{\alpha\rho}=\sum_b\sum_\beta\sum_{t_0}\sum_i\lim_{N_r\to\infty}\frac{1}{N_r}\sum_{r=1}^{N_r}\psi^i_{[r]}(y;t_0)^{ab}_{\alpha\beta}\,\eta^i_{[r]}(\vec{x},t;t_0)^{cb}_{\rho\beta}. \tag{4.11}$$

In this work we have investigated improvement through the use of an interlacing mask that divides the spatial lattice into 2^3 cubes, with only the central site of each cube being non-zero for any single source vector, as visualised in Figure 4.2. This mask can be shifted on the spatial lattice for a total of 8 orthogonal source vectors, therefore inducing an additional $8\times$ the computational cost of calculating a complete quark propagator. We note that this is an example of hierarchical probing with a fixed distance, as introduced in [86, 87].

A physical motivation for this type of interlacing is the removal of nearest-neighbour correlations from each non-zero element of the source vector, and since short-distance correlations correspond to high energies, this may be advantageous for studying low-lying states on the lattice as we are herein.

Unfortunately, in tuning the noise reduction on our small lattice volumes we did not see a significant enough improvement from 2^3 interlacing to justify the $8\times$ increase in computational cost when compared with simply increasing N_r.

4.3 Smearing noise propagators

Gauge-covariant Gaussian sink smearing can be performed on propagators calculated using noise sources in the usual fashion [88]. There is a nuance in the treatment of source smearing however, in that the smearing can be applied to the source that is used in constructing the propagator *after* the inversion has been performed. This is fortunate since we can access any number of different source smearing levels without incurring the cost of an additional inversion of the fermion matrix each time. Ad-

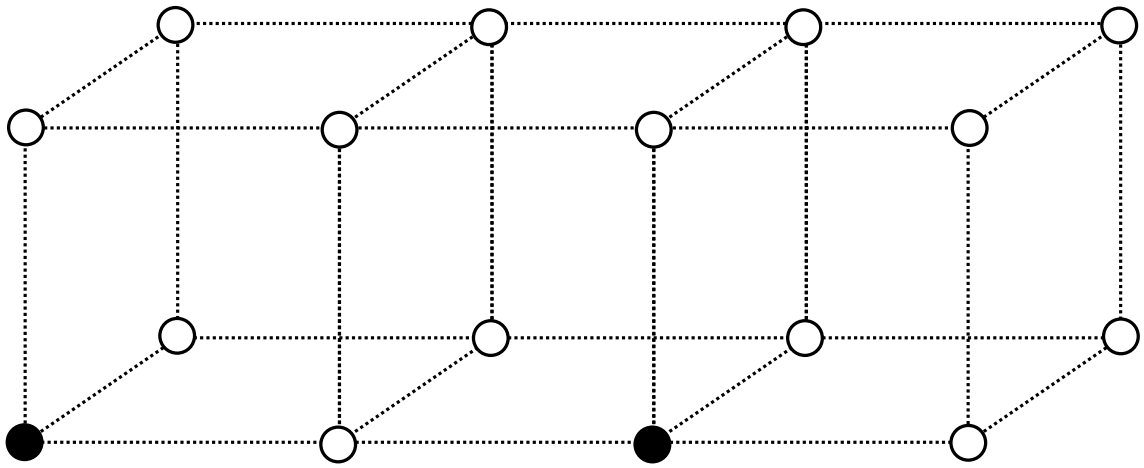

Figure 4.2: A visualisation of a section of the 2^3 interlacing mask, where the filled black lattice sites indicate those left non-zero by the mask. This mask is shifted to dilute the spatial source vector into a total of 8 orthogonal components.

ditionally, we expect smearing to be useful in this work as disconnected correlation functions, calculated using stochastic sources or otherwise, tend to become noisy at small Euclidean time separations, and smearing of purely-connected correlation functions is known to help in isolating the relevant ground states at earlier times.

The $(l+1)^{\text{th}}$ sweep of gauge-covariant Gaussian smearing on the solution vector $\psi_{[r]}(y)^a_\alpha$ is implemented as

$$\psi^{(l+1)}_{[r]}(y)^a_\alpha = (1-\alpha)\psi^{(l)}_{[r]}(y)^a_\alpha + \frac{\alpha}{6}\sum_{\beta=1}^{3} U_\beta(y)^{ab}\psi^{(l)}_{[r]}(y+a\hat{\beta})^b_\alpha + U^\dagger_\beta(y-a\hat{\beta})^{ab}\psi^{(l)}_{[r]}(y-a\hat{\beta})^b_\alpha, \tag{4.12}$$

where the parameter α dictates the 'strength' of the smearing (we use $\alpha = 0.7$ herein). Smearing of the source vector $\eta_{[r]}$ is carried out in the same way.

Where the solution vector is calculated as in Equation (4.2), the quark propagator with l sweeps of sink smearing and m sweeps of source smearing is simply constructed as

$$S^{(l,m)}(y,x) = \lim_{N_r\to\infty}\frac{1}{N_r}\sum_{r}^{N_r}\psi^{(l)}_{[r]}(y)\otimes\eta^{(m)}_{[r]}(x)^\dagger. \tag{4.13}$$

Note that if the standard colour dilution is used for the source vector, the result of source smearing is that the smeared noise source will no longer exhibit the Kronecker delta property in colour.

Figure 4.3 shows the effect of source and sink smearing on the diagonalized π^0, η and η' effective masses for varying numbers of smearing sweeps (π^0 and η appear degenerate). Whilst we are not necessarily resolving reliable plateaus in this case, we do see the effect in the flattening of the signals at earlier Euclidean time separations for increasing levels of smearing, and no indication that these levels of smearing are introducing a systematic degradation of the signals.

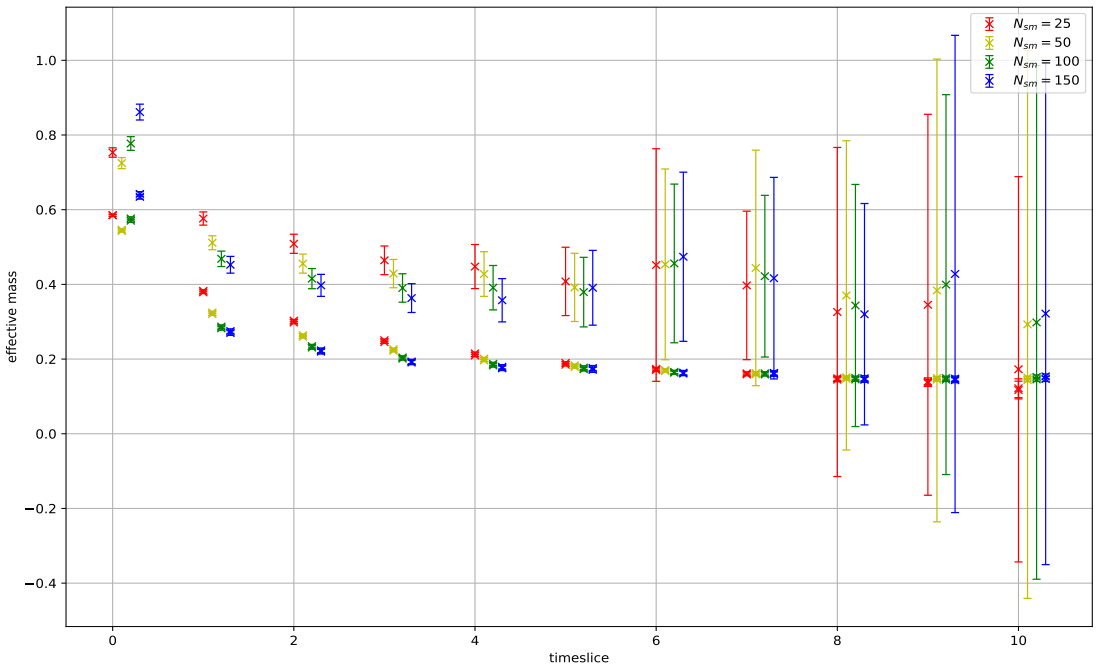

Figure 4.3: A comparison of the effective masses of the diagonalized neutral PS meson states (the lightest 2 states appear visually degenerate), for increasing levels of source and sink smearing at the approximate SU(3) flavour symmetric point. Each signal is produced from ≈100 gauge configurations with 3 noise sources on each, and equal levels of smearing at the source and sink for $N_{sm} = 25, 50, 100, 150$ sweeps of smearing.

4.4 The one-end trick

The stochastic-source methods which we have discussed so far can in principle be applied to approximate the complete all-to-all quark propagator without the extremely prohibitive computational cost of $12 \cdot V_4$ inversions of the fermion matrix. This is particularly useful for calculating the 'spacetime-diagonal' part of the quark propagator $S(x;x)$, that is required in correlation functions of closed quark loops, since this propagator only contains $12^2 \cdot V_4$ numbers and can realistically be stored in computer memory. However the full all-to-all propagator, although now being computationally accessible, contains $12^2 \cdot (V_4)^2$ numbers and cannot feasibly be stored for use in correlation function calculations, since if we take just a small $16^3 \times 32$ lattice as an example, a single-precision all-to-all propagator would require ≈ 10 terabytes of memory.

One way to calculate connected correlation functions with stochastic methods while avoiding explicit use of the all-to-all propagator, but receiving some of its statistical advantage, is the one-end trick [89, 90]. To implement the one-end trick for two-point connected correlators, we simply use our (diluted) solution vectors in place of the full stochastic propagator before carrying out the noise ensemble average:

$$C_{2pt}(t;t_0) = \left\langle \lim_{N_r\to\infty} \frac{1}{N_r} \sum_{r}^{N_r} \sum_{\vec{y}} \psi_{[r]}(y;t_0)^{ab}_{\alpha\kappa}\, \Gamma_{\kappa\beta}\, \psi_{[r]}(y;t_0)^{ba}_{\beta\beta}\, \Gamma_{\beta\alpha}\, e^{-i\vec{p}\cdot\vec{y}} \right\rangle, \qquad (4.14)$$

for $y = (\vec{y}, t)$, some 3-momentum $\vec{p}$ and Dirac structure Γ. The angled brackets $\langle \dots \rangle$ indicate the gauge ensemble average explicitly.

Specialising now, without loss of generality, to $\vec{p} = \vec{0}$ and $\Gamma = \mathbb{I}$ to demonstrate the one-end trick, we calculate

$$\begin{aligned} C_{2pt}(t;t_0) &= \left\langle \lim_{N_r\to\infty} \frac{1}{N_r} \sum_{r}^{N_r} \sum_{\vec{y}} \psi_{[r]}(y;t_0)^{ab}_{\alpha\beta}\, \psi_{[r]}(y;t_0)^{ba}_{\beta\alpha} \right\rangle \\ &= \left\langle \lim_{N_r\to\infty} \frac{1}{N_r} \sum_{r}^{N_r} \sum_{\vec{y}} \sum_{\vec{x},\vec{z}} M^{-1}(y;\vec{x},t_0)^{ab}_{\alpha\beta}\, \xi_{[r]}(\vec{x})\, M^{-1}(y;\vec{z},t_0)^{ba}_{\beta\alpha}\, \xi_{[r]}(\vec{z}) \right\rangle \\ &= \left\langle \sum_{\vec{y}} \sum_{\vec{x},\vec{z}} M^{-1}(y;\vec{x},t_0)^{ab}_{\alpha\beta}\, M^{-1}(y;\vec{z},t_0)^{ba}_{\beta\alpha} \lim_{N_r\to\infty} \frac{1}{N_r} \sum_{r}^{N_r} \xi_{[r]}(\vec{x})\, \xi_{[r]}(\vec{z}) \right\rangle \\ &= \left\langle \sum_{\vec{x},\vec{y}} M^{-1}(y;\vec{x},t_0)^{ab}_{\alpha\beta}\, M^{-1}(y;\vec{x},t_0)^{ba}_{\beta\alpha} \right\rangle. \end{aligned} \qquad (4.15)$$

The end result above is the desired two-point correlation function with, at least in the limit of infinitely many stochastic sources, an additional sum over source locations $\vec{x}$ which didn't explicitly appear in the original construction.

4.5 The hybrid method

The last method of improvement which we have investigated, although ultimately not utilised in our results, is the hybrid method as introduced in [82] and used in various subsequent calculations [91–93]. The method is based on the eigendecomposition of the Hermitian matrix $Q = \gamma^5 M$, where M is the lattice fermion matrix. If we let $v^{[i]}(x)^a_\alpha$ denote the i$^{\text{th}}$ eigenvector of the matrix $Q(y;x)^{ab}_{\alpha\beta}$, with eigenvectors ordered according to their ascending eigenvalues λ_i, then the exact all-to-all lattice propagator may be written as

$$M^{-1}(y;x)^{ab}_{\alpha\beta} = \sum_{i=1}^{N} \frac{1}{\lambda_i} v^{[i]}(y)^a_\alpha \, v^{[i]}(x)^{b\dagger}_\rho \, \gamma^5_{\rho\beta}, \tag{4.16}$$

noting that N is the rank of the fermion matrix. Calculating the propagator in this way is clearly infeasible, however truncating the sum at some $N_{\text{ev}} \ll N$ may provide a suitable approximation of the quark propagator, as there is evidence that the low modes should contain most of the low-energy physical information [94]. In the hybrid method one calculates the aforementioned truncated eigendecomposition and uses stochastic sources to approximate the remaining unknown high modes.

The purely high-mode portion of the propagator,

$$S(y;x)_{\text{high}} = \sum_{i=N_{\text{ev}}+1}^{N} \frac{1}{\lambda_i} v^{[i]}(y) \otimes v^{[i]}(x)^\dagger \, \gamma^5, \tag{4.17}$$

can be calculated using stochastic source techniques through application of the projection operator

$$\mathcal{P}_1 = 1 - \mathcal{P}_0 = 1 - \sum_{i=1}^{N_{\text{ev}}} v^{[i]} \otimes v^{[i]\dagger}, \tag{4.18}$$

to the standard $\mathbb{Z}_2$ noise sources, with any elected dilution, prior to solving for the solution vector through inversion of the matrix Q:

$$\psi^{\text{high}}_{[r]}(y)^a_\alpha = \sum_z Q^{-1}(y;z)^{ab}_{\alpha\rho} \, (\mathcal{P}_1 \, \eta_{[r]})(z)^b_\rho. \tag{4.19}$$

Using the above solution vector we simply construct our high-mode propagator in the usual way

$$\lim_{N_r\to\infty} \frac{1}{N_r} \sum_{r=1}^{N_r} \psi^{\text{high}}_{[r]}(y)^a_\alpha \, \eta_{[r]}(x)^{b\dagger}_\beta = \lim_{N_r\to\infty} \frac{1}{N_r} \sum_{r=1}^{N_r} \sum_{z,w} Q^{-1}(y;z)^{ac}_{\alpha\rho} \, \mathcal{P}_1(z;w)^{cd}_{\rho\sigma} \, \eta_{[r]}(w)^d_\sigma \, \eta_{[r]}(x)^{b\dagger}_\beta$$

$$= \sum_{z,w} Q^{-1}(y;z)^{ac}_{\alpha\rho} \left(\delta_{zw}\delta_{cd}\delta_{\rho\sigma} - \sum_{j=1}^{N_{\text{ev}}} v^{[j]}(z)^c_\rho \, v^{[j]}(w)^{d\dagger}_\sigma \right) \delta_{wx}\delta_{db}\delta_{\sigma\beta}$$

$$= \sum_z \sum_{i=1}^{N} \frac{1}{\lambda_i} v^{[i]}(y)^a_\alpha \, v^{[i]}(z)^{c\dagger}_\rho \left(\delta_{zx}\delta_{cb}\delta_{\rho\beta} - \sum_{j=1}^{N_{\text{ev}}} v^{[j]}(z)^c_\rho \, v^{[j]}(x)^{b\dagger}_\beta \right)$$

$$= \sum_{i=1}^{N} \frac{1}{\lambda_i} v^{[i]}(y)^a_\alpha \, v^{[i]}(x)^{b\dagger}_\beta - \sum_{i=1}^{N} \sum_{j=1}^{N_{\text{ev}}} \sum_z \frac{1}{\lambda_i} v^{[i]}(y)^a_\alpha \, v^{[i]}(z)^{c\dagger}_\rho \, v^{[j]}(z)^c_\rho \, v^{[j]}(x)^{b\dagger}_\beta$$

$$= \sum_{i=1}^{N} \frac{1}{\lambda_i} v^{[i]}(y)^a_\alpha \, v^{[i]}(x)^{b\dagger}_\beta - \sum_{i=1}^{N_{\text{ev}}} \frac{1}{\lambda_i} v^{[i]}(y)^a_\alpha \, v^{[i]}(x)^{b\dagger}_\beta, \tag{4.20}$$

which clearly evaluates to Eq. (4.17). We have assumed in the above calculation that the eigenvectors are normalised such that $\sum_z v^{[i]}(z)^{c\dagger}_\rho \, v^{[j]}(z)^c_\rho = \delta_{ij}$.

In conclusion, we can estimate the all-to-all propagator as

$$S(y;x) \approx \sum_{i=1}^{N_{\text{ev}}} \frac{1}{\lambda_i} v^{[i]}(y) \otimes v^{[i]}(x)^\dagger \, \gamma^5 + \frac{1}{N_r} \sum_{r=1}^{N_r} \psi^{\text{high}}_{[r]}(y) \otimes \eta_{[r]}(x)^\dagger \, \gamma^5, \tag{4.21}$$

for some N_{ev} and N_r as large as is computationally achievable, and $\psi^{\text{high}}_{[r]}$ satisfying Equation (4.19).

It is straightforward to show that one can also approximate the high-mode part of the all-to-all propagator as

$$S(y;x)_{\text{high}} \approx \frac{1}{N_r} \sum_{r=1}^{N_r} \psi^{\text{high}}_{[r]}(y) \otimes (\mathcal{P}_1 \, \eta_{[r]})(x)^\dagger \, \gamma^5, \tag{4.22}$$

which could be easier to implement in practice since the noise source for inversion and construction of the propagator are the same.

4.5.1 The hybrid one-end-trick

In order to utilise the one-end trick in the context of the hybrid method, some consideration must be given to the inclusion of the low modes which were absent from our previous discussion of the one-end trick.

We can confirm the quantity required for calculating connected correlation functions using the hybrid one-end trick by substituting the inverse fermion matrix eigendecomposition into the right-hand side of Equation (4.2), taking explicit spin, colour and time dilution,

$$\sum_{\vec{x}} M^{-1}(y;\vec{x},t_0)^{ab}_{\alpha\beta} \, \xi_{[r]}(\vec{x}) = \sum_{\vec{x}} \sum_{i=1}^{N} \frac{1}{\lambda_i} v^{[i]}(y)^a_\alpha \, v^{[i]}(\vec{x},t_0)^{b\dagger}_\rho \, \gamma^5_{\rho\beta} \, \xi_{[r]}(\vec{x})$$

$$= \sum_{\vec{x}} \left(\sum_{i=1}^{N_{\text{ev}}} \frac{1}{\lambda_i} v^{[i]}(y)^a_\alpha \, v^{[i]}(\vec{x},t_0)^{b\dagger}_\rho \, \gamma^5_{\rho\beta} \, \xi_{[r]}(\vec{x}) + \sum_{i=N_{\text{ev}}+1}^{N} \frac{1}{\lambda_i} v^{[i]}(y)^a_\alpha \, v^{[i]}(\vec{x},t_0)^{b\dagger}_\rho \, \gamma^5_{\rho\beta} \, \xi_{[r]}(\vec{x}) \right).$$

The first term in the above sum is unfamiliar from our previous one-end trick discussion, and is evidently the low-mode component of the full solution vector. The second term contains the corresponding high modes and we can eliminate them in favour of our stochastic construction (RHS of Equation (4.20))

$$\sum_{\vec{x}} \sum_{i=N_{\rm ev}+1}^{N} \frac{1}{\lambda_i} v^{[i]}(y)^a_\alpha \, v^{[i]}(\vec{x},t_0)^{b\dagger}_\rho \, \gamma^5_{\rho\beta} \, \xi_{[r]}(\vec{x})$$

$$= \sum_{\vec{x},\vec{w},\vec{z}} \lim_{N_r\to\infty} \frac{1}{N_r} \sum_{r'=1}^{N_r} Q^{-1}(y;\vec{z},t_0)^{ac}_{\alpha\kappa} \, \mathcal{P}_1(\vec{z},t_0;\vec{w},t_0)^{cb}_{\kappa\rho} \, \xi_{[r']}(\vec{w}) \, \xi_{[r']}(\vec{x})^\dagger \, \gamma^5_{\rho\beta} \, \xi_{[r]}(\vec{x})$$

$$= \sum_{\vec{x},\vec{z}} Q^{-1}(y;\vec{z},t_0)^{ac}_{\alpha\kappa} \, \mathcal{P}_1(\vec{z},t_0;\vec{x},t_0)^{cb}_{\kappa\rho} \, \xi_{[r]}(\vec{x}) \, \gamma^5_{\rho\beta} = \psi^{\rm high}_{[r]}(y;t_0)^{ab}_{\alpha\rho} \, \gamma^5_{\rho\beta}, \qquad (4.23)$$

and the result is analogous to the standard one-end trick, with an additional γ^5 contraction.

In conclusion we have found that the quantity which should be used in the hybrid one-end trick is

$$\psi_{[r]}(y;t_0)^{ab}_{\alpha\beta} \to \sum_{\vec{x}} \sum_{i=1}^{N_{\rm ev}} \frac{1}{\lambda_i} v^{[i]}(y)^a_\alpha \, v^{[i]}(\vec{x},t_0)^{b\dagger}_\rho \, \gamma^5_{\rho\beta} \, \xi_{[r]}(\vec{x}) + \psi^{\rm high}_{[r]}(y;t_0)^{ab}_{\alpha\rho} \, \gamma^5_{\rho\beta}. \qquad (4.24)$$

We have not been able to obtain reasonable numerical results using the hybrid method. One primary issue that we were unable to overcome in implementing the method is that, through repeated iterations of the algorithm for calculating the inverse Fermion matrix and finite precision, the high-mode solution may lose its orthogonality to the low modes.

We have concluded from the work of this chapter that, to obtain the desired precision for the work of the following chapters, a combination of source dilution and source/sink smearing is sufficient.

Chapter 5

π^0–η–η' masses and state mixing

As in Chapter 3, we are again interested in studying the mixtures of SU(3)-flavour states which form the eigenstates of QCD+QED, only now in the sector of flavour-neutral (FN) pseudoscalar (PS) mesons. If the masses and charges of the up, down and strange quarks were degenerate, in the typical isospin construction the π^0 and η would exist as pure FN isovector and isoscalar members of the PS meson octet, respectively, analogous to the Σ^0 and Λ. The η' would then occupy its own multiplet as an SU(3)-flavour singlet, for which there is no low-lying baryon analogue. In reality, where SU(3)-flavour symmetry is broken, these FN PS states are permitted to mix, and quantifying the extent of this mixing is important for theoretical and phenomenological studies where interpolating operators are used to project onto the physical eigenstates.

In the isospin limit, which is often evoked as a reasonable approximation to reality, the η and η' mesons will become mixtures of the relevant octet and singlet states where full SU(3)-flavour symmetry is broken by the strange quark. The magnitude of this mixing is understood to be quite large in reality, assuming isospin-breaking is negligible, of the order 10–20° [40]. If isospin symmetry is no longer assumed, all three FN PS eigenstates will form from admixtures of the octet and singlet states. The mixing of the FN octet states is expected to be small, as may be inferred from the relatively small level of isospin-breaking in nature, of the order 1° [95] and comparable with the analogous Σ^0–Λ mixing. The FN isovector and flavour-singlet mixing is expected to be smaller still, however numerical results including broken isospin are few and limited to phenomenology [95–97], with little consensus. Furthermore, it has been shown that mixing induced by broken isospin could have more significant than expected effects on the $K\pi$-puzzle [98].

Existing lattice QCD studies [37–39,88,99,100] have worked in the limit of isospin symmetry, hence excluding π^0 admixture, and presented determinations of the η–η' mixing with fair consensus and agreement with phenomenology [40]. However, it is important to note that the majority of these existing η–η' mixing studies, lattice and otherwise, have focused on the mixing of decay constants (defined through the couplings of the mesons to axial-vector currents, see Chapter 6), either under the assumption that their mixing behaviour is mirrored in the state mixing, or simply without reference to the mixing of the states. The decay constant picture has many

interesting aspects, for example its close proximity to the axial anomaly [101], but it is understood in general that the mixing of FN PS states through the coupling to pseudoscalar operators will not follow that observed in the decay constants [102].

We have spent the previous chapter, Chapter 4, developing the machinery necessary to accurately calculate the disconnected diagrams that arise from Wick contractions of FN operators. Since all of the non-trivial mixing occurs through these disconnected diagrams [37], the success of this work is heavily dependent on our ability to do this within our computational means.

In this chapter we will introduce the interpolating operators and correlation functions to be calculated on the lattice, before discussing the diagonalization of the eigenstates and quantities of interest: the PS meson masses and state compositions. We also introduce the quark-mass extrapolation scheme used, present preliminary fits to our lattice results and observe some interesting features of the mixing in the quark-mass region of our ensembles. Moreover, we resolve the mass-splitting between the π^0 and η for the first time on the lattice. While the precision achieved for the η' mass is low, we are still able to resolve its state composition with fair precision on each of our ensembles and at the physical point. The work presented in this chapter is the subject of our publication [103].

5.1 Lattice computation of pseudoscalar mesons

We will now introduce the method by which we investigate the masses and state mixing of the pseudoscalar meson nonet (the octet and singlet) on the lattice. The process will be similar in many ways to that employed in Chapter 3. Some added complications in this scenario are the presence of the SU(3)-flavour singlet mixing with the FN isovector and isoscalar states, as well as the computational nuisance presented by the quark-loop contributions which we are now equipped to deal with following the work of Chapter 4.

5.1.1 Interpolating operators and correlation functions

As with the Σ^0 and Λ, there is a canonical choice of interpolating operator basis for the π^0, η and η' provided by the isospin-centric construction of wavefunctions in SU(3)-flavour symmetry. We refer to this basis as the 'octet-singlet' basis, and it is given by

$$\mathcal{O}_{\pi_3} = \frac{1}{\sqrt{2}}(\bar{u}\gamma^5 u - \bar{d}\gamma^5 d), \quad \mathcal{O}_{\eta_8} = \frac{1}{\sqrt{6}}(\bar{u}\gamma^5 u + \bar{d}\gamma^5 d - 2\bar{s}\gamma^5 s),$$

$$\mathcal{O}_{\eta_1} = \frac{1}{\sqrt{3}}(\bar{u}\gamma^5 u + \bar{d}\gamma^5 d + \bar{s}\gamma^5 s), \tag{5.1}$$

where the first two operators, labelled π_3 and η_8, are the octet iso-vector and iso-scalar respectively, and the final operator is the flavour-singlet, labelled η_1. We herein reserve the standard labels π^0, η and η' for the mass eigenstates. When

SU(3)-flavour symmetry is exact, these operators are orthogonal in the sense that

$$\langle 0|\mathcal{O}_i\mathcal{O}_j^\dagger|0\rangle \propto \delta_{ij}, \quad i,j = \pi_3, \eta_8, \eta_1. \tag{5.2}$$

However, when SU(3)-flavour symmetry is broken by a non-degenerate strange quark, the η_8 and η_1 operators are no longer orthogonal. If SU(3)-flavour symmetry is further violated by breaking the residual isospin symmetry, none of the octet-singlet operators remain orthogonal.

Where broken flavour-symmetry is being considered, another common choice of operator basis is the 'quark-flavour' basis, which is given simply by the pseudoscalar Dirac bilinear for each quark flavour,

$$\mathcal{O}_u = \bar{u}\gamma^5 u, \quad \mathcal{O}_d = \bar{d}\gamma^5 d, \quad \mathcal{O}_s = \bar{s}\gamma^5 s. \tag{5.3}$$

Clearly we are free to choose either basis for the purpose of calculating properties of the flavour-neutral pseudoscalar mesons, and where mixing is concerned, convert results regarding one basis to the other afterwards through a change-of-basis.

For the small lattice volumes and large quark masses used in this study we do not need to consider potential contamination by other low-lying states, such as 2γ and 3π channels, due to their relatively high energies. Additionally, although in principle our states of interest may overlap with glueball or heavy quark operators, we expect our interpretation of the flavour-compositions herein to be a good approximation of the low energy physics, as these additional states have previously been found to have negligible overlap with the flavour-neutral pseudoscalar mesons at our level of precision [104].

Correlation functions

We choose to use the more computationally natural of the two presented bases, the quark-flavour basis, and we introduce an extension of this basis by including two different levels of gauge-covariant Gaussian smearing for each operator. The motivation for extending our variational basis in the smearing degree-of-freedom is that there is good evidence that doing so can help to control the excited states [105–108], such that in our case the ground states can be resolved at smaller Euclidean times than would otherwise be possible. This is particularly advantageous since stochastic estimators of quark-loop contributions usually tend towards noise at smaller Euclidean times than connected quantities. Moreover, as mentioned in Chapter 4, whilst stochastic estimation of quark-loop diagrams can be expensive, applying different levels of source and sink smearing to the loops comes at very little extra cost (no additional inversions).

Using our basis of six interpolating operators we construct the (6×6) matrix of correlation functions with elements

$$C_{ij}(t) = \sum_{\vec{x},\vec{y}} \langle \mathcal{O}_j(\vec{y},t)\, \mathcal{O}_i^\dagger(\vec{x},0)\rangle, \quad i,j = \mathcal{O}_u^{(1)}, \mathcal{O}_d^{(1)}, \mathcal{O}_s^{(1)}, \mathcal{O}_u^{(2)}, \mathcal{O}_d^{(2)}, \mathcal{O}_s^{(2)}, \tag{5.4}$$

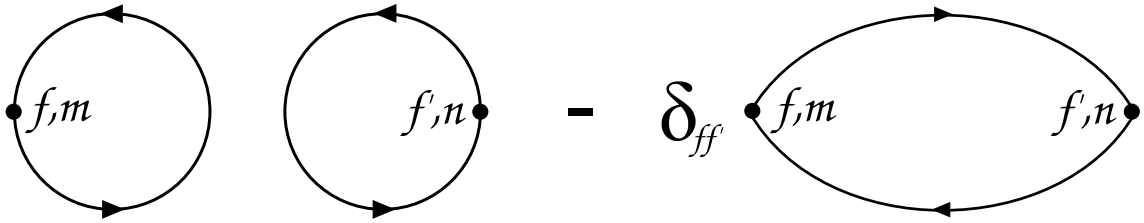

Figure 5.1: Feynman diagrammatic representation of the quark-flavour basis correlation functions with source and sink flavours f and f' respectively, and their corresponding smearing levels m and n (Equation (5.5)). The left-most diagram (two loops) is the quark-loop contribution, which is responsible for correlations between non-degenerate quarks, as well as most of the computational complexity of the calculation. The right-most diagram is the connected contribution, which is only present for source and sink operators of the same quark flavour.

where the superscripts $(1), (2)$ indicate the two levels of smearing applied to the quark-flavour operators, Equation (5.3). Explicitly, smearing level (1) corresponds to 25 sweeps of gauge-covariant Gaussian smearing as defined in Equation (4.12) ($\alpha = 0.7$), and (2) to 100 sweeps. Owing to the simple nature of the quark-flavour basis, all 36 of the Wick-contracted correlation functions can be summarized as

$$C_{ff'}^{(m,n)}(t) = \sum_{\vec{x},\vec{y}} \mathrm{Tr}\big[\gamma^5\, S_{f'}^{(n,n)}(\vec{y},t;\vec{y},t)\,\big]\mathrm{Tr}\big[\gamma^5\, S_{f}^{(m,m)}(\vec{x},0;\vec{x},0)\,\big]$$

$$- \delta_{ff'}\,\mathrm{Tr}\big[\,S_{f'}^{(n,m)}(\vec{y},t;\vec{x},0)\,S_{f}^{(n,m)}(\vec{y},t;\vec{x},0)\,\big], \qquad (5.5)$$

where the correlation function indices f/m and f'/n label the flavours/smearing levels of the source and sink operators respectively. The trace indicated by $\mathrm{Tr}[\ldots]$ is taken in both Dirac and colour indices, and there is no implied sum over f/f' in the second term. We present a diagrammatic representation of Equation (5.5) in Figure 5.1.

The first term of Equation (5.5) is the disconnected quark-loop contribution to the correlation function, which is present regardless of the respective flavours of the source and sink operators. The quark propagators in this term are examples of the self-to-self propagator introduced in Chapter 4, and following the work in that chapter we are now equipped to calculate them using $\mathbb{Z}_2$ wall-sources. We have chosen to use three independent noise-sources, each with spin, colour and time dilution, on each gauge-field configuration. Since we have calculated the self-to-self propagator on each timeslice, it is a straightforward improvement to replace

$$\sum_{\vec{x},\vec{y}} \mathrm{Tr}\big[\gamma^5\, S_{f'}^{(n,n)}(\vec{y},t;\vec{y},t)\,\big]\mathrm{Tr}\big[\gamma^5\, S_{f}^{(m,m)}(\vec{x},0;\vec{x},0)\,\big] \quad \longrightarrow$$

$$\frac{1}{N_t}\sum_{t'}\sum_{\vec{x},\vec{y}} \mathrm{Tr}\big[\gamma^5\, S_{f'}^{(n,n)}(\vec{y},t+t';\vec{y},t+t')\,\big]\mathrm{Tr}\big[\gamma^5\, S_{f}^{(m,m)}(\vec{x},t';\vec{x},t')\,\big], \qquad (5.6)$$

effectively averaging over all possible source times.

The second term of Equation (5.5), which is only present where the source and sink operator flavours are the same, is the connected contribution to the correlation function. In practice, a determination of this two-point function could most easily be achieved via the use of point-to-all propagators, as is common in lattice QCD. Here however, to achieve noise correlation between the disconnected and connected contributions, as well as achieve the indicated sum over spatial source-locations, we use the one-end trick as detailed in Equation (4.15). Note that in order to achieve the desired source smearing using the one-end trick we must apply the smearing to the source vector before inversion, although for the one-end trick we utilize only a single lattice timeslice source location.

5.1.2 Diagonalization

Before performing the diagonalization we introduce the spectral decompositions of our correlation functions at large Euclidean time,

$$
\begin{aligned}
C_{ij}(t) &= \sum_{\vec{x},\vec{y}} \langle \mathcal{O}_j(\vec{y},t)\, \mathcal{O}_i^\dagger(\vec{x},0)\rangle \\
&= \sum_{\vec{x},\vec{y}} \sum_{n} \sum_{\vec{p}} \frac{e^{-E_{n,\vec{p}}t}}{2\,E_{n,\vec{p}}\,L^3} \langle 0|\, \mathcal{O}_j\, e^{i\vec{p}\cdot\vec{y}}\, |n(\vec{p})\rangle\, \langle n(\vec{p})|\, e^{-i\vec{p}\cdot\vec{x}}\, \mathcal{O}_i^\dagger\, |0\rangle \\
&= \sum_{n} \sum_{\vec{p}} \frac{e^{-E_{n,\vec{p}}t}}{2E_{n,\vec{p}}L^3} \langle 0|\mathcal{O}_j|n(\vec{p})\rangle\, \langle n(\vec{p})|\mathcal{O}_i^\dagger|0\rangle \sum_{\vec{x},\vec{y}} e^{-i\vec{p}\cdot\vec{x}} e^{i\vec{p}\cdot\vec{y}} \\
&= \sum_{n} \sum_{\vec{p}} \langle 0|\mathcal{O}_j|n(\vec{p})\rangle\, \langle n(\vec{p})|\mathcal{O}_i^\dagger|0\rangle\, \frac{e^{-E_{n,\vec{p}}t}}{2E_{n,\vec{p}}\,L^3}\, (2\pi)^6\, \delta^3(\vec{p})\, \delta^3(-\vec{p}) \\
&\xrightarrow[t\to\infty]{} \sum_{n=1}^{6} \frac{L^3}{2M_n} \langle 0|\mathcal{O}_j|n\rangle\, \langle n|\mathcal{O}_i^\dagger|0\rangle\, e^{-M_n t}, \qquad (5.7)
\end{aligned}
$$

where we have truncated the sum of states to the six least energetic ground-states at sufficiently large Euclidean time. As discussed in Section 2.2, we find it advantageous to consider the backwards-propagating states occurring due to our boundary conditions, and so we instead consider

$$
C_{ij}(t) \xrightarrow[t\to\infty]{} \sum_{n=1}^{6} \frac{L^3}{2M_n} \langle 0|\mathcal{O}_j|n\rangle\, \langle n|\mathcal{O}_i^\dagger|0\rangle\, \left(e^{-M_n\, t} \,+\, e^{-(T-t)M_n}\right), \qquad (5.8)
$$

where T is the full time-extent of the lattice.

In Chapter 3 we introduced the generalized eigenvalue problem (GEVP) [75, 76] as an alternative to the straightforward eigenvalue problem which we ultimately utilized therein. Here we are interested in both eigenvectors and eigenvalues, and we instead favour the GEVP for its reduction of eigenvalue uncertainties. Note that

the eigenvectors are mathematically equivalent between the two methods provided that, as usual, we have gone to sufficiently large Euclidean times.

We invoke the eigenvectors $\vec{v}_m$ at large Euclidean times, which, for the real and symmetric matrix of correlation functions exhibit the property

$$\sum_{j=1}^{6} \frac{L^{3/2}}{\sqrt{2M_n}} \langle 0|\mathcal{O}_j|n\rangle \, [\vec{v}_m]_j = \delta_{nm}, \tag{5.9}$$

noting that the matrix being real implies that $\langle 0|\mathcal{O}_i|n\rangle = \langle n|\mathcal{O}_i^\dagger|0\rangle$. Ignoring the backwards-propagating states momentarily, we can calculate these eigenvectors as the solutions to the GEVP given by

$$C(t_0)^{-1} \, C(t_0 + \delta t) \, \vec{v}_n = e^{-M_n \delta t} \, \vec{v}_n. \tag{5.10}$$

Once we have solved the GEVP, we can diagonalize our matrix of correlation functions at sufficiently large t as $\vec{v}_n^T \, C(t) \, \vec{v}_n = \left(e^{-M_n t} + e^{-(T-t)M_n}\right)$, in order to extract the ground-state masses. The three least-energetic states are the π^0, η and η'.

In addition to the masses of the eigenstates, we also determine the overlaps of the quark-flavour operators at large times as

$$\frac{2M_n}{L^3} \left(e^{-M_n t} + e^{-(T-t)M_n}\right)^{-1} \sum_{j=1}^{6} C_{ij}(t) \, [\vec{v}_n]_j = \langle n|\mathcal{O}_i^\dagger|0\rangle, \tag{5.11}$$

by fitting the left-hand side of the above expression to a constant at sufficiently large times, for each $n \leq 3$ and i. We define the re-scaled overlaps for a fixed smearing level l as the relative weight of flavour f in the eigenstate $|n\rangle$,

$$\langle 0|\tilde{\mathcal{O}}_f^{(l)}|n\rangle \equiv \frac{\langle 0|\mathcal{O}_f^{(l)}|n\rangle}{\sqrt{\sum_{f'=u,d,s} |\langle 0|\mathcal{O}_{f'}^{(l)}|n\rangle|^2}}, \quad f = u, d, s. \tag{5.12}$$

As can be seen from Equation (5.9), the overlaps of Equation (5.11) are in fact proportional to the eigenvectors in the sense that

$$\vec{v}_n \propto \left[\langle 0|\mathcal{O}_u^{(1)}|n\rangle, \langle 0|\mathcal{O}_d^{(1)}|n\rangle, \langle 0|\mathcal{O}_s^{(1)}|n\rangle, \langle 0|\mathcal{O}_u^{(2)}|n\rangle, \langle 0|\mathcal{O}_d^{(2)}|n\rangle, \langle 0|\mathcal{O}_s^{(2)}|n\rangle\right]^T, \tag{5.13}$$

and hence either the eigenvectors or overlaps may be used to form operators which diagonalize the FN PS mesons.

In principle, it may be true that the quark-flavour operators of one smearing level couple to the eigenstates in different proportions to those of the other smearing level, i.e.

$$\left[\langle 0|\mathcal{O}_u^{(1)}|n\rangle, \langle 0|\mathcal{O}_d^{(1)}|n\rangle, \langle 0|\mathcal{O}_s^{(1)}|n\rangle\right] \not\propto \left[\langle 0|\mathcal{O}_u^{(2)}|n\rangle, \langle 0|\mathcal{O}_d^{(2)}|n\rangle, \langle 0|\mathcal{O}_s^{(2)}|n\rangle\right]. \tag{5.14}$$

In this work we find statistical consistency for proportionality between the two smearing levels on our lattice ensembles, the κ-values for which can be found in Table 5.1. As an example of this, on our Ensemble 1 we find

$$\frac{\langle 0|\mathcal{O}_u^{(1)}|\eta\rangle}{\langle 0|\mathcal{O}_d^{(1)}|\eta\rangle} = -2.097(23), \quad \frac{\langle 0|\mathcal{O}_u^{(2)}|\eta\rangle}{\langle 0|\mathcal{O}_d^{(2)}|\eta\rangle} = -2.080(25), \tag{5.15}$$

which implies from Equation (5.12) that $\langle 0|\tilde{\mathcal{O}}_f^{(1)}|n\rangle = \langle 0|\tilde{\mathcal{O}}_f^{(2)}|n\rangle$, and we hence drop the smearing-level label on our rescaled operators: $\langle 0|\tilde{\mathcal{O}}_f|n\rangle$. Finally, due to this proportionality, we may write our operators which diagonalize the FN PS mesons simply as

$$\mathcal{O}_n^\star = \sum_{f=u,d,s} \langle 0|\tilde{\mathcal{O}}_f|n\rangle\, \mathcal{O}_f, \tag{5.16}$$

where, for our purposes, arbitrary smearing may be associated with the quark-flavour operators $\mathcal{O}_f$. We will interchangeably refer to the re-scaled overlaps $\langle 0|\tilde{\mathcal{O}}_f|n\rangle$ as the flavour-contents or flavour-compositions of the eigenstates $|n\rangle$.

The outer-ring pseudoscalar mesons

In addition to the FN PS meson system already discussed, we also determine the masses of the outer-ring octet mesons: π^+, K^+ and K^0, which are already diagonalized by their standard octet SU(3)-flavour wavefunctions. To achieve this we solve a GEVP for each species, with the respective correlation function matrices having elements

$$C_{mn}^{\pi^+}(t) = \sum_{\vec{x},\vec{y}} \langle (\bar{q}_d\gamma^5 q_u)(\vec{y},t)^{(n)}\, (\bar{q}_d\gamma^5 q_u)^\dagger(\vec{x},0)^{(m)}\rangle \tag{5.17}$$

$$C_{mn}^{K^+}(t) = \sum_{\vec{x},\vec{y}} \langle (\bar{q}_s\gamma^5 q_u)(\vec{y},t)^{(n)}\, (\bar{q}_s\gamma^5 q_u)^\dagger(\vec{x},0)^{(m)}\rangle \tag{5.18}$$

$$C_{mn}^{K^0}(t) = \sum_{\vec{x},\vec{y}} \langle (\bar{q}_d\gamma^5 q_s)(\vec{y},t)^{(n)}\, (\bar{q}_d\gamma^5 q_s)^\dagger(\vec{x},0)^{(m)}\rangle, \tag{5.19}$$

where the indices m and n enumerate the two smearing levels already detailed. Analogous to the FN species, we calculate the necessary eigenvectors via the GEVP's

$$\begin{aligned} C^{\pi^+}(t_0)^{-1}\, C^{\pi^+}(t_0+\delta t)\, \vec{v}_n^{\pi^+} &= \lambda_n^{\pi^+}\, \vec{v}_n^{\pi^+}, \\ C^{K^+}(t_0)^{-1}\, C^{K^+}(t_0+\delta t)\, \vec{v}_n^{K^+} &= \lambda_n^{K^+}\, \vec{v}_n^{K^+}, \\ C^{K^0}(t_0)^{-1}\, C^{K^0}(t_0+\delta t)\, \vec{v}_n^{K^0} &= \lambda_n^{K^0}\, \vec{v}_n^{K^0}, \end{aligned} \tag{5.20}$$

for the same δt and two values of t_0 used for the FN mesons. The ground state masses are then extracted by fitting the appropriate combinations of exponential functions to the (large times) diagonalizations

$$\vec{v}_1^{\pi^+ T}\, C^{\pi^+}(t)\, \vec{v}_1^{\pi^+} = e^{-M_{\pi^+}\, t} + e^{-(T-t)M_{\pi^+}},$$

Lattice ensembles							
#	κ_u	κ_d	κ_s	#	κ_u	κ_d	κ_s
1	0.124362	0.121713	0.121713	4	0.124281	0.121752	0.121752
2	0.124374	0.121713	0.121701	5	0.124338	0.121760	0.121689
3	0.124400	0.121713	0.121677	6	0.124430	0.121760	0.121601

Table 5.1: The ensemble number labels and κ-values for each of the six (unitary) $n_f = 1+1+1$ QCD+QED ensembles used in this chapter. These ensembles are depicted in the quark-mass plane in Figure 5.2.

$$\begin{aligned} \vec{v}_1^{K^+T}\, C^{K^+}(t)\, \vec{v}_1^{K^+} &= e^{-M_{K^+}\, t} \,+\, e^{-(T-t)M_{K^+}}, \\ \vec{v}_1^{K^0T}\, C^{K^0}(t)\, \vec{v}_1^{K^0} &= e^{-M_{K^0}\, t} \,+\, e^{-(T-t)M_{K^0}}. \end{aligned} \tag{5.21}$$

Calculating the outer-ring mesons in this way, using a variational smearing analysis, is expected to give us increased control over excited states and does not require the calculation of any propagators in addition to those needed for the FN PS meson diagonalization.

5.1.3 Flavour-breaking expansions

As was done in Chapter 3 for the Σ^0–Λ mixing angle, we can parametrise our meson masses and overlaps by the light quark mass and charge parameters in order to correct for the dominant systematic error, which is the unphysical bare quark masses used. Such parametrisations around an SU(3) symmetric point have already been worked out for the pseudoscalar meson masses-squared in the flavour-breaking scheme [63]. The central idea of this extrapolation scheme is that particles belonging to certain multiplets under SU(3)-flavour symmetry have resulting group properties which must also be manifest in the expansion polynomials at each order. Therefore, at each order there is some finite combination of quark mass and charge polynomials which need be considered to parametrise the masses of the PS mesons.

Due to the exploratory nature of this work, we limit our parametrisations to leading order in the quark masses and charges. Taking, to leading order, the expressions presented in [65] for the purely connected outer-ring PS mesons,

$$M^2_{\pi^+} = M_0^2 \,+\, \beta_0^{\mathrm{EM}}(e_u^2 + e_d^2 + e_s^2) \,+\, \alpha(\delta m_u + \delta m_d) \,+\, \beta_2^{\mathrm{EM}}(e_u - e_d)^2, \tag{5.22}$$

$$M^2_{K^+} = M_0^2 \,+\, \beta_0^{\mathrm{EM}}(e_u^2 + e_d^2 + e_s^2) \,+\, \alpha(\delta m_u + \delta m_s) \,+\, \beta_2^{\mathrm{EM}}(e_u - e_s)^2, \tag{5.23}$$

$$M^2_{K^0} = M_0^2 \,+\, \beta_0^{\mathrm{EM}}(e_u^2 + e_d^2 + e_s^2) \,+\, \alpha(\delta m_d + \delta m_s). \tag{5.24}$$

In the above expressions δm_i is again the deviation of the i^{th} quark's mass from the approximate SU(3)-symmetric point (see Section 2.3): $\delta m_i = m_i - m_0$, e_i is the EM charge associated with the i^{th} quark, and M_0, β_0^{EM}, β_2^{EM} and α are fit parameters. Note that we have simplified the above expressions using the relation

$\delta m_u + \delta m_d + \delta m_s = 0$, which is a feature of our extrapolation scheme and true for all of our ensembles.

For the FN PS mesons the above set of parameters is not sufficient to describe the effects of the quark-loop diagrams contributing to their masses, and hence additional parameters are introduced. Since the mass-matrix is not diagonal in the octet-singlet basis, the masses of the relevant eigenstates must be obtained by diagonalization of some non-diagonal matrix, and to this end we again choose the simple quark-flavour basis. In the flavour-breaking scheme at leading order we have

$$\begin{bmatrix} M^2_{u\bar{u}} & M^2_{u\bar{d}} & M^2_{u\bar{s}} \\ M^2_{u\bar{d}} & M^2_{d\bar{d}} & M^2_{d\bar{s}} \\ M^2_{u\bar{s}} & M^2_{d\bar{s}} & M^2_{s\bar{s}} \end{bmatrix} = \left[M_0^2 + \beta_0^{\mathrm{EM}}(e_u^2 + e_d^2 + e_s^2)\right] \cdot \mathbb{I} + A \begin{bmatrix} 1 & 1 & 1 \\ 1 & 1 & 1 \\ 1 & 1 & 1 \end{bmatrix}$$

$$+ b_0 \begin{bmatrix} 2\delta m_u & \delta m_u + \delta m_d & \delta m_u + \delta m_s \\ \delta m_u + \delta m_d & 2\delta m_d & \delta m_d + \delta m_s \\ \delta m_u + \delta m_s & \delta m_d + \delta m_s & 2\delta m_s \end{bmatrix} + 2\beta_1^{\mathrm{EM}} \begin{bmatrix} e_u^2 & 0 & 0 \\ 0 & e_d^2 & 0 \\ 0 & 0 & e_s^2 \end{bmatrix}$$

$$+ 2\alpha \begin{bmatrix} \delta m_u & 0 & 0 \\ 0 & \delta m_d & 0 \\ 0 & 0 & \delta m_s \end{bmatrix} + a_1^{\mathrm{EM}} \begin{bmatrix} e_u^2 & e_u e_d & e_u e_s \\ e_u e_d & e_d^2 & e_d e_s \\ e_u e_s & e_d e_s & e_s^2 \end{bmatrix}. \tag{5.25}$$

The additional parameter A is the zeroth-order contribution arising from disconnected diagrams, and is responsible for octet-singlet mass-splitting even where SU(3)-flavour symmetry is realised, whilst the new parameters b_0 and a_1^{EM} correspond respectively to gluons and photons interacting with quark loops.

In the language of the flavour-breaking expansions employed in [65], we extend the 8×8 mass matrix considered therein for the PS meson octet to include the flavour singlet. We now have a 9×9 mass matrix, with a 3×3 block for the FN mesons. In addition to the terms in $8 \otimes 8$ considered in [65], we also have terms with the symmetries $1 \otimes 1$, $1 \otimes 8$ and $8 \otimes 1$, which are (trivially) decomposed as

$$1 \otimes 1 = 1, \quad 1 \otimes 8 = 8, \quad 8 \otimes 1 = 8. \tag{5.26}$$

The $1 \otimes 1$ term gives the A term of Eq. 5.25, whilst the $1 \otimes 8$ and $8 \otimes 1$ terms give the b_0 term.

We have checked that performing a Taylor expansion analogous to the method employed in Section 3.1.2, but of the 3×3 matrix of correlation functions with row and column indices enumerating the quark-flavour basis operators, returns a parametrisation sharing the same functional form as (5.25). Therefore it is appropriate that we fit our overlaps of Equation (5.12), which are proportional to eigenvectors of the aforementioned 3×3 matrix, to the eigenvectors of a function of this form. We do not require the parameters between the mass and overlap fits

to be equal, since the overlaps diagonalize the states but not necessarily the mass matrix.

On each ensemble then, the masses-squared extracted for each of the nonet mesons are simultaneously fit to Equations (5.22)–(5.24), as well as the eigenvalues of Equation (5.25) computed numerically. We have also determined the mass splitting $M_\eta - M_{\pi^0}$ on each ensemble via the ratio of the relevant correlation functions:

$$\frac{\vec{v}_{\pi^0}^T\, C(t)\, \vec{v}_{\pi^0}}{\vec{v}_\eta^T\, C(t)\, \vec{v}_\eta} = e^{(M_\eta - M_{\pi^0})t}, \tag{5.27}$$

and subsequently fitting the effective mass, which is also included in the simultaneous fit. Independently of these mass fits, the re-scaled overlaps are fit to the numerically computed eigenvectors of a fit function with the form of Equation (5.25).

5.2 Results

The lattice simulations for this work were performed on six ensembles, with κ-values and naming labels given in Table 5.1. All ensembles are $24^3 \times 48$, $n_f = 1 + 1 + 1$, dynamical QCD+QED with quark masses around a U-spin symmetric point ($m_d = m_s$), with m_u tuned to approximate SU(3) symmetry, as detailed in Chapter 2. Ensembles 1–3 were employed previously in Chapter 3, and were chosen based on symmetries in the masses of the connected-only FN PS mesons. In particular, these ensembles span a quark-mass region which exhibits a wide variety of different mixing regimes, as we will soon observe. The three additional ensembles, 4–6, were required in order to better constrain our parametrisations through variation of the down-quark mass, and are chosen also holding $m_u + m_d + m_s = constant$. All of our ensembles are depicted on the plane of constant $\bar{m}$ in Figure 5.2, along with the physical point. Lines of constant m_d which our ensembles lie on are denoted by the red dashed lines, while the U-spin symmetric line is shown by the blue dashed line.

In solving the GEVP, Equation (5.10), we have chosen $\delta t = 1$ and calculated the eigenvectors for both $t_0 = 4$ and $t_0 = 5$. The mass and overlap results for each value of t_0 are treated as independent bootstrap samples in our error analysis, in order to estimate some of the systematic uncertainty associated with the choice. This is because in practice, the value of t_0 is restricted to relatively small times due to the quickly increasing statistical uncertainty, whereas the GEVP diagonalizations detailed herein are large Euclidean time expressions.

We present an example of the extracted signals of the diagonalized PS meson correlation functions in Figure 5.3, along with the effective mass of the splitting $M_\eta - M_{\pi^0}$, all on Ensemble 1 for $t_0 = 4$. Since the η' signal contains most of the disconnected contribution, on each ensemble we find it necessary to fit the η' at earlier times than the remaining nonet states. Again for Ensemble 1 and $t_0 = 4$ we present an example of the re-scaled overlap signal, as determined from the left-hand side of Equation (5.11) and the re-scaling Equation (5.12), in Figure 5.4. Clearly,

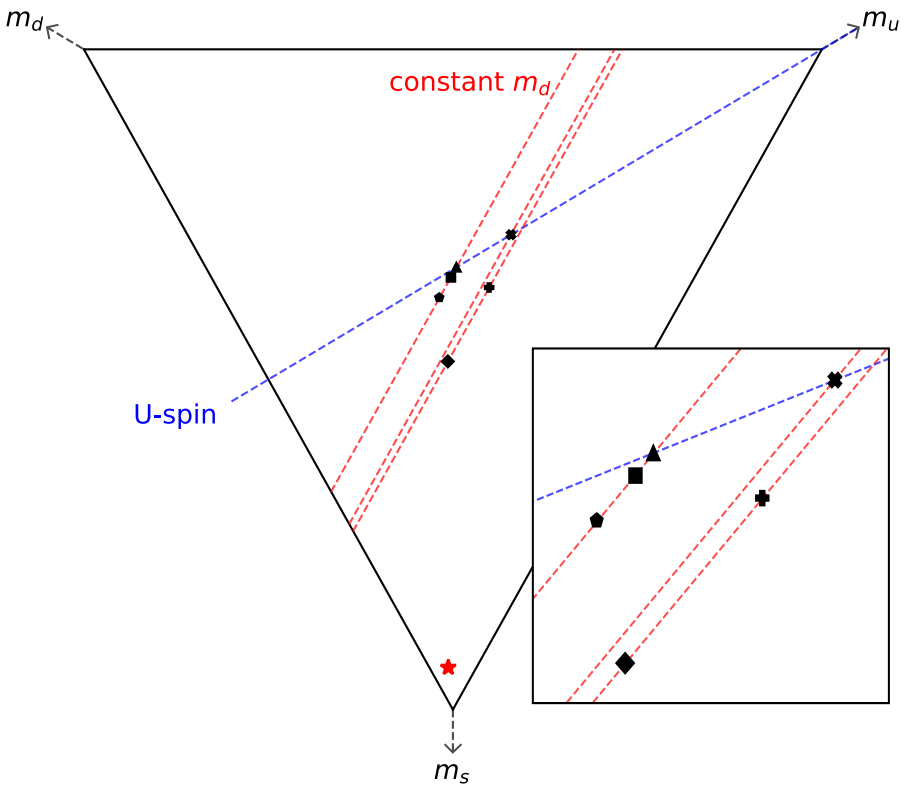

Figure 5.2: A visualisation of our six ensembles on the plane of constant average bare quark mass, including a close-up view of the ensemble locations, along with the physical point indicated by a red star. The red dashed lines indicate paths of constant m_d, whilst the blue dashed line shows where the down and strange quarks are degenerate and thus U-spin symmetry is exact. The ensembles, as detailed in Table 5.1, are 1 (triangle), 2 (square), 3 (pentagon), 4 (x), 5 (plus) and 6 (diamond).

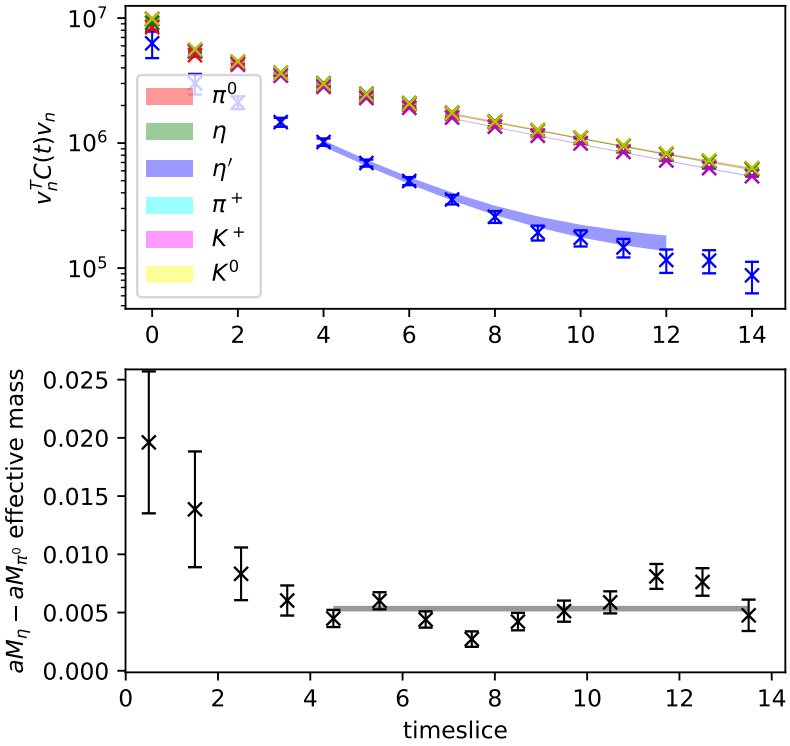

Figure 5.3: An example of the signals obtained for the PS mesons from the GEVP on Ensemble 1: correlation functions (top) and $M_\eta - M_{\pi^0}$ effective mass (bottom), along with their respective fits.

after re-scaling the overlaps are largely time independent, and can be confirmed to agree statistically with the normalized (to unity) eigenvectors. All of the extracted overlap and mass parameters are presented in Tables 5.2 and 5.3 respectively.

In Figure 5.5 we present a visual summary encapsulating most of our lattice results for this chapter, in particular all of the overlaps and octet masses from each of our six ensembles, along with their respective global fits. The χ^2/dof for the two global fits are 2.4 and 2.1 for the overlaps and masses respectively. The fit parameters for the masses-squared and overlap fits are given in Tables 5.4 and 5.5 respectively. Note that the presented overlap fit parameters are determined from a fit to the mean values of the FN overlaps, since the bootstrap-by-bootstrap fit parameters have variances which leave them consistent with zero, even though the resulting bootstrap-by-bootstrap fits do not. We stress that given the small lattice volumes and additional systematic uncertainties present, the quoted statistical uncertainties for our lattice data are expected to underestimate the true uncertainties, and simply adding an additional 2% uncertainty to our data as a conservative estimate of the systematic uncertainties lowers the χ^2/dof values to 1.1 and 0.6 for the overlap and mass fits respectively.

The two plots occupying the top row of Figure 5.5 each depict ensembles 1–3 (right-to-left), which all lie on the constant down-quark mass trajectory $\delta m_d = 0$. Ensemble 1 exhibits U-spin symmetry due to the degeneracy of the down and

Flavour compositions									
#	$\lvert\langle 0\rvert\tilde{\mathcal{O}}_u\rvert\pi^0\rangle\rvert^2$	$\lvert\langle 0\rvert\tilde{\mathcal{O}}_d\rvert\pi^0\rangle\rvert^2$	$\lvert\langle 0\rvert\tilde{\mathcal{O}}_s\rvert\pi^0\rangle\rvert^2$	$\lvert\langle 0\rvert\tilde{\mathcal{O}}_u\rvert\eta\rangle\rvert^2$	$\lvert\langle 0\rvert\tilde{\mathcal{O}}_d\rvert\eta\rangle\rvert^2$	$\lvert\langle 0\rvert\tilde{\mathcal{O}}_s\rvert\eta\rangle\rvert^2$	$\lvert\langle 0\rvert\tilde{\mathcal{O}}_u\rvert\eta'\rangle\rvert^2$	$\lvert\langle 0\rvert\tilde{\mathcal{O}}_d\rvert\eta'\rangle\rvert^2$	$\lvert\langle 0\rvert\tilde{\mathcal{O}}_s\rvert\eta'\rangle\rvert^2$
1	0.000(0)	0.500(0)	0.500(0)	0.682(9)	0.159(5)	0.159(5)	0.380(56)	0.310(28)	0.310(28)
2	0.111(46)	0.641(12)	0.248(53)	0.590(49)	0.019(12)	0.391(58)	0.380(26)	0.312(14)	0.309(13)
3	0.622(17)	0.360(21)	0.018(5)	0.090(14)	0.278(22)	0.632(8)	0.329(28)	0.333(14)	0.339(18)
4	0.000(0)	0.500(0)	0.500(0)	0.656(18)	0.172(9)	0.172(9)	0.462(46)	0.269(23)	0.269(23)
5	0.094(10)	0.664(10)	0.242(17)	0.594(10)	0.014(3)	0.392(12)	0.356(52)	0.329(49)	0.314(17)
6	0.511(20)	0.488(19)	0.001(1)	0.225(36)	0.161(25)	0.614(27)	0.337(46)	0.278(41)	0.385(67)

Table 5.2: The extracted overlaps squared of the physical states with the flavour basis operators on each of our ensembles.

PS meson masses (MeV)							
#	M_{π^0}	M_η	M_η-M_{π^0}	$M_{\eta'}$	M_{π^+}	M_{K^+}	M_{K^0}
1	457(5)	473(5)	15(1)	1234(51)	485(4)	485(4)	459(5)
2	475(4)	483(4)	10(1)	1219(118)	491(4)	498(4)	477(4)
3	446(9)	476(7)	28(1)	1165(54)	461(8)	478(8)	474(7)
4	430(11)	521(9)	86(3)	1519(127)	519(7)	519(7)	429(10)
5	405(8)	448(5)	50(3)	1156(70)	437(5)	464(4)	413(6)
6	404(7)	503(5)	97(2)	1058(50)	421(6)	499(4)	482(4)

Table 5.3: The extracted PS meson masses, as well as the mass-splitting $M_\eta - M_{\pi^0}$, for each of our six ensembles.

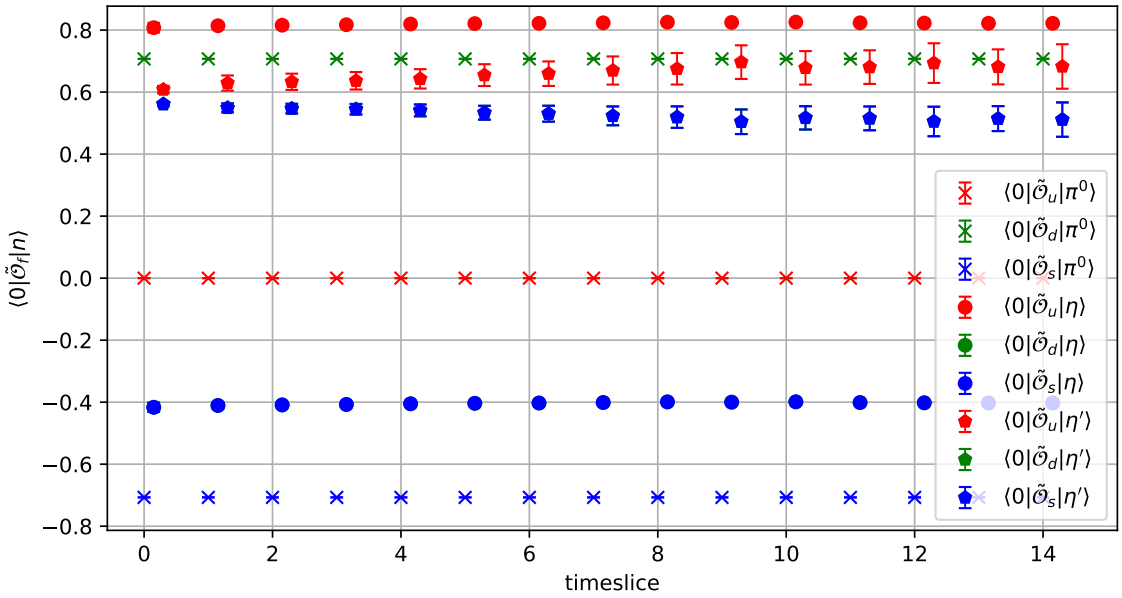

Figure 5.4: An example of the signals obtained for the FN PS meson (re-scaled) overlaps on Ensemble 1, as determined by the left-hand side of Equation (5.11) and the re-scaling Equation (5.12). A slight time offset has been applied to some signals for clarity.

Masses-squared expansion fit parameters						
C	A	α	b_0	a_1^{EM}	β_1^{EM}	β_2^{EM}
0.0244(2)	0.045(2)	1.51(2)	-1.3(4)	0.0025(1)	0.001(60)	0.00267(9)

Table 5.4: We have denoted $C \equiv M_0^2 + \beta_0^{\mathrm{EM}}(e_u^2 + e_d^2 + e_s^2)$ for the combination appearing identically in each mass expansion given in Section 5.1.3.

FN overlap expansion fit parameters				
A	α	b_0	a_1^{EM}	β_1^{EM}
0.0193	0.0998	0.3854	0.0001	0.0002

Table 5.5: The values of the overlap expansion parameters as determined from a fit to the bootstrap-means of the FN overlaps.

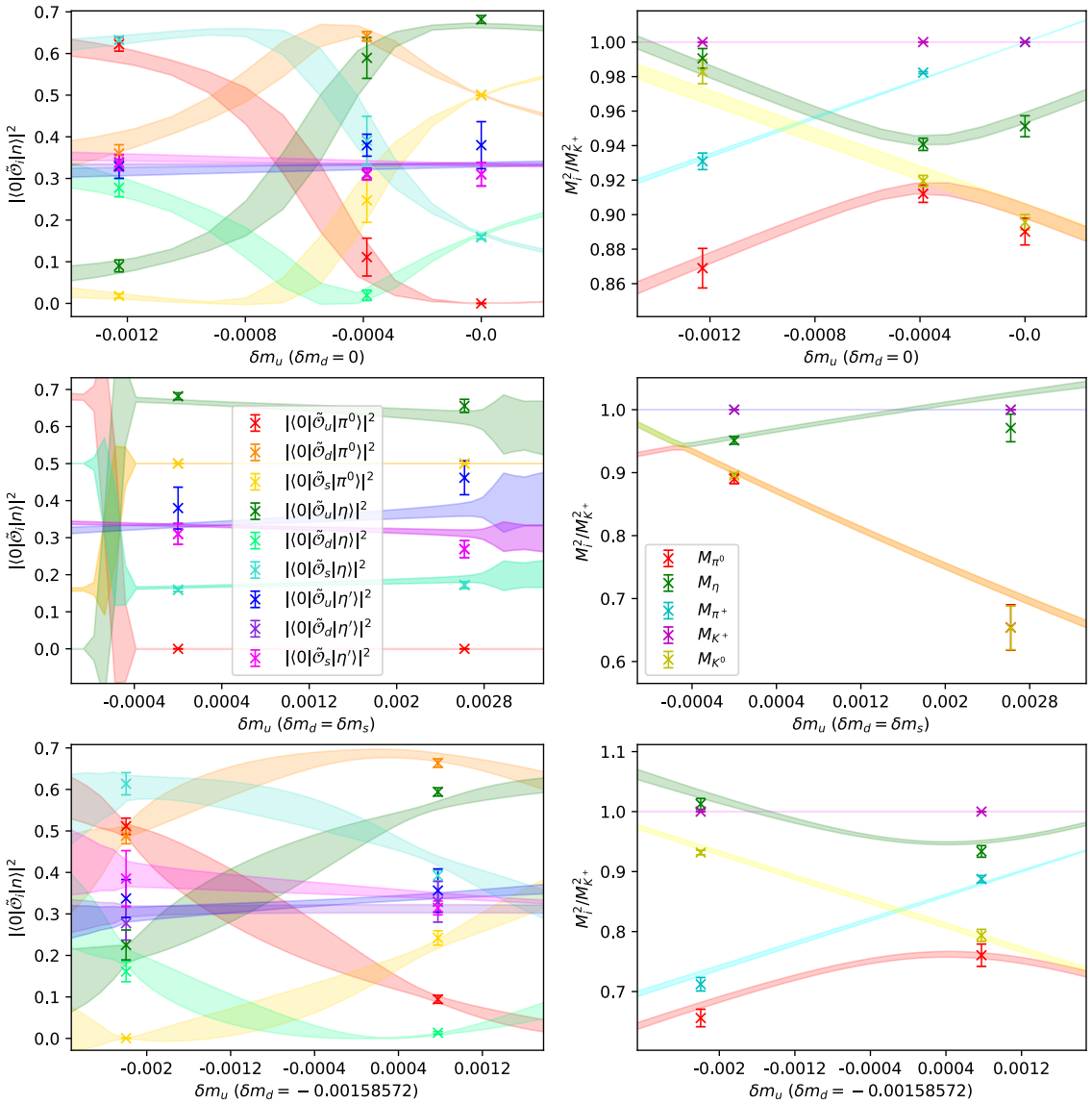

Figure 5.5: The overlaps (left column) and octet masses (right column) from each of our 6 ensembles with their respective global fits. The top pair of plots display ensembles 1–3 (right-to-left), which lie on the constant down quark mass trajectory $\delta m_d = 0$ (left-most dashed red line of Fig. 5.2). The center plots depict ensembles 1 and 4, which both exhibit U-spin symmetry (dashed blue line in Fig 5.2), whilst the bottom pair of plots depict ensembles 5 and 6, which lie on the constant down quark mass trajectory $\delta m_d = -0.00159$ (right-most dashed red line of Fig. 5.2). For a complete discussion of the features of this figure refer to Section 5.2.

strange quarks, and we can see as a result that the lightest FN PS meson exhibits the exact state composition of a U-spin π_3, $\pi_3^U = (\bar{d}\gamma^5 d - \bar{s}\gamma^5 s)/\sqrt{2}$, with its mass necessarily degenerate with that of the K^0. The η meson of Ensemble 2 has a flavour composition approaching that of a V-spin π_3, $\pi_3^V = (\bar{u}\gamma^5 u - \bar{s}\gamma^5 s)/\sqrt{2}$. Ensemble 2 also appears to be very near to the waist of an avoided level crossing between the π^0 and η mesons. Occurring along this mass trajectory and between Ensembles 2 and 3, as determined from the overlap fit, the π^0 becomes a pure isospin π_3 at $\delta m_u \approx -0.0008$.

The two plots that occupy the centre row of Figure 5.5 display the overlaps and octet masses of Ensembles 1 and 4 (left-to-right), which lie along a quark-mass trajectory where the down and strange quarks have equal masses, and the up-quark mass is fixed by our condition $\delta\bar{m} = 0$. Along this trajectory, indicated by the blue dashed line in Figure 5.2, we have hence enforced U-spin symmetry, and consequentially one of either the π^0 or η exhibit the flavour structure of a π_3^U throughout. A distinct feature of these plots is the level crossing observed in the π^0 and η masses at $\delta m_u \approx -0.0004$, and corresponding point in the overlaps where the state compositions change labels according to the flipped mass ordering. Additionally, one can observe that the three FN PS states approach their SU(3)-symmetric flavour compositions at the approximate location of Ensemble 1. The separation, in quark-mass space, of the level crossing and exact SU(3)-flavour-states points is a pure EM effect, as without EM these two phenomena would always occur together at points with equal light-quark masses (i.e. exact SU(3)-flavour symmetry). Additionally, the mass-splitting of about 2.5% between the charged and neutral octet-mesons, which we see at the point of M_{π^0}–M_η degeneracy in Figure 5.5 (centre row, right-hand plot), is also a pure EM effect.

The plots occupying the bottom row of Figure 5.5 depict the overlaps and octet masses of Ensembles 5 and 6 (right-to-left), which are situated on our lightest constant down quark mass trajectory, $\delta m_d = -0.0016$. The flavour composition of the η of Ensemble 5 is seen to be near that of a π_3^V, whilst the π^0 of Ensemble 6 is a very good approximation of an isospin π_3. Ensemble 6 exhibits the poorest overlap signal in our set, likely since it also possesses the lightest up and down quarks but has a comparable number of configurations to the other ensembles. The octet masses again exhibit an avoided level crossing between the π^0 and η, however with a much broader waist than that observed around Ensemble 2.

It is interesting to note that across the range of quark masses considered, the state compositions evolve between each of the distinct SU(2) subgroups: T-spin, U-spin and V-spin. In particular, as highlighted above, as δm_u changes in the top-left panel of Figure 5.5, we observe three distinct locations where one of the eigenstates appears as a pure π_3 state of a distinct SU(2) subgroup. Similarly, the lower-left panel also identifies pure π_3^T and π_3^V at particular values of δm_u. Using the parametrised description of the state composition we can trace out these distinct SU(2) subgroups in the quark mass plane, as shown in Figure 5.6. Each of the three lines corresponds to a trajectory where one of the eigenstates is a pure π_3; either

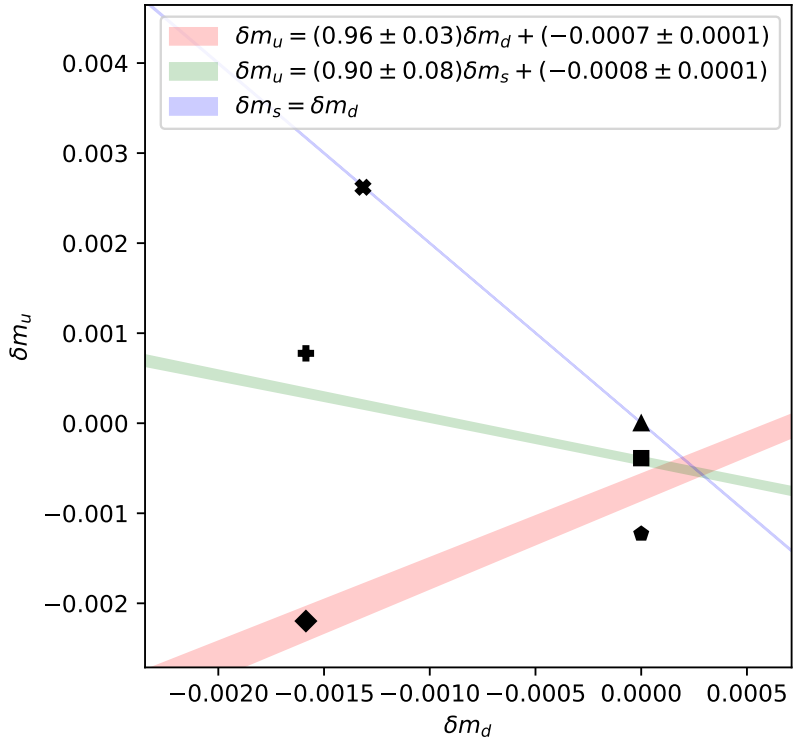

Figure 5.6: Lines of pure isospin (red), U-spin (blue) and V-spin (green) π_3 states as determined from our global fit to the extracted overlaps. The linear relationships in the legend indicate the symmetry condition between the relevant pairs of quarks, which are non-trivial for isospin and V-spin due to the presence of EM. Also illustrated are the locations of our Ensembles 1 (triangle), 2 (square), 3 (pentagon), 4 (x), 5 (plus) and 6 (diamond).

π_3^T, π_3^U or π_3^V. While the U-spin trajectory is exact, since the corresponding quark degeneracy is exact, the isospin and V-spin trajectories have slopes that are roughly compatible with maintaining degeneracy of the quark masses.

Figure 5.6 also suggests an improved definition of the SU(3) symmetric point, where the three lines appear to intersect together at a down quark mass slightly heavier than that of the nominal approximate SU(3) symmetric point introduced in Section 2.3. This intersection point also coincides with the point where the π^0 and η are degenerate along the U-spin symmetric line. While the approximate symmetric point was chosen such that the connected-only flavour-neutrals are degenerate [109, 110], the location identified here uses only physical states in the spectrum. In practice however, tuning lattice quark masses with respect to the disconnected correlation functions needed in this study would be unfeasible, and from the point of view of an expansion about an approximate SU(3) symmetric point, the consequence for any physical observable will always be equivalent up to the order of an expansion.

Although we currently lack ensembles at large enough $|\delta m_i|$ to constrain our parametrisation so as to effectively resolve the physical point mixing, we can assess our overlap extrapolation at the physical values of the quark masses, δm_i^*, the locations of which were determined in [65], albeit on a $32^3 \times 64$ volume,

$$a\delta m_u^\star = -0.00834(8), \quad a\delta m_d^\star = -0.00776(7). \tag{5.28}$$

We note that in this preliminary work we make no attempt to quantify the finite volume or lattice spacing effects in our results. We scale the parameters in our expansion that arise due to the inclusion of QED (note that β_0^{EM} doesn't contribute to the mixing) as was done in [72] to approximately correct our larger-than-physical EM coupling, and find

$$|\pi^0\rangle = 0.85(14)|\pi_3\rangle \,-\, 0.27(25)|\eta_8\rangle \,+\, 0.29(22)|\eta_1\rangle, \tag{5.29}$$

$$|\eta\rangle = -0.07(10)|\pi_3\rangle \,+\, 0.76(16)|\eta_8\rangle \,+\, 0.56(24)|\eta_1\rangle, \tag{5.30}$$

$$|\eta'\rangle = -0.005(2)|\pi_3\rangle \,-\, 0.26(10)|\eta_8\rangle \,+\, 0.96(3)|\eta_1\rangle. \tag{5.31}$$

With our relatively low level of precision at the physical point we cannot yet resolve much significant mixture of the π^0 with either the η or η', but we can see a small non-zero π_3 content in the η', although we would await a more precise calculation before drawing any physical conclusions. We do observe some clearly non-trivial admixtures of the η_8 and η_1 occurring in the physical η and η', and since all four numbers,

$$|\eta\rangle = \,0.76(16)|\eta_8\rangle \,+\, 0.56(24)|\eta_1\rangle, \quad |\eta'\rangle = -\,0.26(10)|\eta_8\rangle \,+\, 0.96(3)|\eta_1\rangle.$$

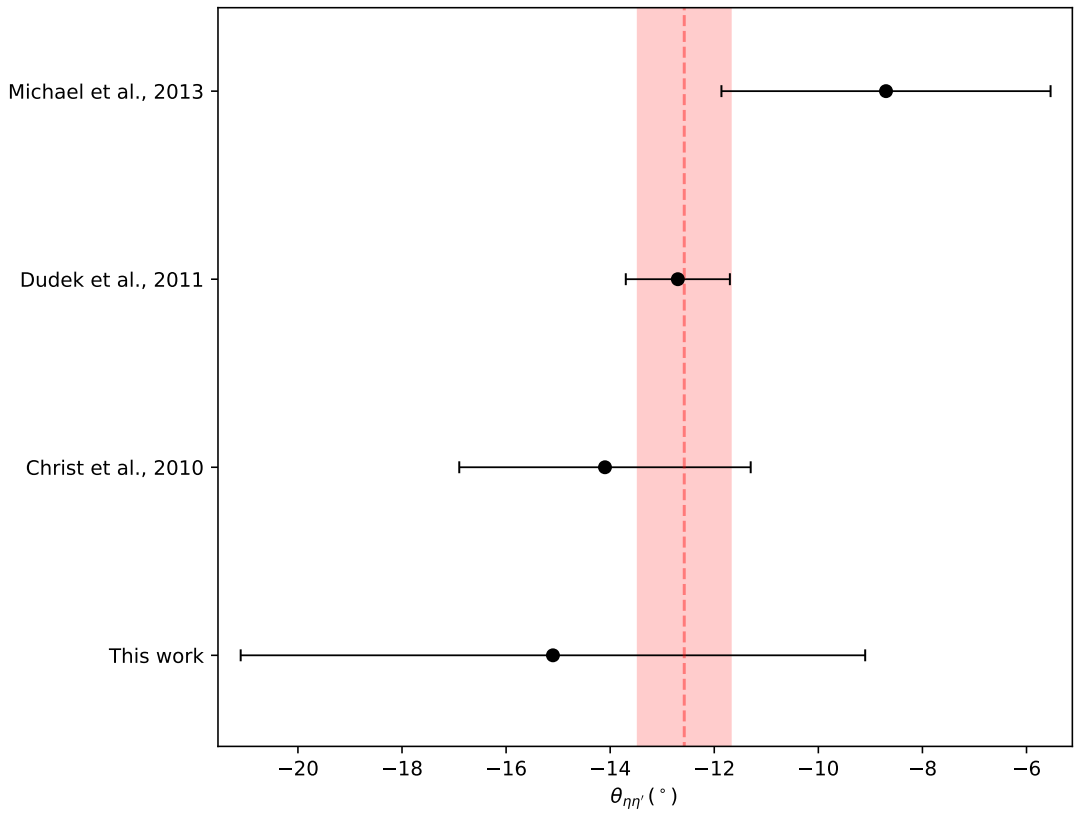

Figure 5.7: A comparison of the η–η' state mixing angle result of this work with the three existing determinations of Christ et al. [37], Dudek et al. [38] and Michael et al. [39], all performed in lattice QCD with exact isospin symmetry. Where statistical and systematic uncertainties are quoted we have added them in quadrature, and the dashed red line and shaded region give the weighted average of the four results and associated standard deviation: $\bar{\theta}_{\eta\eta'} = -12.6(9)^\circ$.

are consistent with parametrisation by a single mixing angle, we present a determination of said angle as

$$|\theta_{\eta\eta'}| = \sin^{-1}(-0.26 \pm 0.10) = (-15.1^{+5.9}_{-6})^\circ, \tag{5.32}$$

which is consistent with existing results from lattice QCD [37–39, 100] and phenomenology [111, 112], although it should be noted that many of these determinations define the mixing through the weak decay constants which need not follow the state mixing defined here. A comparison plot of mixing determinations using a state definition compatible with this work is presented in Figure 5.7.

While the extrapolation of the flavour compositions to the physical point presented here is considered only exploratory, we use the meson masses as a measure of the limitations of the present extrapolation. Using the physical quark mass point from [65], as above, we determine physical meson masses that are within 10-15% of observation. For instance, on the present small volume and low-order chiral extrapolation we obtain $M_{\pi^+} = 114(17)$MeV and $M_{K^+} = 551(2)$MeV. If however

we choose to instead constrain the quark mass parameters to give the physical meson masses M_{π^+} and M_{K^+}, the mixing angles do not appreciably differ from those reported above. As an example, with the alternative physical point tuned via the experimental meson masses, the η–η' mixing is determined to be $\theta_{\eta\eta'} = (-12.9^{+7.5}_{-7.8})^\circ$, which is in agreement with Equation (5.32).

5.3 Summary

In this chapter we have applied the central ideas of Chapter 3 to the FN PS mesons, extracting and extrapolating the state compositions, assisted by the computational techniques for calculating disconnected diagrams introduced in Chapter 4. Whilst the status of our extrapolation is exploratory, the results presented at the physical point agree in general with existing calculations of the η–η' mixing.

We have also calculated the masses of all PS nonet species on each of our ensembles, and notably, resolved the mass gap between the π^0 and η on the lattice. Using quark-mass extrapolations for the PS meson masses-squared, we were able to see some clear interplay between the masses and state compositions of the FN PS mesons, and in particular the influence of QED.

This program is promising for the purpose of calculating the physical-point PS state compositions of the FN PS mesons with high precision. Moreover, as we will see in the following chapter, the state compositions of the FN mesons inform other quantities such as their weak decay constants. To resolve the isospin-breaking effects reliably at the physical point we require additional ensembles farther from the approximate SU(3)-symmetric point so as to better constrain the quark-mass extrapolation. Such a precision calculation should also be performed in concert with continuum and infinite volume extrapolations.

Chapter 6

Decay constants of the pseudoscalar mesons

The pseudoscalar mesons are of particular interest in QCD due to their relationship to the spontaneous chiral symmetry breaking (SCSB) of the vacuum. In the chiral limit and without electromagnetism, the pseudoscalar octet species are understood to be massless Nambu-Goldstone bosons of SCSB, whilst the flavour-singlet η' procures a mass through an Adler-Bell-Jackiw anomaly [113–115] due to non-conservation of the singlet axial-vector current upon quantization. This anomaly is understood to arise from the non-trivial topological structure of the QCD vacuum [116], and is often studied in large-N_c perturbation theory [101, 117] whereby chiral symmetry may be restored. Moreover, a similar $U_A(1)$ anomaly in QED further breaks chiral symmetry and endows electroweak decays of the flavour-neutral (FN) pseudoscalar (PS) mesons with unique properties. Hence, with their relationship to SCSB and the dynamics of the physical vacuum, the FN PS mesons and their decays offer unique tests of fundamental physics which may prove fruitful in the search for physics beyond the standard model [40], for which experimental searches using them have recently been proposed [118].

These anomalies and their qualities, as they are understood in the chiral or SU(3)-flavour symmetric limits, are distributed between the FN PS mesons as they mix via flavour-symmetry breaking in the sense of the previous chapter. The decay constants which parametrise the couplings of PS eigenstates to axial-vector currents are important inputs for phenomenological and theoretical calculations, and a precise understanding of them including aspects such as isospin-breaking will be necessary for precision studies going forward.

We previously indicated in Chapter 5 that there is a common approach in lattice QCD and phenomenological studies to studying the mixing of FN PS mesons through their weak decay constants [40], usually in the approximation of isospin symmetry (no π^0 admixing). This approach corresponds to the parametrisation of a decay constant matrix in terms of two decay constants and two mixing angles [102, 111, 112, 119],

$$\begin{bmatrix} F_\eta^l & F_\eta^s \\ F_{\eta'}^l & F_{\eta'}^s \end{bmatrix} = \begin{bmatrix} F^l \cos\phi_l & -F^s \sin\phi_s \\ F^l \sin\phi_l & F^s \cos\phi_s \end{bmatrix}, \tag{6.1}$$

where the decay constants on the left-hand side, here in the quark-flavour basis, are defined through axial-vector matrix elements,

$$\langle 0|\, A_\mu^f \,|n(p)\rangle = ip_\mu F_n^f, \quad f = l, s, \quad n = \eta, \eta', \tag{6.2}$$

and the flavour index l represents the up and down quarks since exact isospin is assumed, such that

$$A_\mu^l = \frac{1}{\sqrt{2}}\left(\bar{u}\gamma_\mu\gamma_5 u + \bar{d}\gamma_\mu\gamma_5 d\right), \quad A_\mu^s = \bar{s}\gamma_\mu\gamma_5 s.$$

The quark-flavour basis is usually preferred in this context as the two mixing angles are thought to be approximately degenerate, $\phi_l \approx \phi_s$, however similar definitions can be made with respect to octet-singlet decay constants. Phenomenological studies have shown however that a single mixing angle is not sufficient to describe the experimental results in the octet-singlet basis [120].

It is clear that this concept of mixing is somewhat strained when contrasted with the mixing of correlation function matrices, as in Chapters 3 and 5. Since the decay constant matrix is not Hermitian, there is not necessarily a diagonalization proceeding via an $SO(n)$ matrix, except approximately in the case of the quark-flavour basis with isospin symmetry. Moreover, the 'diagonalized' decay constants, F^l and F^s, which one reaches using the mixing parametrisation are not any more physically significant than those appearing on the left-hand side of Equation (6.1).

In this work we proceed naturally from the work of the previous chapter. Having discussed the isolation and quark-mass parametrisation of the pseudoscalar state compositions of the FN PS mesons, we now aim to do the same for the decay constants F_n^f as defined by

$$\langle 0|\, A_\mu^f \,|n(p)\rangle = ip_\mu F_n^f, \quad A_\mu^f = \bar{q}_f\gamma_\mu\gamma_5 q_f, \quad f = u, d, s, \quad n = \pi^0, \eta, \eta'. \tag{6.3}$$

In this chapter we detail the determination of the above decay constants from lattice simulations, and present a quark-mass/charge extrapolation scheme which is shown to perform well in the quark-mass region where our ensembles are focused. We also discuss and present initial results for the non-perturbative renormalisation of the quark-flavour axial-vector currents appearing in Equation (6.3).

6.1 Decay constants on the lattice

In this section we give a detailed explanation of the PS meson decay constant calculation on the lattice, from the interpolating operators used to how the decay constants are determined from lattice correlation functions. We will also discuss the calculation of operator renormalisation factors in the RI'-MOM scheme, which are introduced to remove the effects of the regulator a as it pertains to the UV divergences of the path integral.

6.1.1 Lattice theoretic construction

We wish to calculate the couplings of the mass eigenstates to local axial-vector currents $A_\mu^f \equiv \bar{q}_f \gamma_\mu \gamma_5 q_f$, in order to determine the relevant quark-flavour decay constants as defined in Equation (6.3). Also of interest are the flavoured PS meson decay constants which are defined similarly as

$$\langle 0|\, \bar{d}\gamma_\mu\gamma_5 u \,|\, \pi^+(p)\,\rangle = ip_\mu F_{\pi^+}, \quad \langle 0|\, \bar{s}\gamma_\mu\gamma_5 u \,|\, K^+(p)\,\rangle = ip_\mu F_{K^+},$$

$$\langle 0|\, \bar{s}\gamma_\mu\gamma_5 d \,|\, K^0(p)\,\rangle = ip_\mu F_{K^0}, \tag{6.4}$$

where the normalization here is consistent with the experimental value of $F_{\pi^+} = 130\,\text{MeV}$. We will now discuss the extension of the diagonalization procedure of Chapter 5 which allows us to isolate the FN mass eigenstates, and subsequently extract the weak decay constants.

We begin by constructing lattice correlation functions

$$C_{ff'}^{AP}(t) = \sum_{\vec{x},\vec{y}} \langle \mathcal{A}_f(\vec{y},t)\, \mathcal{P}_{f'}^\dagger(\vec{x},0)\rangle, \quad f,f' = u,d,s, \tag{6.5}$$

where we have chosen to restrict ourselves to the Euclidean-time component of the axial-vector, $\mathcal{A}_f \equiv A_4^f = \bar{q}_f\gamma_4\gamma_5 q_f$. The Wick contractions which allow us to write these correlation functions in terms of quark propagators may be summarized as

$$C_{ff'}^{AP}(t) = \sum_{\vec{x},\vec{y}} \mathrm{Tr}\big[\gamma_4\gamma_5\, S_{f'}(\vec{y},t;\vec{y},t)\,\big]\,\mathrm{Tr}\big[\gamma_5\, S_f(\vec{x},0;\vec{x},0)\,\big]$$

$$- \delta_{ff'}\,\mathrm{Tr}\big[\, S_{f'}(\vec{y},t;\vec{x},0)\,\gamma_4\, S_f(\vec{y},t;\vec{x},0)\,\big]. \tag{6.6}$$

In terms of the spectral decomposition, a very similar calculation to that presented in Section 2.2 yields the useful large-time expression

$$C_{ff'}^{AP}(t) = \sum_{\vec{x},\vec{y}} \langle \mathcal{A}_f(\vec{y},t)\, \mathcal{P}_{f'}^\dagger(\vec{x},0)\rangle \xrightarrow[t\to\infty]{} \sum_{n=1}^{3} \frac{L^3}{2M_n} \langle 0|\mathcal{A}_f|n\rangle\, \langle n|\mathcal{P}_{f'}^\dagger|0\rangle\, e^{-M_n t}, \tag{6.7}$$

where we only consider the three least energetic states here, but in principle we could work with six states as in Equation (5.8). We can use the eigenvectors of the large-time matrix of correlation functions, Equation (6.7), which may be normalized to unity so that

$$\sum_{f'=1}^{3} \langle n|\mathcal{P}_{f'}^\dagger|0\rangle\, [\vec{v}_m]_{f'} = \delta_{nm} \sqrt{\sum_{f=1}^{3} |\langle n|\mathcal{P}_f^\dagger|0\rangle|^2}. \tag{6.8}$$

Applying these eigenvectors to the matrix of correlation functions we can isolate terms in the spectral sum as

$$\sum_{f'=u,d,s} C^{AP}_{ff'}(t)[\vec{v}_m]_{f'} = \sum_{n=1}^{3} \frac{L^3}{2M_n} e^{-M_n t} \langle 0|\mathcal{A}_f|n\rangle \sum_{f'=u,d,s} \langle n|\mathcal{P}^{\dagger}_{f'}|0\rangle [\vec{v}_m]_{f'}$$

$$= \sqrt{\frac{L^3}{2M_m}}\, e^{-M_m t} \langle 0|\mathcal{A}_f|m\rangle \sqrt{\sum_{f'=u,d,s} \frac{L^3}{2M_m} |\langle 0|\mathcal{P}_{f'}|m\rangle|^2}. \tag{6.9}$$

Note that to simplify the presentation we have not included backwards-propagating states, however this will be corrected in our final expressions. The normalized-to-unity eigenvectors $\vec{v}_m$ in Equation (6.8) are obtained from the GEVP of the 3×3 matrix of PS correlation functions, which at large times results in the diagonalization

$$\vec{v}^{\,T}_n\, C^{PP}(t)\, \vec{v}_n = e^{-M_n t} \sum_{f'=u,d,s} \frac{L^3}{2M_n} |\langle 0|\mathcal{P}_{f'}|n\rangle|^2, \tag{6.10}$$

and we have given this matrix of correlation functions the superscript PP to indicate that the operators at source and sink are of the pseudoscalar type $\mathcal{P}_f$.

The matrix elements $\langle 0|\mathcal{A}_f|m\rangle$ are hence extracted from Equation (6.9) as

$$\langle 0|\mathcal{A}_f|m\rangle = \sqrt{\frac{2M_m}{L^3}}\, e^{M_m t} \sum_{f'=u,d,s} C^{AP}_{ff'}(t)[\vec{v}_m]_{f'} \left(\sum_{f''=u,d,s} \frac{L^3}{2M_m} |\langle 0|\mathcal{P}_{f''}|m\rangle|^2 \right)^{-\frac{1}{2}}, \tag{6.11}$$

where we have distributed the constant factors in the above Equation (6.11) for ease of matching to our diagonalized pseudoscalar correlation functions of Equation (6.10).

We can isolate the quark-flavour basis decay constants via the Euclidean time component of the axial-vector current at zero 3-momentum as $\langle 0|\mathcal{A}_f|n\rangle = M_n F^f_n$. Explicitly, in terms of our correlation functions and including the backwards-propagating states on the lattice, we calculate

$$F^f_n = \sqrt{\frac{2}{M_n L^3}} \left(e^{-M_n t} + e^{-(T-t)M_n}\right)^{-1} \frac{\sum_{f'=u,d,s} C^{AP}_{ff'}(t)\, [\vec{v}_n]_{f'}}{\sqrt{\vec{v}^{\,T}_n\, C^{PP}(t)\, \vec{v}_n \, \left(e^{-M_n t} + e^{-(T-t)M_n}\right)^{-1}}}, \tag{6.12}$$

where T is again the full time-extent of the lattice.

We also calculate the decay constants of the remaining nonet mesons at large times as

$$F_{\pi^+} = \sqrt{\frac{2}{M_{\pi^+} L^3}} \left(e^{-M_{\pi^+} t} + e^{-(T-t)M_{\pi^+}}\right)^{-1} \frac{C^{AP}_{\pi^+}(t)}{\sqrt{C^{PP}_{\pi^+}(t) \left(e^{-M_{\pi^+} t} + e^{-(T-t)M_{\pi^+}}\right)^{-1}}}, \tag{6.13}$$

$$F_{K^+} = \sqrt{\frac{2}{M_{K^+} L^3}} \left(e^{-M_{K^+}\, t} \,+\, e^{-(T-t)M_{K^+}}\right)^{-1} \frac{C^{AP}_{K^+}(t)}{\sqrt{C^{PP}_{K^+}(t) \,\left(e^{-M_{K^+}\, t} \,+\, e^{-(T-t)M_{K^+}}\right)^{-1}}}, \tag{6.14}$$

$$F_{K^0} = \sqrt{\frac{2}{M_{K^0} L^3}} \left(e^{-M_{K^0}\, t} \,+\, e^{-(T-t)M_{K^0}}\right)^{-1} \frac{C^{AP}_{K^0}(t)}{\sqrt{C^{PP}_{K^0}(t) \,\left(e^{-M_{K^0}\, t} \,+\, e^{-(T-t)M_{K^0}}\right)^{-1}}}, \tag{6.15}$$

where

$$C^{AP}_{\pi^+}(t) = \sum_{\vec{x},\vec{y}} \langle \mathcal{A}_{\pi^+}(\vec{y},t)\, \mathcal{P}^{\dagger}_{\pi^+}(\vec{x},0)\rangle, \quad C^{PP}_{\pi^+}(t) = \sum_{\vec{x},\vec{y}} \langle \mathcal{P}_{\pi^+}(\vec{y},t)\, \mathcal{P}^{\dagger}_{\pi^+}(\vec{x},0)\rangle \tag{6.16}$$

$$\mathcal{A}_{\pi^+} = \bar{u}\gamma_4\gamma_5 d, \quad \mathcal{P}_{\pi^+} = \bar{u}\gamma_5 d, \tag{6.17}$$

and similarly for the K^+ and K^0.

6.1.2 Renormalisation

To make sensible comparisons between bare lattice results, which implicitly depend on the regulator, and experimental or phenomenological determinations of matrix elements, the interpolating operators must be renormalised in an appropriate scheme (usually $\overline{\text{MS}}$). In this work we utilise the non-perturbative RI'-MOM framework [121, 122], in which one calculates the bare vertex function for an operator non-perturbatively on the lattice before matching to the tree-level result. The literature is primarily concerned with flavour singlet and non-singlet renormalisation factors with full quark-flavour degeneracy, so that only the presence of disconnected contributions to the singlet renormalisation distinguishes the two cases [123]. In this work we are initially faced with the task of extending the process of renormalisation in the RI'-MOM scheme to include non-degenerate quark flavours, which is necessary even in the chiral limit due to QED. The subsequent changing of scheme using continuum perturbation theory to $\overline{\text{MS}}$, for example, is left for future work.

The RI'-MOM scheme

The typical renormalisation of quark-bilinear lattice operators in RI'-MOM is defined multiplicatively [121], however with our non-degenerate quark-flavour operators we must allow for operator mixing which can occur through diagrams such as that illustrated in Figure 6.1. Whilst in principle we may also have gluonic operators contributing to the renormalised quark-flavour operator, for the present study we will only consider the mixing of quark operators as

$$\mathcal{O}^R_f(\mu) = \sum_{f'} Z^{ff'}_{\mathcal{O}}(\mu a)\, \mathcal{O}_{f'}(a), \tag{6.18}$$

with the resulting operator $\mathcal{O}^R_f(\mu)$ being independent of the lattice regularisation scheme. The factors $Z^{ff'}_{\mathcal{O}}$ may be interpreted as a matrix in flavour which acts to

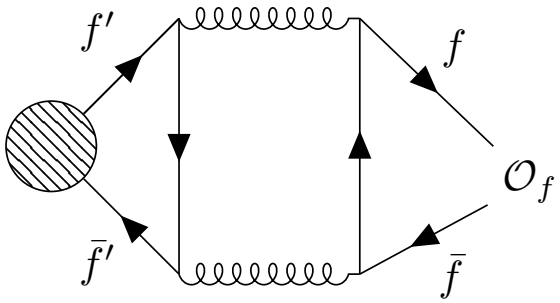

Figure 6.1: A leading-order, $\mathcal{O}(g^4)$, diagram contributing to the operator mixing, where $\mathcal{O}_f$ denotes our quark-flavour operator of flavour f, and the lined circle an external state.

transform the lattice operators to a new renormalisation scheme

$$\begin{bmatrix} \mathcal{O}_u^R(\mu) \\ \mathcal{O}_d^R(\mu) \\ \mathcal{O}_s^R(\mu) \end{bmatrix} = \begin{bmatrix} Z_{\mathcal{O}}^{uu} & Z_{\mathcal{O}}^{ud} & Z_{\mathcal{O}}^{us} \\ Z_{\mathcal{O}}^{du} & Z_{\mathcal{O}}^{dd} & Z_{\mathcal{O}}^{ds} \\ Z_{\mathcal{O}}^{su} & Z_{\mathcal{O}}^{sd} & Z_{\mathcal{O}}^{ss} \end{bmatrix} \begin{bmatrix} \mathcal{O}_u(a) \\ \mathcal{O}_d(a) \\ \mathcal{O}_s(a) \end{bmatrix}. \tag{6.19}$$

Now setting $a = 1$, the determination of the Z-factors above is achieved through non-perturbative calculation of the bare amputated vertex function

$$\Gamma_{ff'}^{\mathcal{O}}(p) = S_{f'}^{-1}(p)\, G_{ff'}^{\mathcal{O}}(p)\, S_{f'}^{-1}(p), \tag{6.20}$$

where f and f' enumerate the three light quark flavours, and the Green's function $G_{ff'}^{\mathcal{O}}$ is given by

$$G_{ff'}^{\mathcal{O}}(p) = \frac{1}{V_4} \sum_{x,y,z} e^{-ip(x-y)} \langle q_{f'}(x)\, \mathcal{O}_f(z)\, \bar{q}_{f'}(y) \rangle. \tag{6.21}$$

The lattice four-volume is denoted V_4 and $S_{f'}^{-1}(p)$ is the inverse of the quark propagator of flavour f', first projected onto momentum p

$$S_{f'}(p) = \frac{1}{V_4} \sum_{x,y} e^{-ip(y-x)}\, S_{f'}(y;x), \tag{6.22}$$

which may in practice be calculated using a momentum source propagator. We can perform Wick contractions on the Green's function, Equation (6.21), explicitly for the axial-vector quark-flavour operators

$$G_{ff'}^{A}(p) = \frac{1}{V_4} \sum_{x,y,z} e^{-ip(x-y)} \left\langle q_{f'}(x)\ (\bar{q}_f(z)\gamma_\mu\gamma_5 q_f(z))\ \bar{q}_{f'}(y) \right\rangle$$

$$= \frac{1}{V_4} \sum_{x,y,z} e^{-ip(x-y)}\ (\delta_{ff'}\, S_f(x;z)\, \gamma_\mu\gamma_5\, S_f(z;y)\ -\ S_{f'}(x;y)\, \mathrm{Tr}\left[S_f(z;z)\gamma_\mu\gamma_5\right]). \tag{6.23}$$

In the above expression we can see the connected contributions occurring only for the flavour diagonal Green's functions ($f = f'$), while the disconnected terms contribute for each flavour combination. Diagrammatic representations for each of these types of contribution are presented in Figure 6.2.

The renormalised amputated vertex function is then defined through application of Equation (6.18),

$$\Gamma^R_{ff'}(p) = \frac{1}{Z_{q_{f'}}} \sum_g Z^{fg}_{\mathcal{O}} \Gamma^{\mathcal{O}}_{gf'}(p), \tag{6.24}$$

where $Z_{q_{f'}}$ denotes the renormalisation factor for the quark field and is given by

$$Z_q(p) = \frac{\mathrm{Tr}\left[-i \sum_\lambda \gamma_\lambda \sin(p_\lambda) S_q^{-1}(p)\right]}{12 \sum_\rho \sin^2(p_\rho)}. \tag{6.25}$$

The condition which is then imposed is to set the renormalised amputated vertex functions equal to their tree-level values in perturbation theory, at the scale $p^2 = \mu^2$, with the tree-level values

$$\Gamma^R_{ff'}(p) = \delta_{ff'} \Gamma^{Born}_{\mathcal{O}}. \tag{6.26}$$

The Born term $\Gamma^{Born}_{\mathcal{O}}$ is the tree-level amputated vertex function and is equal to $\Gamma^{Born}_{A_\mu} = \gamma_5\gamma_\mu \mathbb{I}_{colour}$ for axial-vector operators [124], and in practice we perform the calculation with the 3rd component $\Gamma^{Born}_{A_3} = \gamma_5\gamma_3 \mathbb{I}_{colour}$. We have already seen that for off-diagonal flavour combinations, the only contributions to the amputated vertex function are disconnected, which do not occur at tree-level and hence we have introduced the delta function in Equation (6.26).

Applying the renormalisation condition of Equation (6.26) to Equation (6.24) we find

$$\begin{aligned}
\delta_{f''f'} \Gamma^{Born}_{\mathcal{O}} &= \frac{1}{Z_{q_{f'}}(p)} \sum_g Z^{f''g}_{\mathcal{O}} \Gamma^{\mathcal{O}}_{gf'}(p) \Big|_{p^2=\mu^2} \\
\delta_{f''f'} \, \mathbb{I}_{spin} \, \mathbb{I}_{colour} &= \frac{1}{Z_{q_{f'}}(p)} \sum_g Z^{f''g}_{\mathcal{O}} \Gamma^{\mathcal{O}}_{gf'}(p) (\Gamma^{Born}_{\mathcal{O}})^{-1} \Big|_{p^2=\mu^2} \\
\sum_{f''} \left(Z^{-1}_{\mathcal{O}}\right)^{ff''} \delta_{f''f'} &= \frac{1}{12 Z_{q_{f'}}(p)} \sum_g \delta_{fg} \mathrm{Tr}\left[\Gamma^{\mathcal{O}}_{gf'}(p) (\Gamma^{Born}_{\mathcal{O}})^{-1}\right] \Big|_{p^2=\mu^2} \\
\left(Z^{-1}_{\mathcal{O}}\right)^{ff'} &= \frac{1}{12 Z_{q_{f'}}(p)} \mathrm{Tr}\left[\Gamma^{\mathcal{O}}_{ff'}(p) (\Gamma^{Born}_{\mathcal{O}})^{-1}\right] \Big|_{p^2=\mu^2},
\end{aligned} \tag{6.27}$$

where the indicated trace is over the implicit spin and colour indices, and the resulting quantity $(Z^{-1}_{\mathcal{O}})^{ff'}$ is the (f, f') component of the matrix-inverse of the Z-factors as they appear in Equation (6.19). Note that it is necessary to perform this calculation on the lattice with gauge-fixed fields, although the gauge dependence is not retained in the final result.

Throughout this discussion we have considered only the FN operators, but it is straightforward to calculate the RI'-MOM factors for the remaining flavoured axial-vector operators also. For these currents there can be no closed-loop contributions

Figure 6.2: The two types of vertex function contribution for the flavour-neutral operator $\mathcal{O}_f$; the connected diagram involving only the flavour f (left), and the disconnected diagrams involving a quark-loop of flavour f and through-propagating quark of flavour f'. The connected diagrams enter at tree-level, while the disconnected diagrams have leading strong and electromagnetic contributions at $\mathcal{O}(g^4)$ and $\mathcal{O}(e^4)$ respectively [125].

to the vertex function, and the Green's functions producing the required connected diagrams may be written as

$$G^{F,A}_{ff'}(p) = \frac{1}{V_4}\sum_{x,y,z} e^{-ip(x-y)} \left\langle q_f(x)\ (\bar{q}_f(z)\gamma_\mu\gamma_5 q_{f'}(z))\ \bar{q}_{f'}(y)\right\rangle, \tag{6.28}$$

where we have added the superscript F to differentiate the flavoured operator appearing in the above Green's function to the flavour-neutral operators of the preceding discussion, and A again denotes the axial-vector operator. The appropriate amputation then yields

$$\Gamma^{F,A}_{ff'}(p) = S_f^{-1}(p)\left[\sum_{x,y,z}\frac{e^{-ip(x-y)}}{V_4}\, S_f(x;z)\,\gamma_\mu\gamma_5\, S_{f'}(z;y)\right] S^{-1}_{f'}(p). \tag{6.29}$$

Substituting this amputated vertex function into the procedure already established will then yield the desired Z-factor for the flavoured operator composed of f and f' flavoured quarks,

$$\frac{1}{Z^{ff'}_{F,A}} = \frac{1}{12\sqrt{Z_{q_f} Z_{q_{f'}}}}\mathrm{Tr}\left[\Gamma^{ff'}_{F,A}(p)(\Gamma^{Born}_{F,A})^{-1}\right]\Big|_{p^2=\mu^2}. \tag{6.30}$$

We stress that the above Z-factor is not a matrix, unlike the FN case in Equation (6.27), and the superscript ff' simply labels the flavours of quark appearing in the operator to be renormalised.

In practice, the operator renormalisation factors are calculated at a range of scales (momenta), as it is understood that for sufficiently large momenta the flavoured axial-vector operator renormalisation is independent of scale. For the FN operators the anomalous dimension is non-vanishing so that the renormalisation remains scale dependent, however for the range of momenta we consider we will see that the scale dependence is clearly not resolved at our precision. As a consequence of this we can consider our FN Z-factors to be at a rough scale of $\mu \approx a^{-1}$. Moreover, it is known that there exist discretisation errors in the RI'-MOM renormalisation fac-

tors beginning at $(ap)^2$, and so the Z-factors are extracted by first identifying the scale-independent region and then extrapolating to $(ap)^2 = 0$ in order to minimize discretization errors. We will see in our results that considering only the leading-order discretization errors, $\propto (ap)^2$, gives a very good description of the data.

6.2 Flavour-breaking expansions

It was shown in [126] that decay constants defined through couplings of octet currents to their corresponding octet states, $\langle 0|A^a_\mu|n\rangle$, possess the same symmetries as the masses-squared of those states, and so we can immediately write

$$F_{\pi^+} = F_0 \,+\, H_0^{\rm EM}(e_u^2 + e_d^2 + e_s^2) \,+\, G(\delta m_u + \delta m_d) \,+\, H_2^{\rm EM}(e_u - e_d)^2, \tag{6.31}$$

$$F_{K^+} = F_0 \,+\, H_0^{\rm EM}(e_u^2 + e_d^2 + e_s^2) \,+\, G(\delta m_u + \delta m_s) \,+\, H_2^{\rm EM}(e_u - e_s)^2, \tag{6.32}$$

$$F_{K^0} = F_0 \,+\, H_0^{\rm EM}(e_u^2 + e_d^2 + e_s^2) \,+\, G(\delta m_d + \delta m_s), \tag{6.33}$$

by analogy with Equations (5.22)–(5.24). The correct approach to the mass extrapolation of the FN decay constants is less obvious. Consider decay constants defined through quark-flavour basis (axial-vector) operators coupling to fictitious quark-flavour states, $F_{ff'} = \langle 0|\mathcal{A}_{f'}|f\rangle/M_f$. It would follow then, by analogy with the flavoured octet decay constants above, that these decay constants may be extrapolated using a straightforward generalization of Equation (5.25),

$$\begin{bmatrix} F_{uu} & F_{ud} & F_{us} \\ F_{ud} & F_{dd} & F_{ds} \\ F_{us} & F_{ds} & F_{ss} \end{bmatrix} = \left[F_0 + H_0^{\rm EM}(e_u^2 + e_d^2 + e_s^2)\right] \cdot \mathbb{I} + E \begin{bmatrix} 1 & 1 & 1 \\ 1 & 1 & 1 \\ 1 & 1 & 1 \end{bmatrix}$$

$$+h_0 \begin{bmatrix} 2\delta m_u & \delta m_u + \delta m_d & \delta m_u + \delta m_s \\ \delta m_u + \delta m_d & 2\delta m_d & \delta m_d + \delta m_s \\ \delta m_u + \delta m_s & \delta m_d + \delta m_s & 2\delta m_s \end{bmatrix} + 2H_1^{\rm EM} \begin{bmatrix} e_u^2 & 0 & 0 \\ 0 & e_d^2 & 0 \\ 0 & 0 & e_s^2 \end{bmatrix}$$

$$+2G \begin{bmatrix} \delta m_u & 0 & 0 \\ 0 & \delta m_d & 0 \\ 0 & 0 & \delta m_s \end{bmatrix} + g_1^{\rm EM} \begin{bmatrix} e_u^2 & e_u e_d & e_u e_s \\ e_u e_d & e_d^2 & e_d e_s \\ e_u e_s & e_d e_s & e_s^2 \end{bmatrix}. \tag{6.34}$$

The difference between these hypothetical decay constants and those that we are concerned with herein is a transformation of the quark-flavour basis states into the physical mass eigenstates, which may be performed using the flavour contents discussed in Chapter 5, or equivalent eigenvectors. Our scheme for extrapolating the FN decay constants extracted via Equation (6.12) then, is to first fit the extracted overlaps to the eigenvectors of the mass expansion, Equation (5.25), before fitting

Lattice ensembles			
#	κ_u	κ_d	κ_s
7	0.124362	0.121713	0.121713
8	0.124440	0.121676	0.121676
9	0.124508	0.121821	0.121466

Table 6.1: The number labels and κ-values for the three $V_4 = 32^3 \times 64$ ensembles employed in this chapter. We have continued the ensemble naming convention from Chapter 5 for ease of comparison with results therein.

the decay constants to the expression

$$\begin{bmatrix} F^u_{\pi^0} & F^u_\eta & F^u_{\eta'} \\ F^d_{\pi^0} & F^d_\eta & F^d_{\eta'} \\ F^s_{\pi^0} & F^s_\eta & F^s_{\eta'} \end{bmatrix} = \begin{bmatrix} F_{uu} & F_{ud} & F_{us} \\ F_{ud} & F_{dd} & F_{ds} \\ F_{us} & F_{ds} & F_{ss} \end{bmatrix} \begin{bmatrix} \langle 0|\tilde{\mathcal{O}}_u|\pi^0\rangle & \langle 0|\tilde{\mathcal{O}}_u|\eta\rangle & \langle 0|\tilde{\mathcal{O}}_u|\eta'\rangle \\ \langle 0|\tilde{\mathcal{O}}_d|\pi^0\rangle & \langle 0|\tilde{\mathcal{O}}_d|\eta\rangle & \langle 0|\tilde{\mathcal{O}}_d|\eta'\rangle \\ \langle 0|\tilde{\mathcal{O}}_s|\pi^0\rangle & \langle 0|\tilde{\mathcal{O}}_s|\eta\rangle & \langle 0|\tilde{\mathcal{O}}_s|\eta'\rangle \end{bmatrix}. \quad (6.35)$$

6.3 Results

For the lattice results presented in this chapter we have performed unitary simulations on three different QCD+QED ensembles, two of which possess U-spin symmetry and one with three non-degenerate quarks. We have opted here for larger, $32^3 \times 64$, volumes when compared with the ensembles used in Chapter 5, so as to reduce the impact of finite-volume effects. The κ-values and ensemble labels are given in Table 6.1, and we note in particular that Ensemble 7 has the same approximate SU(3)-symmetric quark masses as Ensemble 1. Moreover, Ensemble 9 exhibits the same quark masses as the unitary $48^3 \times 96$ ensemble employed in Chapter 3.

With our $32^3 \times 64$ volume simulations, we do not presently need to be concerned with the presence of two-photon states at low enough energies to disrupt our spectral decomposition. However, for simulations on larger lattice volumes, one could control the two-photon channels using an extended variational basis, using quark smearings as in Chapter 5 for example.

RI'-MOM results

The RI'-MOM renormalisation Z-factors are determined on Ensemble 7, with an additional neutral Z-factor (connected only) calculated for comparison using partially-quenched quarks, with zero electric charge and hopping parameter $\kappa_n = 0.1208142$. The mass of this neutral quark has been tuned so that $M^2_{n\bar{n}} = X^2_\pi$, in keeping with the scheme of Equation (2.46). For the matrix of FN axial-vector Z-factors, which have disconnected contributions, the quark-loop terms $\mathrm{Tr}\,[S_f(z;z)\gamma_5\gamma_3]$ are calculated using colour- and spin-diluted $\mathbb{Z}_2$ volume-sources with $\mathcal{O}(100)$ independent sources on each gauge configuration. In Figure 6.3 we present our determinations of the flavour-diagonal elements of the Z matrix (LHS), as well as the off-diagonal, purely

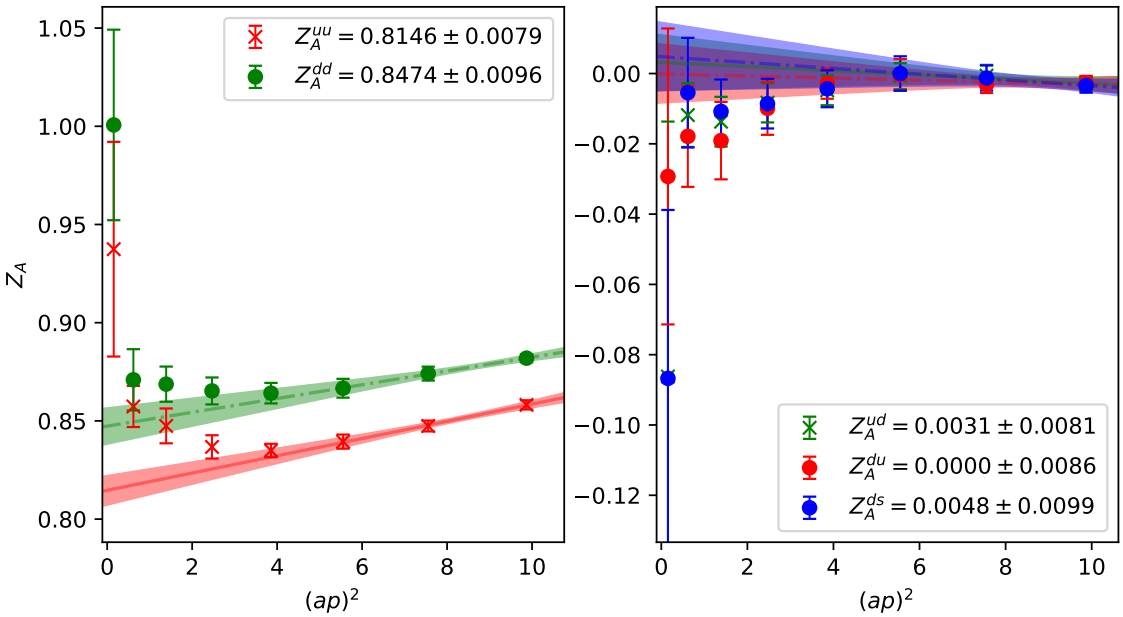

Figure 6.3: The distinct flavour-diagonal (LHS) and off-diagonal (RHS) elements of the axial-vector Z-factor matrix. The flavour-diagonal factors have a large connected contribution and are hence well resolved, whilst the off-diagonals are purely disconnected (see Equation (6.23)).

disconnected elements (RHS). Since the down and strange quarks are degenerate in this simulation, for the FN Z-factors we have $Z_A^{dd} = Z_A^{ss}$, $Z_A^{ds} = Z_A^{sd}$, $Z_A^{ud} = Z_A^{us}$ and $Z_A^{du} = Z_A^{su}$. The signal is well resolved for the flavour-diagonal factors which are dominated by their connected contributions, however the results of our continuum extrapolations for the off-diagonal elements are consistent with zero. Although we cannot resolve the very small and purely disconnected off-diagonal contributions in the continuum, the signals are still seen to exhibit the expected behaviour.

In Figure 6.4 we present the remaining (connected-only) Z-factors which are required for renormalisation of the charged-pion and kaon decay constants, as well as the fictitious neutral Z-factor for comparison. The numbers appearing in the legend in each case correspond to the continuum limit, where the fit is performed on only the four largest momentum values for which the expected $(ap)^2$ scaling is observed.

Decay constant results

As in Chapter 5 we calculate all connected contributions to our correlation functions using the one-end trick, and again utilise three independent $\mathbb{Z}_2$-noise sources per gauge field configuration in calculating both disconnected and connected diagrams. Also in parallel to the method of Chapter 5, we calculate two different levels of gauge-covariant Gaussian smearing, however since we require local axial-vector operators for the decay constant calculation, one of the smearing levels is trivial (not smeared). This is necessary because the same propagators should be used for

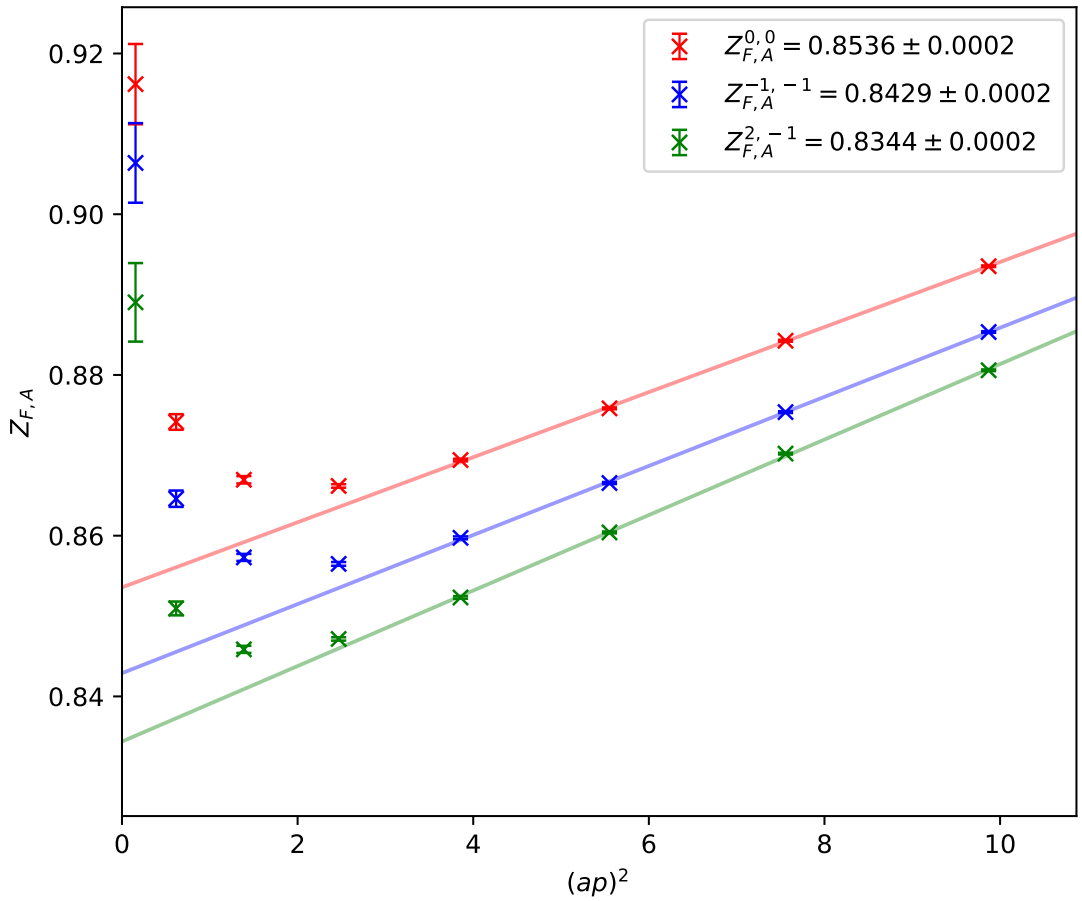

Figure 6.4: The flavoured axial-vector Z-factors which receive only connected contributions, labelled by the electric charges of the quarks in the relevant operator. The factors $Z^{-1,-1}_{F,A}$ and $Z^{2,-1}_{F,A}$ are relevant to the K^0 and π^+/K^+ decay constants respectively, whilst the Z-factor for a fictitious neutral-quark operator is presented to give a sense of the valence charge dependence.

both C^{AP} and C^{PP} to reduce computational cost. The masses and flavour compositions are calculated from the variational analysis with the basis extended in the smearing degree-of-freedom, as in Chapter 5, whilst the subsequent decay constant extraction is performed using only the local operators. The flavour compositions and meson masses for each of the three ensembles 7–9 are listed in Tables 6.2 and 6.3 respectively.

In Figure 6.5 we give an example of the signals obtained for the (non-renormalised) decay constants on our Ensemble 7. The eigenvectors are calculated using the GEVP with $\delta t = 1$, and at both $t_0 = 3$ and $t_0 = 4$, in order to absorb some of the systematic uncertainty associated with the choice of t_0. As can be seen, the η' signal tends to degrade at relatively small values of Euclidean time, forcing us to fit a plateau earlier than for the octet species. It is hence reasonable to assume that our extracted values of the η' decay constants may presently over or underestimate the true values, and this is unlikely to be captured in the quoted uncertainty. The renormalised FN and flavoured decay constants are given in Table 6.4 and Table 6.5 respectively.

The fitting of the quark-mass extrapolation scheme for the decay constants, described in Section 6.2, is performed on the lattice decay constants with the RI'-MOM Z-factors applied according to Equation (6.18),

$$\tilde{F}_n^f \equiv \sum_{f'} Z_A^{ff'} F_n^{f'}. \tag{6.36}$$

The FN decay constant fits are presented in Figure 6.6, and the range of fit parameters in Table 6.6. The overlap fits which are input into the decay constant fit (last factor of Equation (6.35)) are performed on the full set of ensembles 1–9. Since we currently have very few ensembles with which to fit our decay constant quark-mass extrapolation, we consider its current status to be that of a proof-of-concept, and to that end the results appear promising.

The top panel of Figure 6.6 displays the decay constant fit on a quark-mass trajectory with $\delta m_d = 0$, on which our Ensemble 7 results are presented. This panel should be compared with the top panels of Figure 5.5, which share the same trajectory and give relevant behaviour of the mass eigenstates. In the second panel of Figure 6.6 we present the fit along the U-spin trajectory, $\delta m_d = \delta m_s$, as well as the results from our ensembles 7 (right) and 8 (left). This plot may be compared with the second row of plots in Figure 5.5 which again share the same trajectory. The final (bottom) panel of Figure 6.6 gives the fit along the constant-δm_d trajectory which our Ensemble 9 occupies, and which possesses the lightest up and down quarks of any of our ensembles 1–9. It is clear that with our very limited set of ensembles, the mass extrapolation becomes poorly constrained at such large values of SU(3)-flavour breaking as are present in this plot.

In Figure 6.7 we show a close-up view of the flavoured decay constants and their respective fits on each of our ensembles 7–9, normalized by the flavour-singlet quantity $X_{F_\pi} = (F_{\pi^+} + F_{K^+} + F_{K^0})/3$. In the top panel we present the results of ensembles 7–8 which each possess exact U-spin symmetry, and as such one of the

Flavour compositions									
#	$\lvert\langle 0\rvert\tilde{\mathcal{O}}_u\rvert\pi^0\rangle\rvert^2$	$\lvert\langle 0\rvert\tilde{\mathcal{O}}_d\rvert\pi^0\rangle\rvert^2$	$\lvert\langle 0\rvert\tilde{\mathcal{O}}_s\rvert\pi^0\rangle\rvert^2$	$\lvert\langle 0\rvert\tilde{\mathcal{O}}_u\rvert\eta\rangle\rvert^2$	$\lvert\langle 0\rvert\tilde{\mathcal{O}}_d\rvert\eta\rangle\rvert^2$	$\lvert\langle 0\rvert\tilde{\mathcal{O}}_s\rvert\eta\rangle\rvert^2$	$\lvert\langle 0\rvert\tilde{\mathcal{O}}_u\rvert\eta'\rangle\rvert^2$	$\lvert\langle 0\rvert\tilde{\mathcal{O}}_d\rvert\eta'\rangle\rvert^2$	$\lvert\langle 0\rvert\tilde{\mathcal{O}}_s\rvert\eta'\rangle\rvert^2$
7	0.000(0)	0.500(0)	0.500(0)	0.703(5)	0.149(2)	0.149(2)	0.391(25)	0.305(12)	0.305(12)
8	0.737(10)	0.131(5)	0.131(5)	0.000(0)	0.500(0)	0.500(0)	0.362(59)	0.319(29)	0.319(29)
9	0.575(61)	0.423(63)	0.003(3)	0.186(122)	0.231(98)	0.583(61)	0.173(101)	0.247(140)	0.580(137)

Table 6.2: The extracted overlaps squared of the physical states with the flavour basis operators on each of our $32^3 \times 64$ ensembles.

PS meson masses (MeV)							
#	M_{π^0}	M_η	M_η-M_{π^0}	$M_{\eta'}$	M_{π^+}	M_{K^+}	M_{K^0}
7	432(3)	443(4)	15(1)	1185(121)	459(3)	459(3)	432(3)
8	423(8)	460(3)	74(9)	1208(114)	442(3)	442(3)	460(3)
9	309(12)	490(26)	260(18)	1083(109)	341(5)	500(2)	487(2)

Table 6.3: The extracted PS meson masses, as well as the mass-splitting $M_\eta - M_{\pi^0}$, for each of our three $32^3 \times 64$ ensembles.

Flavour-neutral decay constants (MeV)									
#	$\tilde{F}^u_{\pi^0}$	$\tilde{F}^d_{\pi^0}$	$\tilde{F}^s_{\pi^0}$	$\tilde{F}^u_\eta$	$\tilde{F}^d_\eta$	$\tilde{F}^s_\eta$	$\tilde{F}^u_{\eta'}$	$\tilde{F}^d_{\eta'}$	$\tilde{F}^s_{\eta'}$
7	1(1)	100(2)	100(2)	124(3)	56(3)	56(3)	209(7)	191(6)	191(6)
8	126(5)	44(4)	44(4)	1(1)	100(2)	100(2)	190(8)	183(7)	183(7)
9	116(9)	86(8)	6(4)	92(28)	81(17)	115(9)	148(44)	152(46)	237(24)

Table 6.4: The renormalised quark-flavour basis decay constants of the physical states, on each of our $32^3 \times 64$ ensembles in the RI'-MOM scheme.

Flavoured decay constants (MeV)									
#	$\tilde{F}_{\pi^+}$	$\tilde{F}_{K^+}$	$\tilde{F}_{K^0}$	#	$\tilde{F}_{\pi^+}$	$\tilde{F}_{K^+}$	$\tilde{F}_{K^0}$	#	$\tilde{F}_{\pi^+}$	$\tilde{F}_{K^+}$	$\tilde{F}_{K^0}$
7	142(1)	142(1)	140(1)	8	136(2)	136(2)	139(1)	9	132(2)	143(1)	145(1)

Table 6.5: The renormalised flavoured decay constants on each of our $32^3 \times 64$ ensembles in the RI'-MOM scheme.

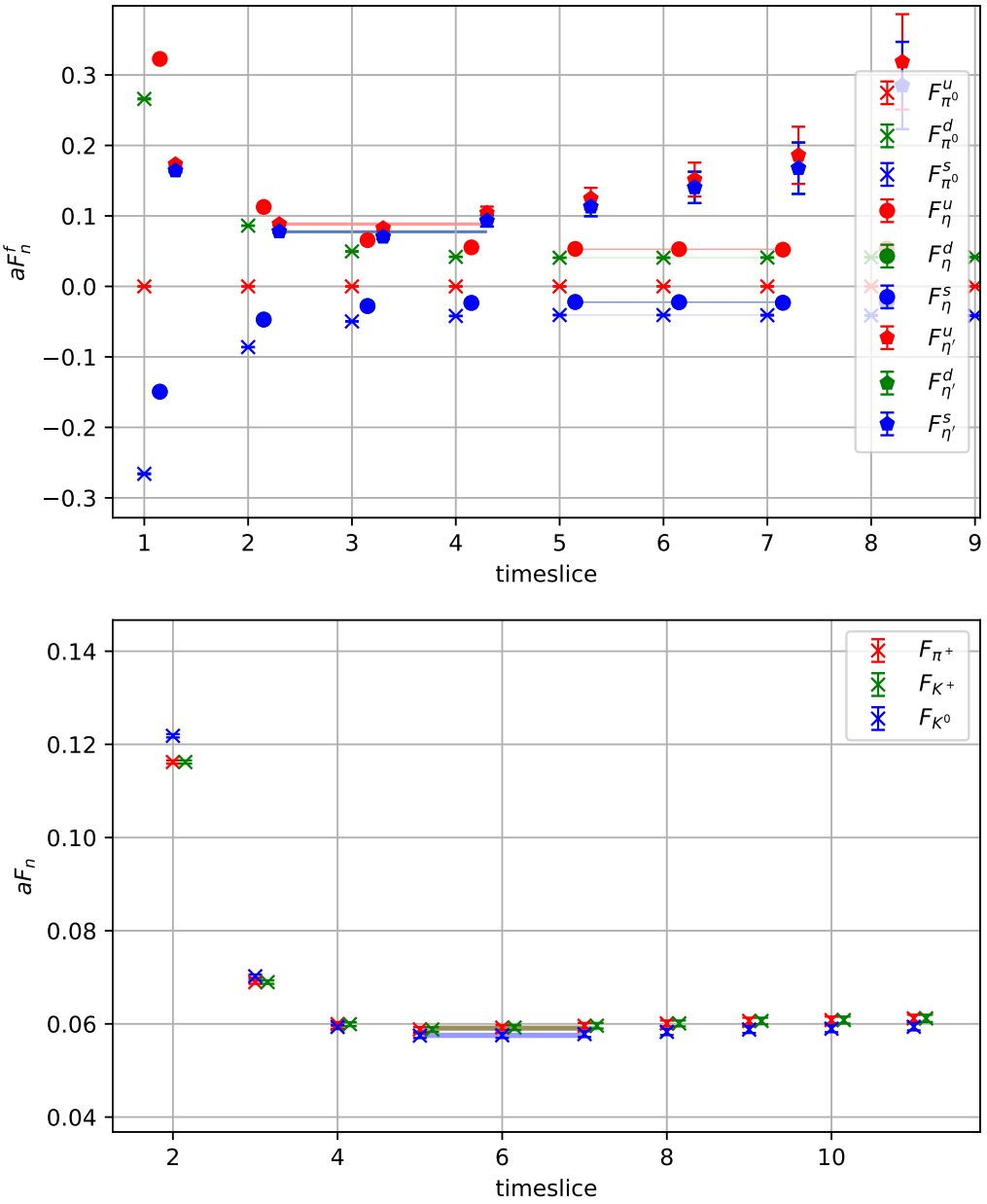

Figure 6.5: The decay constant signals as obtained from Equation (6.12) (top) and Equations (6.13)–(6.15) (bottom) on Ensemble 7. Also pictured are constant fits to the plateau regions in each case.

Decay constants expansion fit parameters						
C	E	G	h_0	g_1^{EM}	H_1^{EM}	H_2^{EM}
0.047(1)	0.019(2)	0.37(18)	0.4(4)	-0.01(1)	0.016(12)	0.001(1)

Table 6.6: We have denoted $C \equiv F_0 + H_0^{\mathrm{EM}}(e_u^2 + e_d^2 + e_s^2)$ for the combination appearing identically in each mass expansion given in Section 5.1.3.

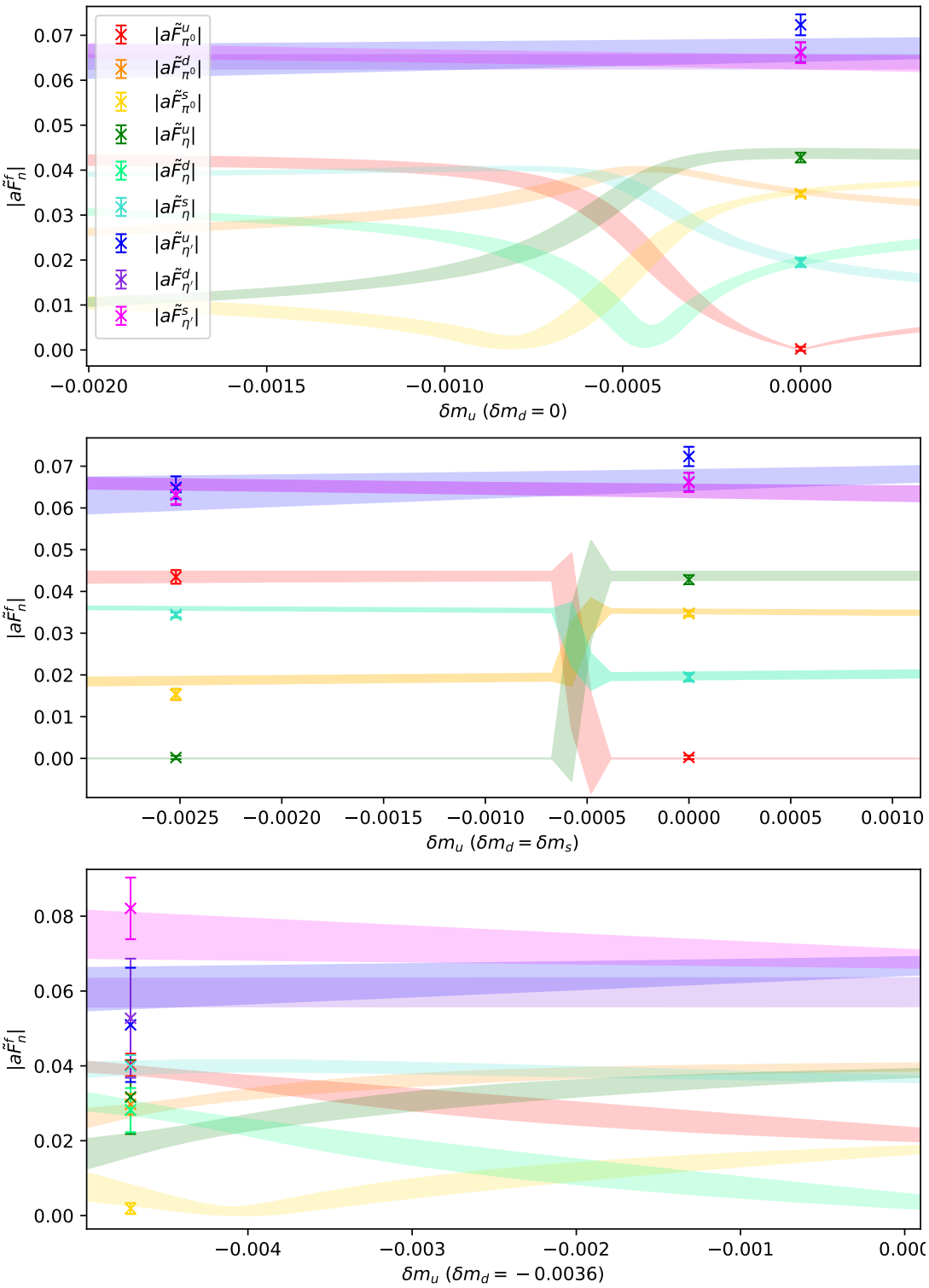

Figure 6.6: The RI'-MOM scheme FN decay constant magnitudes calculated on each of our ensembles 7–9, along with the global fit described in Section 6.2, for $t_0 = 3$. The top panel depicts the results obtained using Ensemble 7 along with the fit on the trajectory $\delta m_d = 0$. The centre panel depicts ensembles 7–8 (right-to-left) along the exact U-spin trajectory. The bottom panel illustrates the fit around, and results of, Ensemble 9, which possesses the greatest broken flavour-symmetry of our ensembles.

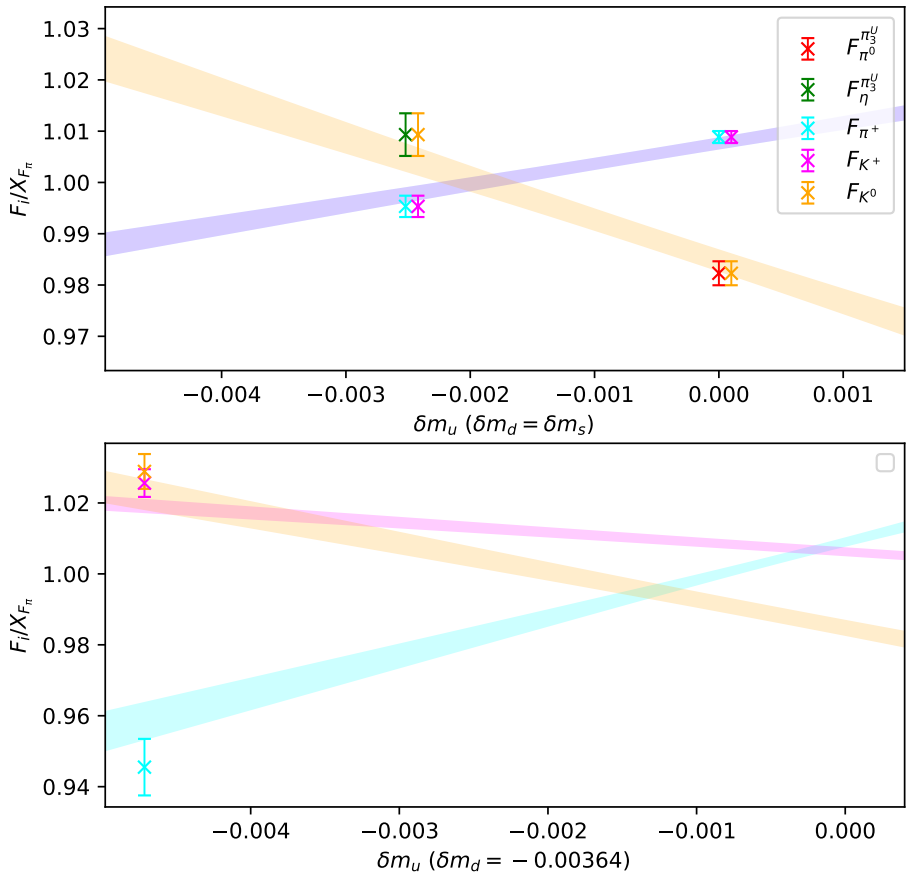

Figure 6.7: The flavoured decay constants and their respective fits on each of our ensembles 7–9 normalized by the singlet quantity X_{F_π}. The top panel depicts the results of ensembles 7–8 (right-to-left) along the U-spin trajectory, as well as the FN decay constants $F_{\pi^0}^{\pi_3^U}$ and $F_\eta^{\pi_3^U}$ on ensembles 7 and 8 respectively, which are predicted and seen to agree with F_{K^0}. The bottom panel depicts the results of Ensemble 9 and the flavoured decay constant fits around it.

Preliminary physical-point decay constants (MeV)					
	$a = \pi_3$	$a = \eta_8$	$a = \eta_1$		
$\tilde{F}^a_{\pi^0}$	99(21)	-36(34)	37(32)	$\tilde{F}_{\pi^+}$	119(9)
$\tilde{F}^a_{\eta}$	-10(17)	99(32)	67(35)	$\tilde{F}_{K^+}$	146(6)
$\tilde{F}^a_{\eta'}$	-1(1)	-103(56)	312(16)	$\tilde{F}_{K^0}$	146(7)

Table 6.7: The values of the decay constant fits at the physical-point quark masses in the RI'-MOM scheme, at the approximate scale $\mu \approx a^{-1}$. The quoted uncertainties are statistical only.

FN eigenstates possesses the flavour composition of a $\pi_3^U = (\bar{d}d - \bar{s}s)/\sqrt{2}$ in each case. For Ensemble 7 (8) the π^0 (η) is an exact π_3^U, and we remind the reader that the labelling of states is done according to the mass hierarchy. The leading-order quark mass/charge flavour-breaking expansion for a pure π_3^U decay constant is

$$F_{\pi_3^U} = F_0 + H_0^{\mathrm{EM}}(e_u^2 + e_d^2 + e_s^2) + G(\delta m_d + \delta m_s), \tag{6.37}$$

which matches identically the expansion for F_{K^0}, Equation (6.33), and we have hence included $F_{\pi^0}^{\pi_3^U} = (F_{\pi^0}^d - F_{\pi^0}^s)/\sqrt{2}$ and $F_{\eta}^{\pi_3^U} = (F_{\eta}^d - F_{\eta}^s)/\sqrt{2}$ from Ensemble 7 and 8 respectively, to show numerical agreement with F_{K^0}. For completeness, the bottom panel of Figure 6.7 shows the flavoured decay constants of Ensemble 9 and the corresponding flavour-breaking expansions along the trajectory $\delta m_d = -0.00364$.

It is clear from the bottom panel of Figure 6.6 that the physical point determination of the FN decay constants from our current global fit should be considered exploratory, where improved precision on Ensemble 9 and/or additional ensembles should greatly improve the current situation. Regardless, it is still of interest to make such an assessment, and to that end we present the values of our fits at the physical point determined for $32^3 \times 64$ volume [65],

$$a\delta m_u^\star = -0.00834(8), \quad a\delta m_d^\star = -0.00776(7). \tag{6.38}$$

Since isospin is a good approximate symmetry at the physical point, it is most intuitive to present the physical point determination in the (isospin) octet-singlet basis, and so with the RI'-MOM renormalisation factors considered we have

$$\tilde{F}_n^{\pi_3} = \frac{1}{\sqrt{2}}\left(\tilde{F}_n^u - \tilde{F}_n^d\right), \quad \tilde{F}_n^{\eta_8} = \frac{1}{\sqrt{6}}\left(\tilde{F}_n^u + \tilde{F}_n^d - 2\tilde{F}_n^s\right), \tag{6.39}$$

$$\tilde{F}_n^{\eta_1} = \frac{1}{\sqrt{3}}\left(\tilde{F}_n^u + \tilde{F}_n^d + \tilde{F}_n^s\right), \tag{6.40}$$

for each $n \in [\pi^0, \eta, \eta']$. Moreover, as in chapters previous, we have scaled all expansion parameters which originate with QED by the factor $\alpha_{\mathrm{QED}}^\star/\alpha_{\mathrm{QED}} = 0.07338$, to approximately correct for our unphysical EM coupling. Unfortunately, since we have no simulations for varying quark charges, we cannot properly constrain the shared

H_0^{EM} term, and so some residual larger-than-physical QED effect will remain. The FN physical-point results, as well as those for the flavoured decay constants, are given in Table 6.7.

As we found in Chapter 5 for the state compositions, which inform the decay constants presented here via Equation (6.34), our preliminary physical-point results for the FN decay constants are consistent with isospin symmetry. The result for $\tilde{F}_{\pi^+} = 119(9)$ may be compared with the charged pion value inferred from experiment $F^{\star}_{\pi^+} = 130\,\mathrm{MeV}$, which shows fair agreement at the current, low level of precision. Additionally, we see agreement in the kaon decay constants at 2σ (statistical) with the experimental value of $F^{\star}_{K^+} = 156(1)\,\mathrm{MeV}$, and it should be noted that the quoted uncertainties underestimate the systematic uncertainties present due to discretization and the finite volume, which have not been studied here.

Considering now the η–η' decay constant sector in isolation, we can compare our results with some existing determinations. As an example we take the results of the recent lattice study [88] at $\mu = 2\,\mathrm{GeV}$, distinguished as $\hat{F}^a_n$, which have central values[1]

$$\hat{F}_{\eta}^{\eta_8} = 149\,\mathrm{MeV}, \quad \hat{F}_{\eta}^{\eta_1} = 16\,\mathrm{MeV},$$
$$\hat{F}_{\eta'}^{\eta_8} = -63\,\mathrm{MeV}, \quad \hat{F}_{\eta'}^{\eta_1} = 143\,\mathrm{MeV}.$$

The associated uncertainties are all $\mathcal{O}(10\%)$, and we note that these results were obtained assuming isospin symmetry and without QED. Comparing these numbers with the relevant results of Table 6.7 we see general agreement at ≈ 1–2σ, except in the case of $\tilde{F}_{\eta'}^{\eta_1}$, for which our result is roughly twice as large as $\hat{F}_{\eta'}^{\eta_1}$. It is likely that our systematic inability to accurately determine the true values of the decay constants associated with the η' account for much of this disagreement. In addition, it is possible that better constraining our extrapolation with simulations at additional quark masses will help to bring these results into agreement. It should be noted also that the results of [88] include corrections of the systematic effects of the finite volume and lattice spacing.

6.4 Summary

In this chapter we have used the theoretical and numerical machinery developed throughout the previous three chapters to extract the weak decay constants of the FN and flavoured PS mesons. We have also introduced and presented preliminary results for the extension to the RI'-MOM renormalisation scheme which facilitates a proper treatment of the renormalisation of FN axial-vector currents on the lattice.

We have deduced quark-mass and charge expansions for the PS meson decay constants, finding that proper parametrisation of the FN sector requires knowledge of the relevant underlying PS flavour-compositions. These parametrisations facilitate physical-point determinations of the PS decay constants which, with improved

[1] Note that the normalization used therein is consistent with $F^{\pi_3}_{\pi^0} \approx 92\,\mathrm{MeV}$, which we have adjusted for by including the relevant factors of $\sqrt{2}$.

precision, may be used as numerical inputs for theoretical and phenomenological calculations regarding various decays which include PS mesons, such as $\pi^0/\eta/\eta' \to \gamma\gamma$ for example.

Through the results of this chapter we have demonstrated a process by which precision physical-point determinations of all PS meson decay constants should be possible. The most immediate improvement of our results would be given by additional lattice simulations at a variety of bare quark masses, however for a precision study one would also desire infinite volume and continuum extrapolations, as well as a careful treatment of the scale dependence of the FN operators.

Chapter 7

Conclusion

The status of lattice QCD studies of many hadron properties have reached a point of precision at which strong isospin symmetry-breaking and QED effects need be considered for further improvement. Whilst naively the inclusion of non-degenerate up and down quarks in lattice QCD is simply an additional computational expense, there are cases, which have been the focus of this thesis, where the breaking of SU(3)-flavour symmetry complicates the role of the canonical basis of hadron interpolating operators through mixing. Moreover, this induced state mixing influences quark-mass extrapolation schemes for hadron properties which, even with more lattice simulations being performed with physical quark masses, can shed light on properties of the underlying quarks. Additionally, the inclusion of QED on the lattice necessitates a careful treatment of flavour-symmetry breaking if the light quarks are endowed with their physical, non-degenerate electric charges. In Chapter 2 we detailed our computational framework for calculating hadronic correlation functions in lattice QCD with three independent flavours of light quark, as well as the inclusion of QED.

In Chapter 3 we investigated the state mixing of the Σ^0–Λ sector of the baryon octet, an effect that may be attributed to broken isospin-symmetry and which is driven by the non-degenerate masses and charges of the up and down quarks. We found therein that Taylor expanding the correlation functions and forming an explicit expression for the mixing angle gave us an interesting insight into the time dependence of the quantity on the lattice, namely the leading-order time independence for QCD-only mixing, and retained time dependence for the case of QCD with QED. Using our derived quark mass and charge parametrisation we were able to make preliminary physical point determinations of $\theta_{\Sigma\Lambda,\text{QCD-only}} = -0.55(3)^\circ$ and $\theta_{\Sigma\Lambda,\text{QCD+QED}} = -1.0(3)$, indicating that QED could contribute around 50% of the total mixing.

For the purpose of studying lattice correlation functions of flavour-neutral operators, which have contributions from disconnected quark-loop diagrams, we investigated the lattice computation of all-to-all quark propagators in Chapter 4. The focus of this investigation was approximation using stochastic $\mathbb{Z}_2$ sources, and we discussed various methods for improving the approximation such as dilution, quark smearing and explicit calculation of the low-lying eigenmodes. From the work therein we selected a combination of spin–colour–time dilution, quark smearing, and three

independent $\mathbb{Z}_2$ sources (per gauge field configuration) for the lattice simulations of the subsequent chapters.

In Chapter 5 we used a very similar process to that developed in Chapter 3, and employed the numerical techniques of Chapter 4, to study mixing in the pseudoscalar meson π^0–η–η' system, as well as the masses of all pseudoscalar octet meson species, in lattice QCD+QED. We presented leading-order flavour-breaking expansions for the flavour-neutral meson masses and flavour compositions which were shown to perform well near an approximate SU(3) symmetric point. The flavour-singlet η' is permitted to mix with the octet η meson even in the isospin limit provided that full SU(3)-flavour symmetry is not realised, and we have obtained a preliminary estimate of $|\theta_{\eta\eta'}| = (-15.1^{+5.9}_{-6})^\circ$, since we do not presently resolve isospin-breaking at the physical point using our extrapolation.

Proceeding naturally from the work of Chapter 5, the focus of Chapter 6 was the calculation of the pseudoscalar meson decay constants for which the state compositions had been determined in Chapter 5. Renormalisation of the axial-vector operators used therein, both flavoured and flavour-neutral, in the RI'-MOM scheme was performed with a treatment for non-degenerate flavours introduced for the first time, necessitated by the presence of QED in our simulations. Again, flavour-breaking expansions were derived for all pseudoscalar decay constants, and in particular the flavour-neutral decay constant parametrisations were found to require simultaneous parametrisation of the state compositions, as determined in the preceding chapter. Our preliminary physical point results were consistent with existing (isospin-conserving) results except for the η', for which our decay constants are significantly larger than other recent determinations, likely due to excited-state contamination.

Overall, we have provided significant proof-of-concept results for state mixing and related quantities with regard to isospin breaking and QED on the lattice. In particular, a precision calculation following the methods of Chapter 6, with additional simulations at a range of light quark masses, should be expected to produce, for example, a resolved determination of the splitting between the π^+ and π^0 decay constants for the first time. Moreover, precision determinations of all pseudoscalar decay constants determined in this way would serve as important inputs to phenomenological calculations of various decays in this sector.

Appendix A

Hadrons in the Eightfold Way

Throughout this thesis we make repeated reference to the belonging of particular hadrons to flavour octet and singlet representations as per the Eightfold Way, which was first introduced in Chapter 1. The Eightfold Way, as utilized herein, is based on identification of the up, down and strange quarks with an approximate SU(3) symmetry, SU(3)-flavour symmetry, and subsequent enumeration of irreducible representations arising as products of fundamental representations.

The light quarks are posited as a triplet, transforming under the fundamental representation which we denote **3**, for which the canonical choice of SU(3) generators given by Gell-Mann (fundamental rep.) are $T_a = \lambda_a/2$, where λ_a are the Gell-Mann matrices

$$\lambda_1 = \begin{bmatrix} 0 & 1 & 0 \\ 1 & 0 & 0 \\ 0 & 0 & 0 \end{bmatrix}, \quad \lambda_2 = \begin{bmatrix} 0 & -i & 0 \\ i & 0 & 0 \\ 0 & 0 & 0 \end{bmatrix}, \quad \lambda_3 = \begin{bmatrix} 1 & 0 & 0 \\ 0 & -1 & 0 \\ 0 & 0 & 0 \end{bmatrix},$$

$$\lambda_4 = \begin{bmatrix} 0 & 0 & 1 \\ 0 & 0 & 0 \\ 1 & 0 & 0 \end{bmatrix}, \quad \lambda_5 = \begin{bmatrix} 0 & 0 & -i \\ 0 & 0 & 0 \\ i & 0 & 0 \end{bmatrix}, \quad \lambda_6 = \begin{bmatrix} 0 & 0 & 0 \\ 0 & 0 & 1 \\ 0 & 1 & 0 \end{bmatrix},$$

$$\lambda_7 = \begin{bmatrix} 0 & 0 & 0 \\ 0 & 0 & -i \\ 0 & i & 0 \end{bmatrix}, \quad \lambda_8 = \frac{1}{\sqrt{3}} \begin{bmatrix} 1 & 0 & 0 \\ 0 & 1 & 0 \\ 0 & 0 & -2 \end{bmatrix}.$$

Similarly, the triplet of light antiquarks transforms under the complex conjugate fundamental representation, which is denoted $\bar{\mathbf{3}}$.

Mesons are composed of a valence quark and antiquark pair, and the resultant representations in the Eightfold Way may be calculated from the product of their respective fundamental representations,

$$\mathbf{3} \otimes \bar{\mathbf{3}} = \mathbf{1} \oplus \mathbf{8},$$

where **1** is the trivial singlet, and **8** the adjoint, or octet, irreducible representation. In order to determine the states transforming under these singlet and octet

representations, we must take a maximal subset of mutually commuting generators known as the Cartan subalgebra [73], for which the canonical choice is $\{T_3, T_8\}$. For the triplet of quarks $[u, d, s]^T$, this choice (namely, T_3) is the familiar strong isotopic spin, or isospin, and is a natural choice due to the near-degeneracy of the up and down quarks. However, as is discussed throughout this thesis and particularly in Chapter 3, the choice of isospin is not unique, and is in fact directly analogous to the (arbitrary) choice to label spin states by their z-component of spin, instead of x or y. In the isospin-centric construction then, the flavour states of the singlet and octet meson representations, labelled by the corresponding pseudoscalar meson, are enumerated as

8 :

$$\pi^+ : |\bar{d}u\rangle, \quad \pi^- : |\bar{u}d\rangle, \quad \pi^0 : \frac{1}{\sqrt{2}}\left(|\bar{u}u\rangle - |\bar{d}d\rangle\right), \quad \eta : \frac{1}{\sqrt{6}}\left(|\bar{u}u\rangle + |\bar{d}d\rangle - 2|\bar{s}s\rangle\right),$$
$$K^0 : |\bar{s}d\rangle, \quad K^+ : |\bar{s}u\rangle, \quad K^- : |\bar{u}s\rangle, \quad \bar{K}^0 : |\bar{d}s\rangle,$$

1 :

$$\eta' : \frac{1}{\sqrt{3}}\left(|\bar{u}u\rangle + |\bar{d}d\rangle + |\bar{s}s\rangle\right).$$

Note that although we have associated these flavour combinations with the pseudoscalar mesons, which are the least massive, the spin-1 vector mesons may considered in the same way.

A similar treatment of the low-lying baryons, composed of three quarks (or three antiquarks), proceeds with some added complexities as

$$\mathbf{3} \otimes \mathbf{3} \otimes \mathbf{3} = \mathbf{1}_A \oplus \mathbf{8}_M \oplus \mathbf{8}_M \oplus \mathbf{10}_S,$$

where the subscripts A, M and S indicate the antisymmetric, mixed symmetry and symmetric natures of the representations under the interchange of two quarks. The association of these representations with physical baryons requires additional considerations such as orbital angular momentum, and is given in detail in [62], but for our purposes herein we presently enumerate the flavour structure of the spin-1/2 baryon octet which is relevant to Chapter 3,

$$n : |udd\rangle, \quad p : |uud\rangle, \quad \Sigma^+ : |uus\rangle, \quad \Sigma^- : |dds\rangle, \quad \Xi^0 : |ssu\rangle, \quad \Xi^- : |ssd\rangle.$$

The flavour compositions of the remaining members of the octet, Σ^0 and Λ, are the subject of Chapter 3, and in the exact SU(3)-flavour approximation are given by combinations of u, d and s, with opposite symmetries under the interchange $u \leftrightarrow d$.

In Figure A.1 we present a diagrammatic representation of the pseudoscalar meson (top) and spin-1/2 baryon (bottom) octets, with strangeness, electric charge and third-component of isospin axes illustrated.

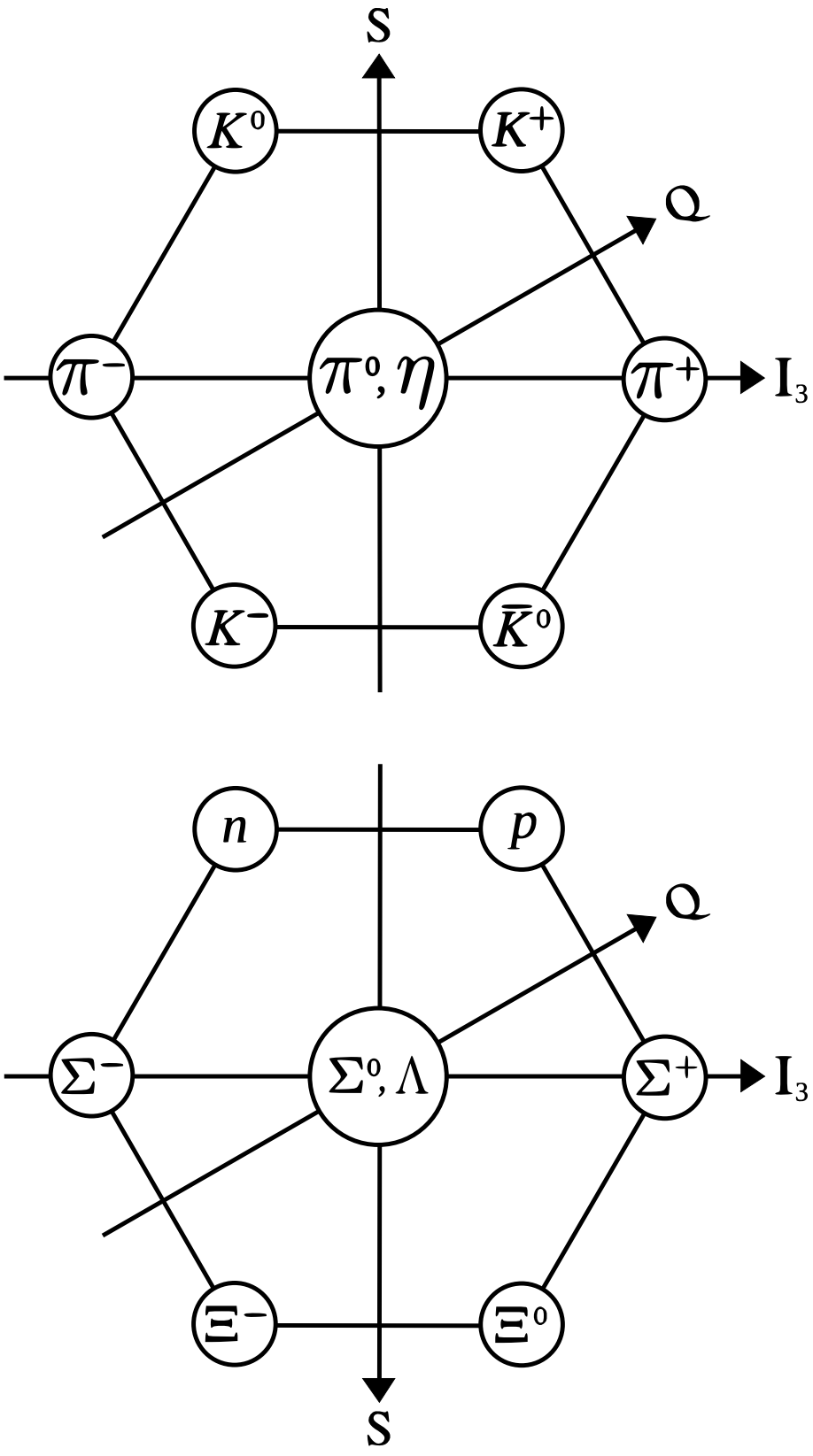

Figure A.1: The pseudoscalar meson octet (top), and spin-1/2 baryon octet (bottom), as originally conceived in the Eightfold Way. The arrows labelled I_3, Q and S indicate the increase of the third component of isospin, electric charge and strangeness respectively.

Appendix B

Discretised integral formulae

We will here list the discrete analogues of some common continuum integral formulae which have been used in this thesis, particularly in the spectral decompositions of lattice correlation functions.

Position and momentum integrals:

$$\int d^4x \longrightarrow \sum_x a^4, \tag{B.1}$$

$$\int d^3\vec{p} \longrightarrow \sum_{\vec{p}} \left(\frac{2\pi}{L}\right)^3, \tag{B.2}$$

and similarly for the 4th-component of momentum, although typically the extent of the lattice in the Euclidean time direction differs from the (dimensionful) spatial extent L.

Dirac delta function:

$$\delta^3(\,\vec{p}\,) = \left(\frac{a}{2\pi}\right)^3 \sum_{\vec{x}} e^{i\vec{p}\cdot\vec{x}}, \tag{B.3}$$

$$\sum_{\vec{p}} \left(\frac{2\pi}{L}\right)^3 \delta^3(\,\vec{k}-\vec{p}\,)\, F(\vec{p}) = F(\vec{k}), \tag{B.4}$$

$$\delta^3(\,\vec{0}\,) = \left(\frac{L}{2\pi}\right)^3. \tag{B.5}$$

Complete set of single-particle momentum states:

$$\mathbb{I} = \sum_n \sum_{\vec{p}} \left(\frac{1}{L}\right)^3 \big|n(\vec{p})\big\rangle \frac{1}{2\,E_{n,\vec{p}}} \big\langle n(\vec{p})\big|. \tag{B.6}$$

Bibliography

[1] E. Rutherford. The scattering of alpha and beta particles by matter and the structure of the atom. *Phil. Mag. Ser. 6*, 21:669–688, 1911.

[2] J. Chadwick. Possible Existence of a Neutron. *Nature*, 129:312, 1932.

[3] J. Chadwick. The Existence of a Neutron. *Proc. Roy. Soc. Lond. A*, 136(830):692–708, 1932.

[4] Hideki Yukawa. On the Interaction of Elementary Particles I. *Proc. Phys. Math. Soc. Jap.*, 17:48–57, 1935.

[5] S. H. Neddermeyer and C. D. Anderson. Note on the Nature of Cosmic Ray Particles. *Phys. Rev.*, 51:884–886, 1937.

[6] J. C. Street and E. C. Stevenson. New Evidence for the Existence of a Particle of Mass Intermediate Between the Proton and Electron. *Phys. Rev.*, 52:1003–1004, 1937.

[7] O. Chamberlain, E. Segre, C. Wiegand, and T. Ypsilantis. Observation of Anti-protons. *Phys. Rev.*, 100:947–950, 1955.

[8] B. Cork, G. R. Lambertson, O. Piccioni, and W. A. Wenzel. Anti-neutrons Produced From Anti-protons in Charge Exchange Collisions. *Phys. Rev.*, 104:1193–1197, 1957.

[9] G. D. Rochester and C. C. Butler. Evidence for the Existence of New Unstable Elementary Particles. *Nature*, 160:855–857, 1947.

[10] David Griffiths. *Introduction to elementary particles*. 2008.

[11] E. C. G. Stueckelberg. Interaction energy in electrodynamics and in the field theory of nuclear forces. *Helv. Phys. Acta*, 11:225–244, 1938.

[12] A. Pais. Some Remarks on the V-Particles. *Phys. Rev.*, 86:663–672, 1952.

[13] M. Gell-Mann. Isotopic Spin and New Unstable Particles. *Phys. Rev.*, 92:833–834, 1953.

[14] T. Nakano and K. Nishijima. Charge Independence for V-particles. *Prog. Theor. Phys.*, 10:581–582, 1953.

[15] M. Gell-Mann. The interpretation of the new particles as displaced charge multiplets. *Nuovo Cim.*, 4(S2):848–866, 1956.

[16] Murray Gell-Mann. The Eightfold Way: A Theory of strong interaction symmetry. 1961.

[17] Murray Gell-Mann and Yuval Ne'eman. The Eightfold way: a review with a collection of reprints. 9 1964.

[18] V. E. Barnes et al. Observation of a Hyperon with Strangeness Minus Three. *Phys. Rev. Lett.*, 12:204–206, 1964.

[19] Murray Gell-Mann. A Schematic Model of Baryons and Mesons. *Phys. Lett.*, 8:214–215, 1964.

[20] O. W. Greenberg. Spin and Unitary Spin Independence in a Paraquark Model of Baryons and Mesons. *Phys. Rev. Lett.*, 13:598–602, 1964.

[21] M. Y. Han and Yoichiro Nambu. Three Triplet Model with Double SU(3) Symmetry. *Phys. Rev.*, 139:B1006–B1010, 1965.

[22] Martin Breidenbach, Jerome I. Friedman, Henry W. Kendall, Elliott D. Bloom, D. H. Coward, H. C. DeStaebler, J. Drees, Luke W. Mo, and Richard E. Taylor. Observed behavior of highly inelastic electron-proton scattering. *Phys. Rev. Lett.*, 23:935–939, 1969.

[23] Elliott D. Bloom et al. High-Energy Inelastic e p Scattering at 6-Degrees and 10-Degrees. *Phys. Rev. Lett.*, 23:930–934, 1969.

[24] J. J. Aubert et al. Experimental Observation of a Heavy Particle *J*. *Phys. Rev. Lett.*, 33:1404–1406, 1974.

[25] J. E. Augustin et al. Discovery of a Narrow Resonance in e^+e^- Annihilation. *Phys. Rev. Lett.*, 33:1406–1408, 1974.

[26] J. D. Bjorken and S. L. Glashow. Elementary Particles and SU(4). *Phys. Lett.*, 11:255–257, 1964.

[27] Chen-Ning Yang and Robert L. Mills. Conservation of Isotopic Spin and Isotopic Gauge Invariance. *Phys. Rev.*, 96:191–195, 1954.

[28] H. Fritzsch, Murray Gell-Mann, and H. Leutwyler. Advantages of the Color Octet Gluon Picture. *Phys. Lett. B*, 47:365–368, 1973.

[29] David J. Gross and Frank Wilczek. Ultraviolet Behavior of Nonabelian Gauge Theories. *Phys. Rev. Lett.*, 30:1343–1346, 1973.

[30] H. David Politzer. Reliable Perturbative Results for Strong Interactions? *Phys. Rev. Lett.*, 30:1346–1349, 1973.

[31] Kenneth G. Wilson. Confinement of Quarks. *Phys. Rev. D*, 10:2445–2459, 1974.

[32] Kenneth G. Wilson. QUARK CONFINEMENT AND LATTICE CALCULATION. *AIP Conf. Proc.*, 48:9–16, 2008.

[33] Johann Haidenbauer, Ulf-G. Meißner, and Andreas Nogga. Constraints on the Λ-Neutron Interaction from Charge Symmetry Breaking in the ${}^{\mathbf{4}}_{\mathbf{\Lambda}}$He - ${}^{\mathbf{4}}_{\mathbf{\Lambda}}$H Hypernuclei. *Few Body Syst.*, 62(4):105, 2021.

[34] R. H. Dalitz and F. Von Hippel. Electromagnetic Λ-Σ^0 mixing and charge symmetry for the Λ-hyperon. *Phys. Lett.*, 10:153–157, 1964.

[35] J. Gasser and H. Leutwyler. Quark masses. *Physics Reports*, 87(3):77 – 169, 1982.

[36] R. Horsley, J. Najjar, Y. Nakamura, H. Perlt, D. Pleiter, P. E. L. Rakow, G. Schierholz, A. Schiller, H. Stüben, and J. M. Zanotti. Lattice determination of Sigma-Lambda mixing. *Phys. Rev.*, D91(7):074512, 2015.

[37] N.H. Christ, C. Dawson, T. Izubuchi, C. Jung, Q. Liu, R.D. Mawhinney, C.T. Sachrajda, A. Soni, and R. Zhou. The η and η' mesons from Lattice QCD. *Phys. Rev. Lett.*, 105:241601, 2010.

[38] Jozef J. Dudek, Robert G. Edwards, Balint Joo, Michael J. Peardon, David G. Richards, and Christopher E. Thomas. Isoscalar meson spectroscopy from lattice QCD. *Phys. Rev.*, D83:111502(R), 2011.

[39] Chris Michael, Konstantin Ottnad, and Carsten Urbach. η and η' mixing from Lattice QCD. *Phys. Rev. Lett.*, 111(18):181602, 2013.

[40] Liping Gan, Bastian Kubis, Emilie Passemar, and Sean Tulin. Precision tests of fundamental physics with η and η' mesons. 7 2020.

[41] A. Bazavov et al. Determination of $|V_{us}|$ from a Lattice-QCD Calculation of the $K \to \pi\ell\nu$ Semileptonic Form Factor with Physical Quark Masses. *Phys. Rev. Lett.*, 112(11):112001, 2014.

[42] Enrico Rinaldi, Sergey Syritsyn, Michael L. Wagman, Michael I. Buchoff, Chris Schroeder, and Joseph Wasem. Lattice QCD determination of neutron-antineutron matrix elements with physical quark masses. *Phys. Rev. D*, 99(7):074510, 2019.

[43] S. Zafeiropoulos, P. Boucaud, F. De Soto, J. Rodríguez-Quintero, and J. Segovia. Strong Running Coupling from the Gauge Sector of Domain Wall Lattice QCD with Physical Quark Masses. *Phys. Rev. Lett.*, 122(16):162002, 2019.

[44] P. A. Boyle, F. Erben, J. M. Flynn, V. Gülpers, R. C. Hill, R. Hodgson, A. Jüttner, F. Ó. hÓgáin, A. Portelli, and C. T. Sachrajda. Simulating rare kaon decays $K^+ \to \pi^+\ell^+\ell^-$ using domain wall lattice QCD with physical light quark masses. 2 2022.

[45] Richard Phillips Feynman. *The principle of least action in quantum mechanics.* PhD thesis, Princeton U., 1942.

[46] Heinz J. Rothe. *Lattice Gauge Theories : An Introduction (Fourth Edition)*, volume 43. World Scientific Publishing Company, 2012.

[47] Steven Weinberg. *The Quantum theory of fields. Vol. 1: Foundations.* Cambridge University Press, 6 2005.

[48] G. P. Lepage. Lattice QCD for novices. In *Strong interactions at low and intermediate energies. Proceedings, 13th Annual Hampton University Graduate Studies, HUGS'98, Newport News, USA, May 26-June 12, 1998*, pages 49–90, 1998.

[49] S. Duane, A. D. Kennedy, B. J. Pendleton, and D. Roweth. Hybrid Monte Carlo. *Phys. Lett. B*, 195:216–222, 1987.

[50] N. Cundy et al. Non-perturbative improvement of stout-smeared three flavour clover fermions. *Phys. Rev.*, D79:094507, 2009.

[51] Holger Bech Nielsen and M. Ninomiya. No Go Theorem for Regularizing Chiral Fermions. *Phys. Lett. B*, 105:219–223, 1981.

[52] Kenneth G. Wilson. Quarks and Strings on a Lattice. In *13th International School of Subnuclear Physics: New Phenomena in Subnuclear Physics*, 11 1975.

[53] John B. Kogut and Leonard Susskind. Hamiltonian Formulation of Wilson's Lattice Gauge Theories. *Phys. Rev. D*, 11:395–408, 1975.

[54] Leonard Susskind. Lattice Fermions. *Phys. Rev. D*, 16:3031–3039, 1977.

[55] Tom Banks, S. Raby, Leonard Susskind, John B. Kogut, D. R. T. Jones, P. N. Scharbach, and D. K. Sinclair. Strong Coupling Calculations of the Hadron Spectrum of Quantum Chromodynamics. *Phys. Rev. D*, 15:1111, 1977.

[56] B. Sheikholeslami and R. Wohlert. Improved Continuum Limit Lattice Action for QCD with Wilson Fermions. *Nucl. Phys. B*, 259:572, 1985.

[57] R. Sommer. A New way to set the energy scale in lattice gauge theories and its applications to the static force and alpha-s in SU(2) Yang-Mills theory. *Nucl. Phys. B*, 411:839–854, 1994.

[58] R. Narayanan and H. Neuberger. Infinite N phase transitions in continuum Wilson loop operators. *JHEP*, 03:064, 2006.

[59] Martin Luscher. Trivializing maps, the Wilson flow and the HMC algorithm. *Commun. Math. Phys.*, 293:899–919, 2010.

[60] Szabolcs Borsanyi et al. High-precision scale setting in lattice QCD. *JHEP*, 09:010, 2012.

[61] Pierre van Baal. Gribov ambiguities and the fundamental domain. In *NATO Advanced Study Institute on Confinement, Duality and Nonperturbative Aspects of QCD*, pages 161–178, 6 1997.

[62] F E Close. Introduction to quarks and partons, Jan 1979.

[63] W. Bietenholz et al. Flavour blindness and patterns of flavour symmetry breaking in lattice simulations of up, down and strange quarks. *Phys. Rev.*, D84:054509, 2011.

[64] W. Bietenholz et al. Tuning the strange quark mass in lattice simulations. *Phys. Lett. B*, 690:436–441, 2010.

[65] R. Horsley et al. QED effects in the pseudoscalar meson sector. *JHEP*, 04:093, 2016.

[66] J. J. de Swart. The Octet model and its Clebsch-Gordan coefficients. *Rev. Mod. Phys.*, 35:916–939, 1963. [Erratum: Rev. Mod. Phys.37,326(1965)].

[67] Sidney R. Coleman and Sheldon Lee Glashow. Electrodynamic properties of baryons in the unitary symmetry scheme. *Phys. Rev. Lett.*, 6:423, 1961.

[68] J. Franklin, D. B. Lichtenberg, W. Namgung, and D. Carydas. Wave Function Mixing of Flavor Degenerate Baryons. *Phys. Rev. D*, 24:2910, 1981.

[69] Nathan Isgur. Isospin violating mass differences and mixing angles: the role of quark masses. *Phys. Rev.*, D21:779, 1980. [Erratum: Phys. Rev.D23,817(1981)].

[70] Avraham Gal. Comment on "Lattice determination of Σ–Λ mixing". *Phys. Rev.*, D92(1):018501, 2015.

[71] R. Horsley, J. Najjar, Y. Nakamura, H. Perlt, D. Pleiter, P. E. L. Rakow, G. Schierholz, A. Schiller, H. Stüben, and J. M. Zanotti. Reply to Comment on 'Lattice determination of Σ-Λ mixing'. *Phys. Rev.*, D92:018502, 2015.

[72] Z.R. Kordov, R. Horsley, Y. Nakamura, H. Perlt, P.E.L. Rakow, G. Schierholz, H. Stben, R.D. Young, and J.M. Zanotti. Electromagnetic contribution to Σ-Λ mixing using lattice QCD+QED. *Phys. Rev. D*, 101(3):034517, 2020.

[73] H. Georgi. LIE ALGEBRAS IN PARTICLE PHYSICS. FROM ISOSPIN TO UNIFIED THEORIES. *Front. Phys.*, 54:1–255, 1982.

[74] S. Meshkov, C. A. Levinson, and H. J. Lipkin. Verification of the Tenfold Assignment of the Baryon Resonances. *Phys. Rev. Lett.*, 10:361–364, 1963.

[75] Benoit Blossier, Michele Della Morte, Georg von Hippel, Tereza Mendes, and Rainer Sommer. On the generalized eigenvalue method for energies and matrix elements in lattice field theory. *JHEP*, 04:094, 2009.

[76] Martin Luscher and Ulli Wolff. How to Calculate the Elastic Scattering Matrix in Two-dimensional Quantum Field Theories by Numerical Simulation. *Nucl. Phys.*, B339:222–252, 1990.

[77] S. Aoki et al. FLAG Review 2019. 2019.

[78] Michael Peardon, John Bulava, Justin Foley, Colin Morningstar, Jozef Dudek, Robert G. Edwards, Balint Joo, Huey-Wen Lin, David G. Richards, and Keisuke Jimmy Juge. A Novel quark-field creation operator construction for hadronic physics in lattice QCD. *Phys. Rev. D*, 80:054506, 2009.

[79] J. J. Wu, W. Kamleh, D. B. Leinweber, R. D. Young, and J. M. Zanotti. Accessing high-momentum nucleons with dilute stochastic sources. *J. Phys. G*, 45(12):125102, 2018.

[80] Constantia Alexandrou, Simon Dinter, Vincent Drach, Karl Jansen, Kyriakos Hadjiyiannakou, and Dru B. Renner. A Stochastic Method for Computing Hadronic Matrix Elements. *Eur. Phys. J. C*, 74(1):2692, 2014.

[81] N. Eicker et al. Evaluating sea quark contributions to flavor singlet operators in lattice QCD. *Phys. Lett. B*, 389:720–726, 1996.

[82] Justin Foley, K. Jimmy Juge, Alan O'Cais, Mike Peardon, Sinead M. Ryan, and Jon-Ivar Skullerud. Practical all-to-all propagators for lattice QCD. *Comput. Phys. Commun.*, 172:145–162, 2005.

[83] P. A. Boyle, A. Juttner, C. Kelly, and R. D. Kenway. Use of stochastic sources for the lattice determination of light quark physics. *JHEP*, 08:086, 2008.

[84] C. Alexandrou, M. Constantinou, V. Drach, K. Hadjiyiannakou, K. Jansen, G. Koutsou, A. Strelchenko, and A. Vaquero. Evaluation of disconnected quark loops for hadron structure using GPUs. *Comput. Phys. Commun.*, 185:1370–1382, 2014.

[85] Gunnar S. Bali, Sara Collins, and Andreas Schafer. Effective noise reduction techniques for disconnected loops in Lattice QCD. *Comput. Phys. Commun.*, 181:1570–1583, 2010.

[86] Andreas Stathopoulos, Jesse Laeuchli, and Kostas Orginos. Hierarchical probing for estimating the trace of the matrix inverse on toroidal lattices. 2 2013.

[87] Jeremy Green, Stefan Meinel, Michael Engelhardt, Stefan Krieg, Jesse Laeuchli, John Negele, Kostas Orginos, Andrew Pochinsky, and Sergey Syritsyn. High-precision calculation of the strange nucleon electromagnetic form factors. *Phys. Rev. D*, 92(3):031501, 2015.

[88] Gunnar S. Bali, Vladimir Braun, Sara Collins, Andreas Schäfer, and Jakob Simeth. Masses and decay constants of the η and η' mesons from lattice QCD. 6 2021.

[89] C. McNeile and Christopher Michael. Decay width of light quark hybrid meson from the lattice. *Phys. Rev. D*, 73:074506, 2006.

[90] Constantia Alexandrou and Giannis Koutsou. A Study of Hadron Deformation in Lattice QCD. *Phys. Rev. D*, 78:094506, 2008.

[91] Eric Endress, Carlos Pena, and Karthee Sivalingam. Variance reduction with practical all-to-all lattice propagators. *Comput. Phys. Commun.*, 195:35–48, 2015.

[92] Yi-Bo Yang, Andrei Alexandru, Terrence Draper, Ming Gong, and Keh-Fei Liu. Stochastic method with low mode substitution for nucleon isovector matrix elements. *Phys. Rev. D*, 93(3):034503, 2016.

[93] Yutaro Akahoshi, Sinya Aoki, Tatsumi Aoyama, Takumi Doi, Takaya Miyamoto, and Kenji Sasaki. $\mathbf{I = 2}$ $\boldsymbol{\pi\pi}$ potential in the HAL QCD method with all-to-all propagators. *PTEP*, 2019(8):083B02, 2019.

[94] H. Neff, N. Eicker, T. Lippert, John W. Negele, and K. Schilling. On the low fermionic eigenmode dominance in QCD on the lattice. *Phys. Rev. D*, 64:114509, 2001.

[95] Rafel Escribano and Emilio Royo. π^0-η-η' mixing from $V \to P\gamma$ and $P \to V\gamma$ decays. *Phys. Lett. B*, 807:135534, 2020.

[96] P. Kroll. Isospin symmetry breaking through pi0 - eta - eta-prime mixing. *Mod. Phys. Lett. A*, 20:2667–2684, 2005.

[97] Maurice Benayoun, Luigi DelBuono, and Friedrich Jegerlehner. BHLS$_2$ Upgrade : τ spectra, muon HVP and the $[\pi^0,\ \eta,\ \eta']$ System. 5 2021.

[98] Zhen-Hua Zhang. The pollution to the $K\pi$-puzzle from the isospin-breaking $\pi^0 - \eta - \eta'$ mixing effect. 12 2021.

[99] Eric B. Gregory, Alan C. Irving, Christopher M. Richards, and Craig McNeile. A study of the eta and eta' mesons with improved staggered fermions. *Phys. Rev. D*, 86:014504, 2012.

[100] Konstantin Ottnad and Carsten Urbach. Flavor-singlet meson decay constants from $N_f = 2 + 1 + 1$ twisted mass lattice QCD. *Phys. Rev. D*, 97(5):054508, 2018.

[101] Edward Witten. Instantons, the Quark Model, and the 1/n Expansion. *Nucl. Phys. B*, 149:285–320, 1979.

[102] T. Feldmann, P. Kroll, and B. Stech. Mixing and decay constants of pseudoscalar mesons: The Sequel. *Phys. Lett. B*, 449:339–346, 1999.

[103] Z. R. Kordov et al. State mixing and masses of the $\pi 0$, η and η' mesons from nf=1+1+1 lattice QCD+QED. *Phys. Rev. D*, 104(11):114514, 2021.

[104] Konstantin Ottnad, C. Michael, S. Reker, C. Urbach, Chris Michael, Siebren Reker, and Carsten Urbach. \eta and \eta' mesons from Nf=2+1+1 twisted mass lattice QCD. *JHEP*, 11:048, 2012.

[105] M. S. Mahbub, Alan O. Cais, Waseem Kamleh, B. G. Lasscock, Derek B. Leinweber, and Anthony G. Williams. Isolating Excited States of the Nucleon in Lattice QCD. *Phys. Rev. D*, 80:054507, 2009.

[106] Benjamin J. Menadue, Waseem Kamleh, Derek B. Leinweber, and M. Selim Mahbub. Isolating the $\Lambda(1405)$ in Lattice QCD. *Phys. Rev. Lett.*, 108:112001, 2012.

[107] Benjamin J. Owen, Jack Dragos, Waseem Kamleh, Derek B. Leinweber, M. Selim Mahbub, Benjamin J. Menadue, and James M. Zanotti. Variational Approach to the Calculation of gA. *Phys. Lett. B*, 723:217–223, 2013.

[108] Boram Yoon et al. Controlling Excited-State Contamination in Nucleon Matrix Elements. *Phys. Rev. D*, 93(11):114506, 2016.

[109] R. Horsley et al. Isospin splittings in the decuplet baryon spectrum from dynamical QCD+QED. 2019.

[110] R. Horsley et al. Isospin splittings of meson and baryon masses from three-flavor lattice QCD + QED. *J. Phys.*, G43(10):10LT02, 2016.

[111] A. Bramon, R. Escribano, and M. D. Scadron. The eta - eta-prime mixing angle revisited. *Eur. Phys. J. C*, 7:271–278, 1999.

[112] T. Feldmann, P. Kroll, and B. Stech. Mixing and decay constants of pseudoscalar mesons. *Phys. Rev. D*, 58:114006, 1998.

[113] J. S. Bell and R. Jackiw. A PCAC puzzle: $\pi^0 \to \gamma\gamma$ in the σ model. *Nuovo Cim. A*, 60:47–61, 1969.

[114] Stephen L. Adler. Axial vector vertex in spinor electrodynamics. *Phys. Rev.*, 177:2426–2438, 1969.

[115] Stephen L. Adler and William A. Bardeen. Absence of higher order corrections in the anomalous axial vector divergence equation. *Phys. Rev.*, 182:1517–1536, 1969.

[116] G. 't Hooft. Symmetry breaking through bell-jackiw anomalies. *Phys. Rev. Lett.*, 37:8–11, Jul 1976.

[117] G. Veneziano. U(1) Without Instantons. *Nucl. Phys. B*, 159:213–224, 1979.

[118] J. Elam et al. The REDTOP experiment: Rare η/η' Decays To Probe New Physics. In *2022 Snowmass Summer Study*, 3 2022.

[119] Thorsten Feldmann. Quark structure of pseudoscalar mesons. *Int. J. Mod. Phys. A*, 15:159–207, 2000.

[120] Rafel Escribano and Jean-Marie Frere. Study of the eta - eta-prime system in the two mixing angle scheme. *JHEP*, 06:029, 2005.

[121] G. Martinelli, C. Pittori, Christopher T. Sachrajda, M. Testa, and A. Vladikas. A General method for nonperturbative renormalization of lattice operators. *Nucl. Phys. B*, 445:81–108, 1995.

[122] M. Gockeler, R. Horsley, H. Oelrich, H. Perlt, D. Petters, Paul E. L. Rakow, A. Schafer, G. Schierholz, and A. Schiller. Nonperturbative renormalization of composite operators in lattice QCD. *Nucl. Phys. B*, 544:699–733, 1999.

[123] A. J. Chambers, R. Horsley, Y. Nakamura, H. Perlt, P. E. L. Rakow, G. Schierholz, A. Schiller, and J. M. Zanotti. A novel approach to nonperturbative renormalization of singlet and nonsinglet lattice operators. *Phys. Lett. B*, 740:30–35, 2015.

[124] M. Constantinou, M. Hadjiantonis, H. Panagopoulos, and G. Spanoudes. Singlet versus nonsinglet perturbative renormalization of fermion bilinears. *Phys. Rev. D*, 94(11):114513, 2016.

[125] A. Skouroupathis and H. Panagopoulos. Two-loop renormalization of vector, axial-vector and tensor fermion bilinears on the lattice. *Phys. Rev. D*, 79:094508, 2009.

[126] V. G. Bornyakov, R. Horsley, Y. Nakamura, H. Perlt, D. Pleiter, P. E. L. Rakow, G. Schierholz, A. Schiller, H. Stüben, and J. M. Zanotti. Flavour breaking effects in the pseudoscalar meson decay constants. *Phys. Lett. B*, 767:366–373, 2017.